



TECHNISCHE
UNIVERSITÄT
WIEN
Vienna University of Technology

INSTITUT FÜR
MECHANIK UND
MECHATRONIK
Mechanics & Mechatronics



DIPLOMARBEIT

Design and Implementation of a Model Predictive Controller for a Small-Scale Biomass Combustion Furnace

ausgeführt zum Zwecke der Erlangung des akademischen Grades eines Diplom-Ingenieurs
unter der Betreuung von

Dipl.-Ing. Lukas Böhler

und unter der Leitung von

Ao.Univ.Prof. Dipl.-Ing. Dr.techn. Martin Kozek

Institut für Mechanik und Mechatronik

Abteilung für Regelungstechnik und Prozessautomatisierung

eingereicht an der Technischen Universität Wien

Fakultät für Maschinenwesen und Betriebswissenschaften

von

Markus Fallmann

Matr.Nr.: 01425369

Neubruckweg 1

3494 Theiß

Eidesstattliche Erklärung

Ich erkläre an Eides statt, dass ich die vorliegende Arbeit selbständig angefertigt, keine anderen als die angegebenen Hilfsmittel benutzt und alle aus ungedruckten Quellen, gedruckter Literatur oder aus dem Internet im Wortlaut oder im wesentlichen Inhalt übernommenen Formulierungen und Konzepte gemäß den Richtlinien wissenschaftlicher Arbeiten zitiert, durch Fußnoten gekennzeichnet bzw. mit genauer Quellenangabe kenntlich gemacht habe.

Wien, am 17. Juni 2020

Markus Fallmann

Danksagung

Leider lässt sich eine wahrhafte Dankbarkeit mit Worten nicht ausdrücken.

— Johann Wolfgang von Goethe

Kurzfassung

Obwohl Kleinfeuerungsanlagen stärkeren Schwankungen des Wärmebedarfs unterliegen als dies für Großanlagen der Fall ist, liegt das Hauptaugenmerk klassischer Ansätze der Verbrennungsregelung auf der Handhabung stationärer Zustände. Wirtschaftliche Aspekte sowie gesetzliche Emissionsbeschränkungen und die Anforderung nach immer höheren Wirkungsgraden verlangen nach einem fortschrittlichen Regelalgorithmus, der neben der Berücksichtigung transienter Vorgänge gleichzeitig kostengünstig in Implementierung und Wartung ist. Die vorliegende Arbeit beschäftigt sich mit der Regelung einer Kleinfeuerungsanlage zur Verbrennung von Biomasse. Dabei kommt eine Reglerstruktur bestehend aus einem linearen, modellprädiktiven Regelalgorithmus und einem Zustandsschätzer zum Einsatz. Die Aufgabe liegt darin, den gesamten Leistungsbereich des zu untersuchenden Ofens lediglich mit einem solch simplen Ansatz zufriedenstellend abzudecken. Eine Grey-Box-Modellierung des nichtlinearen Ofens bildet die Basis für die Reglerauslegung und die Bestimmung eines optimalen Linearisierungspunktes, wobei zur Bewertung der Optimalität eine passende Abstands-Metrik verwendet wird. Da Kohlenstoffmonoxid einen wichtigen Indikator zur Beschreibung der Verbrennungsgüte darstellt, ist eine Minimierung dieses Schadstoffes von großem Interesse. Aufgrund des hochgradig nichtlinearen Oxidationsprozesses ist die direkte Regelung dieser Größe mit einem linearen Ansatz nur beschränkt realisierbar. Zur Regelung der Verbrennungsgüte wird die Sauerstoffkonzentration als Regelgröße herangezogen. Dabei wird zusätzlich ein unteres Limit dieser Größe in der Formulierung des Regelalgorithmus implementiert, um hohe Schadstoffbildung infolge ausgeprägten Sauerstoffmangels zu verhindern. Die Performance des geschlossenen Regelkreises wird anhand experimenteller Untersuchungen für die Verbrennung verschiedener biogener Brennstoffe gezeigt, wobei sowohl im Stationärbetrieb als auch in den Übergangsphasen ein zufriedenstellendes Ergebnis erreicht wird. Da Brennstoffparameter explizit in der Formulierung des Ofen-Modells berücksichtigt werden, eröffnet sich eine einfache und zugleich kostengünstige Möglichkeit, Brennstoffwechsel durch simple Umparametrierung des Modells zu realisieren. Experimentelle Versuchsergebnisse verdeutlichen die Wichtigkeit der gewählten Sauerstoffreferenz im Hinblick auf die Qualität der Verbrennung. Aus der Literatur wird ein einfaches Modell der Kohlenstoffdioxid-Entstehung herangezogen, an den zu untersuchenden Ofen angepasst und schließlich zur Vorgabe passender Referenzwerte der Sauerstoffkonzentration verwendet. Der optimale Charakter dieser systematischen Festlegung wird mittels Simulation bestätigt.

Abstract

Although small-scale furnaces are subject to stronger fluctuations in heat demand compared to larger facilities, widely used control strategies most often only consider steady state operation. Economic aspects, emission regulations, and the steadily increasing need for higher efficiency call for a versatile control algorithm taking transient operation into account while being cost-efficient in implementation and maintenance. This work introduces an optimized control architecture, comprising a simple linear model predictive controller and a state estimation, in order to cover the whole operating range of an investigated small-scale biomass furnace. A grey-box model of the plant provides a basis for controller design as well as for determination of an appropriate linearization point by utilizing a gap metric. Among all pollutants, resulting from (incomplete) combustion, carbon monoxide is of particular importance, as its occurrence strongly indicates sub-par efficiency. However, the highly non-linear oxidation process impedes direct controlling of carbon monoxide by means of a simple linear approach. Therefore, the oxygen concentration in the flue gas is used as the emission-related control variable. Additionally, input and oxygen constraints are implemented to account for saturation of control variables and to prevent incomplete combustion, respectively. Experimental closed-loop results are presented for the combustion of different solid biofuels and indicate satisfying control performance not only in steady state but also in transient operation. Based on the introduced furnace model, which incorporates fuel-related parameters in an explicit manner, a simple and cost-efficient procedure for fuel switches is outlined. Since the highly influential role of the applied oxygen reference on carbon monoxide formation is significant in experimental results, a formation model from literature is used in an adapted formulation to provide emission-optimized reference values. Closed-loop simulation results confirm an overall improvement based on systematically picked oxygen references. The introduced overall control structure keeps complexity low and simultaneously offers a wide variety of possibilities yielding increased control performance along with minimized emission formation.

Contents

1	Introduction	1
1.1	Today's significance of biomass combustion	1
1.2	Combustion control of small-scale furnaces	3
1.2.1	Classical approach	4
1.2.2	Advanced strategies	4
2	Modeling	6
2.1	Chemistry of biomass combustion in a nutshell	6
2.1.1	Fuel properties	6
2.1.2	Thermochemical conversion and emission formation	8
2.2	Process description	10
2.3	Modeling approaches from literature	11
2.4	Furnace model	13
2.4.1	Model equations	13
2.4.2	Model identification and validation	16
2.4.3	Applicability	19
2.5	Emission models	21
3	Controller design	22
3.1	Extended furnace	22
3.1.1	Input interface	22
3.1.2	Feedforward controller	24
3.2	Extended controller	26
3.2.1	MPC	26
3.2.2	Observer	32
3.2.3	Reference interface	32
4	Results and discussion	34
4.1	Closed-loop results for wooden pellets	34
4.2	Fuel flexibility	37
4.3	Emission reduced control	37
5	Conclusion	40

A	Fundamentals of discrete-time linear MPC	42
A.1	Basic concept of model predictive control	42
A.2	Linear discrete-time formulation	43
A.3	Consideration of constraints	46
A.3.1	Rate constraints on input	46
A.3.2	Amplitude constraints on input	46
A.3.3	Output constraints	47
A.3.4	Conclusive optimization problem	48
A.4	Receding horizon principle	49
A.5	Stability	49
A.5.1	Terminal equality constraints	50
A.5.2	Terminal costs	51
A.5.3	Terminal set constraints	52
B	Fundamentals of Kalman-filtering	53
B.1	Process description	53
B.2	Filter formulation	54
B.3	Derivation	55
B.4	One-step Kalman filter equations	57
B.5	Existence and stability	58
B.6	Extended Kalman filter	60
C	Fundamentals of gap metric	61
	Bibliography	63

Chapter 1

Introduction

Utilizing fire in a controlled way has played a major role in human evolution, not only to provide warmth but also to repeal wild animals, cook food, and extend shelf-life of perishable goods [1]. Combustion of biomass enhanced primeval life significantly, and despite today's wide range of energy sources it is still of vital importance. As it is indirectly formed by solar irradiation from the sun, biomass is considered as a renewable energy source (see definition in the box given below). Due to global climate change and limited fossil fuels, this kind of energy source gained increased interest in recent years.

renewable energy sources [2]

Energy is considered renewable, if its source constantly regenerates itself. Consequently, renewable energy sources are assumed to be inexhaustible in human dimensions.

Out of numerous and partly inconsistent definitions of biomass, the ones presented in the box below are reasonable in the given context of this work.

biomass

While IUPAC [3] defines biomass as

*a material produced by the growth of microorganisms, plants,
or animals,*

the definition according to Kaltschmitt et al. [2] explicitly excludes already fossilized phytomass and zoomass to facilitate differentiation from fossil fuels.

1.1 Today's significance of biomass combustion

Increasing shares of energy, especially for heating, rely on renewable energy sources, whereby Sweden has taken a pioneering role in the EU, see Fig. 1.1a. A breakdown of

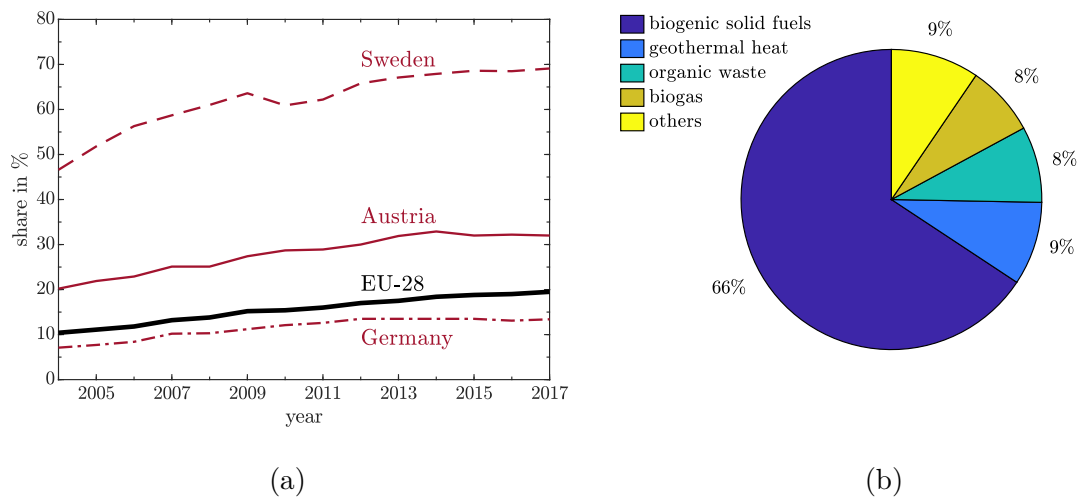


Figure 1.1: (a) Share of energy from renewable sources for heating and cooling, depicted for the EU-28 and selected European countries [4]. Annual averages are connected to guide the eye. (b) Breakdown of heat energy from renewable sources according to its particular source of energy in 2019 in Germany [5].

heat energy generated in 2019 in Germany by utilizing renewable sources (Fig. 1.1b) illustrates the important role of solid biofuels.

In urban areas large furnaces supply heat for many facilities, which exhibit a strongly changing individual heat demand throughout the day. But, aggregation of these single contributions comes along with a smooth and well-predictable total demand. Therefore, such furnaces operate in steady state for most of the time, which facilitates highly efficient and emission-optimized combustion. Additionally, high output power and long operating life, accompanied by immense acquisition costs, justify sophisticated control strategies improving the overall performance even further.

Conversely, in rural regions heat supply is more likely to be organized in a decentralized manner, carried out by small-scale furnaces with a nominal heat capacity of less than 500 kW. Economic aspects of this market segment call for a simple and cost-effective controller design, which is partially in contradiction to emission-related objectives. Based on larger variations in the heat demand, related to this kind of application, the need rises to account not only for steady-state but also for transient behavior in an appropriate manner.

Furthermore, furnace manufacturers face challenges by introduced legal emission regulations. Fig. 1.2 compares legal restrictions for small-scale furnaces that are effective in Austria and Germany, respectively (presented data are valid for furnaces with a nominal heat capacity between 50 kW and 500 kW and utilized for heating rooms or for warm water treatment). While the Austrian government limits emission of carbon monoxide (CO), particulate matter (PM), and nitrogen oxides (NO_x), it also states a minimum required efficiency η_{\min} . Although, Germany's actual law only acts on CO

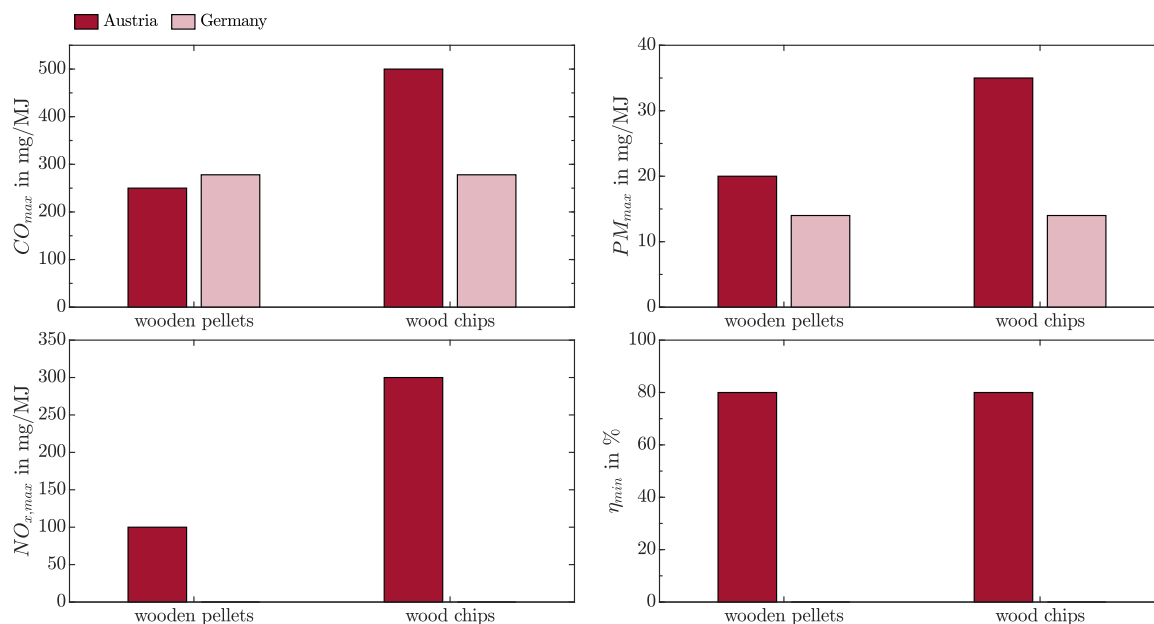


Figure 1.2: Comparison of current legal emission regulations for small-scale furnaces in Austria [6] and Germany [7]. Missing bars indicate no current limitations.

and PM emissions, its limits are more restrictive in most cases. Among all these emissions, CO is of vital importance, since it is well correlated with combustion quality - see section 2.1.2 for detailed information.

1.2 Combustion control of small-scale furnaces

As mentioned above, combustion control comprises two main tasks: keeping track of a required heat output and maintaining a high combustion quality. Usually, the released heat energy is transferred from the flue gas to a heat medium, e.g. water, by using a heat exchanger. Assuming a constant heat medium mass flow and a constant return temperature, the heat output relates to the supply temperature T_{sup} , which is therefore considered as a control variable from now on.

From a technical point of view, it would be favored to control CO emissions directly in order to ensure a high combustion quality. Unfortunately, its highly non-linear formation process complicates application of linear control approaches. Furthermore, lack of an appropriate emission model as well as the availability of cost-efficient oxygen (O_2) sensors suggest the use of O_2 concentration as the control variable related to combustion efficiency. Additionally, its dynamic is by far less non-linear than the one of CO, which enables an appropriate control performance for most industrial applications by employing simple linear algorithms.

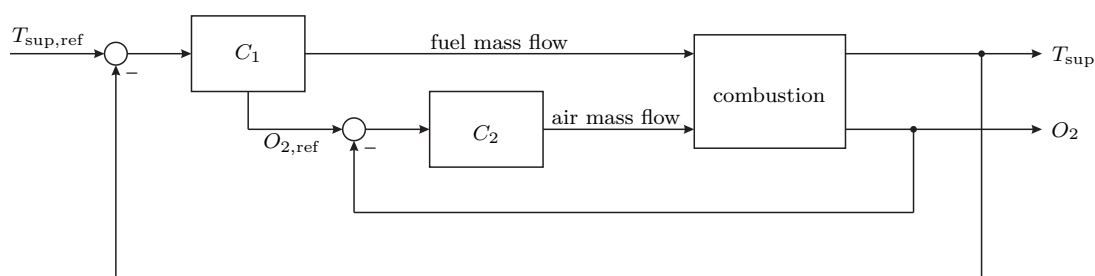


Figure 1.3: Classical concept of combined power and combustion control based on cascading loops with controllers C_1 and C_2 .

Simple and cost-efficient design characterize classical approaches, while advanced control strategies come along with a higher design effort justified by an usually better fulfillment of control objectives.

1.2.1 Classical approach

Classical industrial control strategies mostly rely on the simple proportional-integral-derivative (PID) control algorithm and so they do for furnaces as well. Fig. 1.3 depicts the widely used control concept for biomass furnaces, based on cascading loops with two PID controllers C_1 and C_2 in total [2]. In this setup the outer loop controls T_{sup} by adapting the fuel mass flow, and the inner loop keeps track of a desired oxygen concentration $O_{2,\text{ref}}$, which is defined according to the actual fuel mass flow. Note that in real implementations C_1 may also determine a part of the air mass flow based on a fixed ratio to the fuel mass flow.

Since many furnaces operate in power ranges close to the nominal heat output for most of the time, utilization of linear controllers is reasonable. But, as the independently designed control loops inherently neglect obvious couplings, control performance further decreases. To overcome this lack, at least in steady-state conditions, manufactures often implement a feedforward controller and therefore force C_1 and C_2 to act deviation-related.

Nonetheless, due to high furnace complexity all mentioned strategies are rarely model-based but rather designed empirically in real applications. While extensive effort is put into hardware optimization, an insufficient basis for the controller design yields a performance undoubtedly worthy of improvement.

1.2.2 Advanced strategies

More advanced control strategies are capable of handling state transitions and not only steady state operation according to efficiency perspectives. While model predictive approaches were already investigated in furnaces with high nominal heat output [8–11], little was done for small-scale furnaces. Besides the design of dynamic feedforward controllers reported in [12, 13], only Böhler et. al [14] dealt with model-based approaches

for small furnaces. The latter presented simulation results obtained by using a fuzzy model predictive controller for the very same furnace investigated within this work. But, to combine the massive advantages, coming along with a model predictive strategy, with the need of an economically justifiable solution, the implementation must be as simple as anyway possible.

For this purpose, a simple linear model predictive controller (MPC) for a small-scale biomass furnace is introduced in this work. The presented grey-box model of the furnace is of low-order to facilitate fast computation, is combined with adaptations to serve furnace characteristics, and enables helpful process insight due to the physical nature of model parameters, see section 2.4. The implemented MPC (section 3) explicitly accounts for the given overall furnace setup, covering an additional feedforward controller, to maintain manufacturers' empirical knowledge. Experimental closed-loop results obtained for the combustion of different solid biofuels not only confirm applicability of the chosen approach but also highlight the possibility of simple fuel switches by just adapting fuel-related model parameters (section 4). Based on experimental results, comprehensive simulations together with a model of the CO formation process, see section 2.5 or [15], yield recommendations on how to choose O_2 references and MPC configuration appropriately to achieve a minimum of emissions.

Chapter 2

Modeling

Besides high model accuracy, the model structure itself is equally important. Due to limited computational power of the furnace hardware, a lumped model is preferred. At the beginning of this chapter, the chemical process is outlined briefly to provide a basic understanding of biomass combustion. After reviewing model approaches from literature, the chosen process model together with its identification and validation is presented.

2.1 Chemistry of biomass combustion in a nutshell

Only a small insight into the extensive field of combustion chemistry is given, whereby it is appropriately selected to meet the necessary needs for the intended modeling and control purpose. Hereinafter, chemical aspects related to the combustion of solid biofuels, in particular wooden pellets and wood chips, are considered. If not otherwise stated, following remarks are based on [2].

2.1.1 Fuel properties

More than 95 % of the dry matter of solid biofuels consist of only three biopolymers: cellulose, hemicellulose, and lignin. The latter is a cross-linked polymer stiffening the mixture of cellulose (unbranched polysaccharide) and hemicellulose (branched polysaccharide). A simple approach neglects the exact chemical structure and only considers the fuel as a mixture of its main elements, yielding an average elemental composition of $\text{CH}_{1.44}\text{O}_{0.66}$ for wood. But, since fuels also contain water (H_2O), incombustible compounds (ash), and traces of other chemical elements, such a simple analytic study is insufficient to determine heat-related fuel parameters. However, the net calorific value q_{net} and gross calorific value q_{gr} of the actual fuel can be identified by experimental methods [16]. These parameters are of vital importance, as they are directly related to the heat quantity accessible by combustion - definitions are given in the boxes below.

net calorific value q_{net}

The net calorific value is the heat produced by complete oxidation of one unit of a fuel, combusted under isobaric conditions such that all the water is vaporized.

gross calorific value q_{gr}

In addition to the net calorific value, the gross calorific value assumes that all the water is condensed. Therefore, the relation $q_{\text{gr}} \geq q_{\text{net}}$ holds.

As no significant condensation takes place in the investigated furnace, the water content $w_{\text{H}_2\text{O}}$ plays a crucial role. Additionally, this parameter as well as the ash content a_{ash} are subject to at least slight changes over different fuel batches. For the sake of clarity, definitions are given below.

water content $w_{\text{H}_2\text{O}}$

The water content is defined as

$$w_{\text{H}_2\text{O}} = \frac{m_{\text{H}_2\text{O}}}{m_{\text{fuel}}}, \quad (2.1)$$

where $m_{\text{H}_2\text{O}}$ is the mass of water bonded in the total fuel mass m_{fuel} .

ash content a_{ash}

Similar to the water content, the ash content is defined as a mass ratio according to

$$a_{\text{ash}} = \frac{m_{\text{ash}}}{m_{\text{fuel}}} \quad (2.2)$$

with m_{ash} as the ash mass.

Therefore, a comprehensive model has to account for changes in $w_{\text{H}_2\text{O}}$ and a_{ash} . For this purpose, the gross calorific value is adapted in such a sense that it is no longer related to the total fuel mass m_{fuel} but to the dry and ash-free mass, yielding the calorific value

$$q_{\text{gr-ah,af}} = \frac{q_{\text{gr}|s}}{(1 - w_{\text{H}_2\text{O}|s})(1 - a_{\text{ash}|s})}, \quad (2.3)$$

where the suffix ($|s$) denotes values gained by analyzing a fuel sample. Using the dry and ash-free fuel mass as the actual heat source allows to conveniently incorporate varying water and ash contents into the model description, see section 2.4.

2.1.2 Thermochemical conversion and emission formation

Since oxygen, as an oxidizer, strongly influences biomass combustion, the available amount must be sufficiently high to enable complete combustion. In general, not pure oxygen but ambient air with an average oxygen concentration of 21 Vol.-% is supplied to the furnace. Therefore, the excess air ratio λ (see the box below) is introduced to characterize the overall combustion but also to distinguish between different combustion stages.

excess air ratio λ

This is the ratio of the actual available air mass m_a to the air mass $m_{a,\min}$ that is stoichiometrically required for complete combustion, mathematically described by

$$\lambda = \frac{m_a}{m_{a,\min}}. \quad (2.4)$$

Figure 2.1 depicts the evolution of thermochemical biomass combustion in a schematic manner. In the first stage, dehydration, the considered fuel mass is heated up to a temperature of approximately 200°C, which is accompanied by evaporation of all the water bonded in the organic matter. Besides this phase, also the next one, the pyrolytic decomposition, takes place under exclusion of air ($\lambda = 0$). At temperatures between 150°C and 220°C macromolecules start to break down, forming gaseous decomposition products. Up to 85% of the organic matter are converted in this stage, which is largely completed by reaching 500°C. Subsequently, air (primary air) is used as gasification medium to convert residual carbon into combustible gases. While the first two stages comprise endothermic reactions only, gasification is mainly accompanied by thermal release and therefore an increase in temperature. In the last stage, all products, resulting from pyrolytic decomposition and gasification, undergo a homogeneous gasphase oxidation in the presence of excess air ($\lambda > 1$). This is obtained by supplying an additional air mass flow (secondary air). Highly exothermic oxidation results in products related to a complete combustion (carbon dioxide CO₂, H₂O) as well as unwanted side products (CO, unburnt hydrocarbons C_nH_m, nitrogen oxides NO_x, PM), which are often referred to as emissions. Since atmospheric molecular nitrogen (N₂) is only partially involved in the reaction, it is not explicitly stated as an output in Fig. 2.1. In addition to the above mentioned combustion products, also the incombustible fuel components (ash) remain as part of the overall residues.

Among all outputs, occurring CO emissions are most directly related to combustion quality and are therefore ideally qualified to assess the completeness of combustion. Furthermore, a characteristic relation between CO and λ holds, indicating the possibility to influence efficiency by adapting the air mass flow, see Fig. 2.2. While low values of λ come along with at least local oxygen deficiency, high air mass flows decrease combustion temperature. While both effects inhibit oxidation, values of λ between 1.5

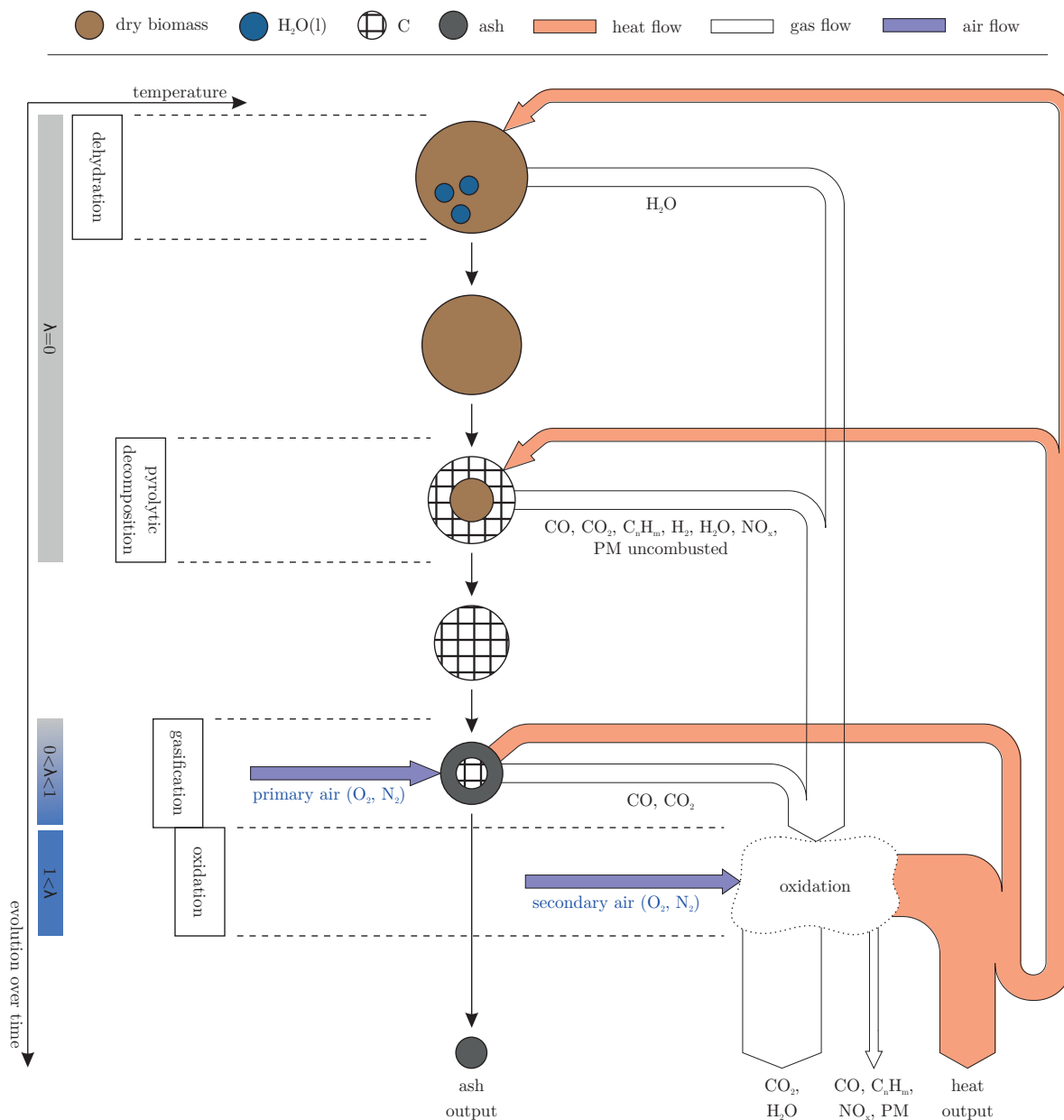


Figure 2.1: Evolution of thermochemical biomass conversion and emission formation over time, depicted in a schematic fashion adapted from [2].

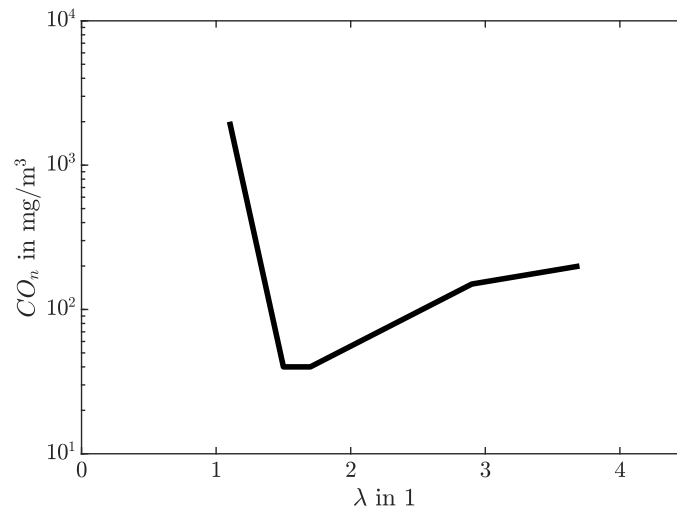


Figure 2.2: Dependency of CO emissions on excess air ratio λ . Index n denotes reference to standard cubic meters. Diagram shows qualitative data [2] for automatically fed wood combustion.

and 2.5 provide promising results. Since λ is basically a convenient formulation of the available amount of oxygen, the presented relation justifies the common practice of controlling the oxygen concentration in order to ensure high combustion quality. However, appropriate oxygen references must be defined to meet emission-related objectives, see section 4.3 for a detailed discussion.

2.2 Process description

The investigated plant is a small-scale biomass grate furnace with a nominal heat output of 100 kW, primarily designed for the combustion of wooden pellets. A schematic drawing is depicted in Fig. 2.3. While the fuel mass flow \dot{m}_{fuel} is fed onto the grate, the primary air mass flow \dot{m}_{pa} passes through the fuel bed to enable gasification (compare air flows in Fig. 2.1). To account for local differences in the composition of the combustion gas, secondary air can be supplied through two different inlets, providing mass flows \dot{m}_{sa_1} and \dot{m}_{sa_2} . After oxidation, the flue gas mass flow \dot{m}_{fg} leaves the chamber with the freeboard temperature T_{fb} and enters the heat exchanger, in which most of the heat is transferred to the water mass flow \dot{m}_{w} . Since the return temperature T_{ret} and \dot{m}_{w} are kept constant in the investigated experimental setup, the supply temperature T_{sup} is directly proportional to the heat output. In addition to \dot{m}_{fg} with the flue gas temperature T_{fg} , ash residues (mass flow \dot{m}_{ash}) also leave the furnace.

A model of this furnace has to be detailed enough to serve the intended control purpose but simple enough to allow fast computations even by utilizing low-cost hardware. To serve this demand, a lumped model is preferred. Various modeling approaches

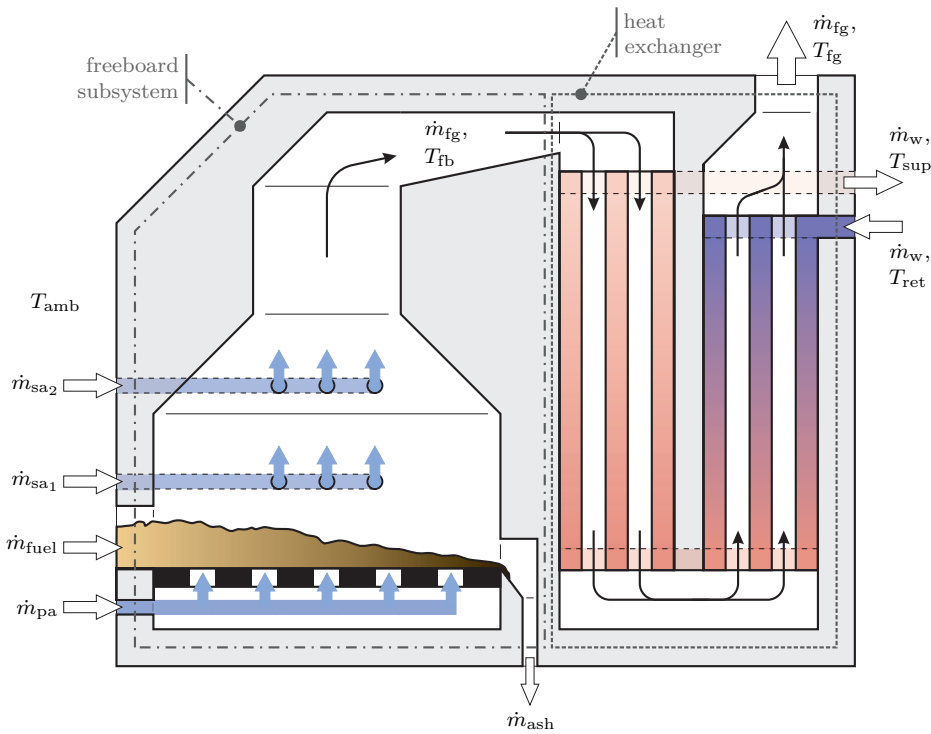


Figure 2.3: Basic furnace structure with mass flows and temperatures required for modelling. To facilitate allocation of equations, the model is divided into a freeboard and heat exchanger subsystem.

already exist in literature, whereby their applicability is discussed in the following section.

2.3 Modeling approaches from literature

To serve the intended comparative purpose, presented equations are depicted in their simplest possible formulation. Parameters that must be defined experimentally are referred to as k with consecutively numbered subscripts to facilitate distinction. Hereinafter, t in brackets denotes continuous-time values.

Böhler et al. [14] and Placek et al. [17] calculate the mass m_b of the fuel on the grate using the simple mass balance

$$\frac{d}{dt} m_b(t) = \dot{m}_{\text{fuel}}(t) - \dot{m}_{\text{thd}}(t) \quad (2.5)$$

with \dot{m}_{fuel} as the fuel mass flow fed onto the grate and \dot{m}_{thd} as the thermally converted mass flow induced by thermal decomposition of the biomass. Other authors [18, 19] suggest to consider the water mass flow $\dot{m}_{w,\text{in}}$ and the mass flow \dot{m}_{dfuel} of dry solid

biomass separately; relations are given by Eqs. (2.6) and (2.7).

$$\dot{m}_{w,\text{in}}(t) = w_{\text{H}_2\text{O}} \dot{m}_{\text{fuel}}(t - T_d(t)) \quad (2.6)$$

$$\dot{m}_{\text{dfuel}}(t) = (1 - w_{\text{H}_2\text{O}}) \dot{m}_{\text{fuel}}(t - T_d(t)) \quad (2.7)$$

An introduced dead time T_d according to

$$T_d(t) = k_1 \frac{m_w(t)}{(1 - w_{\text{H}_2\text{O}}) \dot{m}_{\text{fuel}}(t)} \quad (2.8)$$

accounts for fed mass flows to become effective after a certain delay in case of a long grate. Therefore, the water mass m_w on the grate is calculated by

$$\frac{d}{dt} m_w(t) = \dot{m}_{w,\text{in}}(t) - \dot{m}_{w,\text{ev}}(t) \quad (2.9)$$

with the steam mass flow $\dot{m}_{w,\text{ev}}$ given by the simple approach

$$\dot{m}_{w,\text{ev}}(t) = k_2 m_w(t). \quad (2.10)$$

In this modeling strategy, the mass m_{db} of dry solid fuel on the grate is calculated by

$$\frac{d}{dt} m_{\text{db}}(t) = \dot{m}_{\text{dfuel}}(t) - \dot{m}_{\text{thd}}(t). \quad (2.11)$$

Biomass combustion itself is modeled by several authors [14, 18, 20] using a simple approach according to

$$\dot{m}_{\text{thd}}(t) = k_2 \dot{m}_{\text{pa}}(t) m_b(t) \quad (2.12)$$

with the primary air mass flow \dot{m}_{pa} . In contrast, Placek et al. [17] utilize volume instead of mass flows, which induces an additional temperature dependency and therefore increases model complexity.

Much has been written about disrupted combustion models [21–23]. Such approaches provide comprehensive analytic insight but lack of simplicity, which is essential for the intended control purpose. As these models generally rely on a variety of unknown parameters, identification procedure would become even more challenging.

A majority of model approaches from literature [14, 17–20] cover the thermal dynamic inside the combustion chamber by an ordinary heat balance taking relevant in- and outputs into account. But, slight differences appear in the handling of heat losses. While [14] directly incorporates radiation losses \dot{Q}_{rad} by means of a simplified form of the Stefan-Boltzmann radiation law according to

$$\dot{Q}_{\text{rad}}(t) = k_3 T_{\text{fb}}^3(t), \quad (2.13)$$

others [17, 18] exclude such losses in general and only consider the storage effect of the furnace lining. The related heat flow \dot{Q}_r is defined as

$$\dot{Q}_r(t) = k_4 [T_{\text{fb}}(t) - T_r(t)] \quad (2.14)$$

with T_r as the temperature of the refractory lining. The differential equation

$$k_5 m_r \frac{d}{dt} T_r(t) = \dot{Q}_r(t) \quad (2.15)$$

with m_r as the mass of the refractory lining is then used to calculate T_r .

Since heat exchangers are the subject of extensive research, numerous models exist. However, only few approaches are simple enough to meet stated needs. While a simple heat balance always forms the basis, opinions differ in the matter of how to calculate the exhaust gas temperature T_{fg} . Böhler et al. [14] use a first order low pass filter, based on T_{fb} and an experimentally determined static gain, to define T_{fg} in an approximate manner. A promising way to reduce model order is outlined by Bauer et al. [24], since the heat flow \dot{Q}_W transferred in the heat exchanger is approximated without the need to calculate T_{fg} , see Eq. (2.16).

$$\dot{Q}_W(t) = k_6 [T_{fb}(t) - T_w(t)]^{k_7} \dot{m}_{fg}(t)^{k_8} \quad (2.16)$$

In this relation, T_w is the averaged water temperature in the heat exchanger and \dot{m}_{fg} labels the flue gas mass flow, which is simply calculated as a sum of all air inflows and the mass flow due to thermal decomposition of the biomass. Therefore, T_{fg} is given by an algebraic relation resulting from a steady heat balance of the recuperator.

2.4 Furnace model

The presented model is based on above discussed modeling approaches from literature (section 2.3) and adapted by appropriate terms to satisfy empirical findings gained from open-loop experiments. Thus, an iterative procedure containing modeling (section 2.4.1), parameter estimation and model validation (section 2.4.2) yields the final model structure. Please note that the following statements only consider the finally chosen furnace model and present results from single iterations only in an implicit manner.

2.4.1 Model equations

For the sake of readability, all relations that are necessary to obtain a specific physical quantity are grouped together.

Fuel mass on the grate

The current mass m_b of the dry and ash-free fuel on the grate is obtained by the solid mass balance

$$\frac{d}{dt} m_b(t) = \dot{m}_{\text{fuel,net}}(t) - \dot{m}_{\text{thd}}(t). \quad (2.17)$$

With the total fuel mass flow \dot{m}_{fuel} , water content $w_{\text{H}_2\text{O}}$ (Eq. 2.1), and ash content a_{ash} (Eq. 2.2), the dry and ash-free fuel mass flow $\dot{m}_{\text{fuel,net}}$ is defined according to

$$\dot{m}_{\text{fuel,net}}(t) = (1 - w_{\text{H}_2\text{O}}) (1 - a_{\text{ash}}) \dot{m}_{\text{fuel}}(t). \quad (2.18)$$

The mass flow due to thermal decomposition of the biomass, \dot{m}_{thd} , is calculated by

$$\dot{m}_{\text{thd}}(t) = k_{\text{thd}} (\dot{m}_{\text{pa}}(t) + \dot{m}_{\text{pa}0}) m_{\text{b}}(t), \quad (2.19)$$

where k_{thd} is the constant combustion rate, \dot{m}_{pa} the primary air mass flow, and $\dot{m}_{\text{pa}0}$ represents a constant air mass flow, which constantly passes the inlet.

Oxygen concentration in flue gas

Based on [2], the oxygen concentration O_2 in the flue gas after combustion is given by

$$T_{O_2} \frac{d}{dt} O_2(t) = 21 \text{ Vol.-%} \frac{\lambda(t) - 1}{\lambda(t)} + k_{R_{\text{thd}}} \frac{d}{dt} R_{\text{thd}}(t) - O_2(t), \quad (2.20)$$

where T_{O_2} is a time constant, λ the excess air ratio (see also Eq. 2.4), and R_{thd} an additional state to account for the all-pass behavior, which is apparent in open-loop experiments. Thereby, the factor $k_{R_{\text{thd}}}$ determines its contribution to the overall dynamic. The total air mass flow \dot{m}_{a} is specified according to

$$\dot{m}_{\text{a}}(t) = \dot{m}_{\text{pa}}(t) + \dot{m}_{\text{pa}0} + \dot{m}_{\text{sa}1}(t) + \dot{m}_{\text{sa}2}(t) \quad (2.21)$$

with the secondary air mass flows $\dot{m}_{\text{sa}1}$ and $\dot{m}_{\text{sa}2}$. Resultant excess air ratio is then calculated by

$$\lambda(t) = \frac{\dot{m}_{\text{a}}(t)}{k_{\text{L}} L_{\text{min}} \dot{m}_{\text{thd}}(t)}, \quad (2.22)$$

where L_{min} is the stoichiometric air-to-fuel ratio that is necessary for complete combustion under ideal conditions and k_{L} a factor to respect real circumstances. A closer look at oxygen measurements obtained from open-loop experiments (see exemplary results in Fig. 2.4a at 50 min and in Fig. 2.4b at 18 min) reveals all-pass dynamic and therefore justifies the need for the additional state R_{thd} . Its dynamic is described by

$$\frac{d}{dt} R_{\text{thd}}(t) = \dot{m}_{\text{thd}}(t) - \zeta R_{\text{thd}}(t), \quad (2.23)$$

where $\zeta = 1 \cdot 1/\text{s}$ to ensure consistency regarding physical units.

Freeboard gas temperature

The freeboard temperature T_{fb} is calculated by the unsteady heat balance

$$m_{\text{g}} c_{\text{p,g}} \frac{d}{dt} T_{\text{fb}}(t) = \dot{Q}_{\text{in}}(t) + \dot{Q}_{\text{comb}}(t) - \dot{Q}_{\text{gas}}(t) - \dot{Q}_{\text{rad}}(t), \quad (2.24)$$

with m_{g} as the gas mass in the chamber, $c_{\text{p,g}}$ the specific heat capacity of the combustion gas at elevated temperatures, \dot{Q}_{in} the incoming enthalpy flow accompanied by the air and fuel mass flow, \dot{Q}_{comb} the heat released by combustion, \dot{Q}_{gas} the enthalpy flow related to the gas mass leaving the freeboard, and \dot{Q}_{rad} the heat loss due to radiation.

With $c_{p,a}$ and $c_{p,\text{fuel}}$ as the specific heat capacities of the ambient air and the fuel, respectively, and T_{amb} as the ambient air temperature, the incoming enthalpy flow can be written as

$$\dot{Q}_{\text{in}}(t) = \dot{m}_a(t) c_{p,a} T_{\text{amb}} + \dot{m}_{\text{fuel}}(t) c_{p,\text{fuel}} T_{\text{amb}}. \quad (2.25)$$

Using the calorific value $q_{\text{gr-ah,af}}$, introduced by Eq. (2.3), and the specific evaporation enthalpy ΔH_e , the combustion heat is written as

$$\dot{Q}_{\text{comb}}(t) = \dot{m}_{\text{thd}}(t) q_{\text{gr-ah,af}} - \dot{m}_{\text{fuel}}(t) w_{\text{H}_2\text{O}} \Delta H_e. \quad (2.26)$$

Since the flue gas mass flow \dot{m}_{fg} is calculated according to

$$\dot{m}_{\text{fg}}(t) = \dot{m}_{\text{thd}}(t) + \dot{m}_a(t), \quad (2.27)$$

the enthalpy flow related thereto is given by

$$\dot{Q}_{\text{gas}}(t) = \dot{m}_{\text{fg}}(t) c_{p,g} T_{\text{fb}}(t). \quad (2.28)$$

Results of the iterative identification process have indicated increased model performance by adapting the Stefan-Boltzmann radiation law in such a sense that temperature will no longer be of fourth but rather third order, yielding heat loss \dot{Q}_{rad} to be described by

$$\dot{Q}_{\text{rad}}(t) = k_{\text{rad}} \sigma (T_{\text{fb}}^3(t) - T_{\text{amb}}^3) \quad (2.29)$$

with the Stefan-Boltzmann constant σ and the factor k_{rad} representing the thermally effective surface.

Supply water temperature

Based on the simplified approach presented in [24], the heat flow \dot{Q}_w transferred from the gas to the water side of the heat exchanger is calculated by

$$\dot{Q}_w(t) = k_{Q,1} [\dot{m}_{\text{fg}}(t) (T_{\text{fb}}(t) - T_w(t))]^{k_{Q,2}} + \dot{Q}_{\text{rec}}(t), \quad (2.30)$$

where $k_{Q,1}$ and $k_{Q,2}$ are constants used to appropriately shape the heat transfer, T_w is the mean water temperature within the heat exchanger, and \dot{Q}_{rec} accounts for a proportion of the heat loss \dot{Q}_{rad} that can be recuperated due to the given furnace design. Supply temperature T_{sup} and constant return temperature T_{ret} are used to approximate the mean water temperature according to

$$T_w(t) = \frac{T_{\text{sup}}(t) + T_{\text{ret}}}{2}. \quad (2.31)$$

Recuperated heat output \dot{Q}_{rec} is calculated by

$$\dot{Q}_{\text{rec}}(t) = k_{\text{rec}} \dot{Q}_{\text{rad}}(t), \quad (2.32)$$

where k_{rec} labels the recuperation ratio. The condition $k_{\text{rec}} \leq 1$ must hold, otherwise this term violates the principle of conservation of energy.

Therefore, the supply temperature T_{sup} is given by the empirically adapted heat balance

$$m_{\text{w,he}} c_{\text{p,w}} \frac{d}{dt} T_{\text{sup}}(t) = k_{\text{sup}} + \dot{Q}_{\text{w}}(t) - \dot{m}_{\text{w}} c_{\text{p,w}} (T_{\text{sup}}(t) - T_{\text{ret}}), \quad (2.33)$$

with $m_{\text{w,he}}$ as the effective mass of water inside the heat exchanger, $c_{\text{p,w}}$ the specific heat capacity of water, k_{sup} a constant temperature offset, and \dot{m}_{w} the constant water mass flow in the heating circuit.

Exhaust gas temperature

Although the exhaust gas temperature T_{fg} is only of minor importance for the control objective, its simple use in the identification procedure is appealing. An algebraic relation (Eq. 2.34), based on a stationary heat balance of the heat exchanger, is found to provide an even better model performance than given by an unsteady approach like reported in [14]. Temperature dependency yields the specific heat capacity $c_{\text{p,fg}}$ of the exhaust gas to be smaller than the one related to the freeboard temperature.

$$T_{\text{fg}}(t) = \frac{\dot{Q}_{\text{gas}}(t) + \dot{Q}_{\text{rec}}(t) - \dot{Q}_{\text{w}}(t)}{\dot{m}_{\text{fg}}(t) c_{\text{p,fg}}} \quad (2.34)$$

2.4.2 Model identification and validation

Parameters of the introduced non-linear model can be reasonably divided into three groups: the vector $\boldsymbol{\varphi}$ (Eq. 2.35) of known fuel related parameters, the vector $\boldsymbol{\chi}$ (Eq. 2.36) of all other known parameters, and the vector $\boldsymbol{\theta}$ (Eq. 2.37) of parameters not determined until now.

$$\boldsymbol{\varphi} = [w_{\text{H}_2\text{O}} \quad a_{\text{ash}} \quad q_{\text{gr-ah,af}}]^T \quad (2.35)$$

$$\boldsymbol{\chi} = [\dot{m}_{\text{pa},0} \quad \dot{m}_{\text{w}} \quad L_{\text{min}} \quad \Delta H_{\text{e}} \quad \sigma \quad \zeta \quad T_{\text{amb}} \quad T_{\text{ret}} \quad c_{\text{p,g}} \quad c_{\text{p,a}} \quad c_{\text{p,fuel}} \quad c_{\text{p,w}}]^T \quad (2.36)$$

$$\boldsymbol{\theta} = [k_{\text{thd}} \quad k_{\text{Rthd}} \quad k_{\text{L}} \quad k_{\text{rad}} \quad k_{\text{rec}} \quad k_{\text{sup}} \quad k_{\text{Q},1} \quad k_{\text{Q},2} \quad T_{\text{O}_2} \quad m_{\text{g}} \quad m_{\text{w,he}}]^T \quad (2.37)$$

Open-loop experiments, utilized for identification and validation, are obtained by combustion of wooden pellets. Experimental analyses [16, 25, 26] reveal the following fuel properties

$$\boldsymbol{\varphi}_{\text{pellets}} = [7.43 \text{ wt.-%} \quad 0.3 \text{ wt.-%} \quad 20348 \text{ J/g}]^T. \quad (2.38)$$

Elements of $\boldsymbol{\chi}$ are either natural constants, directly determined by measurement, calculated from reaction stoichiometry, or taken from substance tables - see numerical values presented in Table 2.1.

Table 2.1: Numerical values of known model parameters collected in $\boldsymbol{\chi}$.

variable	value	unit	variable	value	unit
$\dot{m}_{\text{pa},0}$	2	kg/h	T_{ret}	60	°C
\dot{m}_{w}	4000	kg/h	$c_{\text{p},a}$	1.01	J/(g K)
L_{min}	5.04	g _{air} /g _{fuel}	$c_{\text{p},\text{fuel}}$	1.80	J/(g K)
ΔH_{e}	2440	J/g	$c_{\text{p},\text{w}}$	4.19	J/(g K)
σ	$5.67 \cdot 10^{-8}$	W/(m ² K ⁴)	$c_{\text{p},\text{g}}$	1.30	J/(g K)
ζ	1	1/s	$c_{\text{p},\text{fg}}$	1.08	J/(g K)
T_{amb}	25	°C			

In order to determine the unknown parameters collected in $\boldsymbol{\theta}$, five open-loop measurements are used for training and four other data sets for validation. The identification purpose dictates the model formulation to rely on the input vector $\boldsymbol{u}_{\text{id}}$ according to

$$\boldsymbol{u}_{\text{id}}(k) = [\dot{m}_{\text{sa}2}(k) \quad \dot{m}_{\text{sa}1}(k) \quad \dot{m}_{\text{fuel}}(k) \quad \dot{m}_{\text{pa}}(k)]^T \quad (2.39)$$

and the output vector $\boldsymbol{y}_{\text{id}}$ given as

$$\boldsymbol{y}_{\text{id}}(k) = [T_{\text{fb}}(k) \quad O_2(k) \quad T_{\text{sup}}(k) \quad T_{\text{fg}}(k)]^T. \quad (2.40)$$

Please note that k denotes the k -th element within a certain data set of N elements in total. Therefore, the measured results (labeled by suffix m) of one experiment can be written in the abbreviated form Z^N as depicted in Eq. (2.41).

$$Z^N = \left\{ [\boldsymbol{u}_{\text{id},m}(k), \boldsymbol{y}_{\text{id},m}(k)], k = 1, \dots, N \right\} \quad (2.41)$$

In this work, model parameterization is carried out by utilizing the optimization-toolbox implemented in MATLAB[®], whereby a nonlinear least squares method, based on the Levenberg-Marquardt approach, is applied. While the actual used identification procedure considers all five open-loop measurements simultaneously, the following equations illustrate the basic procedure [27, 28] by means of one data set.

Based on the model output $\hat{\boldsymbol{y}}_{\text{id}}$, the cost function V_N related to the prediction error $\boldsymbol{\varepsilon}$ can be formulated as

$$\begin{aligned} V_N(\boldsymbol{\theta}, Z^N) &= \frac{1}{N} \sum_{k=1}^N [\boldsymbol{y}_{\text{id},m}(k) - \hat{\boldsymbol{y}}_{\text{id}}(k, \boldsymbol{\theta})]^T \boldsymbol{W} [\boldsymbol{y}_{\text{id},m}(k) - \hat{\boldsymbol{y}}_{\text{id}}(k, \boldsymbol{\theta})] \\ &= \frac{1}{N} \sum_{k=1}^N \boldsymbol{\varepsilon}(k, \boldsymbol{\theta})^T \boldsymbol{\varepsilon}(k, \boldsymbol{\theta}) \end{aligned} \quad (2.42)$$

with \boldsymbol{W} as a diagonal weighting matrix used to emphasize individual outputs. Equation (2.43) depicts the main objective, which is to find a parameter vector $\hat{\boldsymbol{\theta}}$ that minimizes V_N .

$$\hat{\boldsymbol{\theta}} = \arg \min_{\boldsymbol{\theta}} V_N(\boldsymbol{\theta}, Z^N) \quad (2.43)$$

This optimization provides an iterative procedure of the form

$$\hat{\boldsymbol{\theta}}^{(i+1)} = \hat{\boldsymbol{\theta}}^{(i+1)}(Z_N, \hat{\boldsymbol{\theta}}^{(i)}) \quad (2.44)$$

to find an improved solution in the actual calculation step (i+1) based on the cost function V_N and the previously found estimation $\hat{\boldsymbol{\theta}}^{(i)}$. Gradient method as well as Newton's method rely on a direct expansion of the cost function (Eq. 2.42) as a Taylor series. As this is accompanied by either a low convergence rate (gradient method) or increased computation time and global convergence problems associated with the Hessian matrix (Newton's method), quasi-Newton approaches were developed. Thereby, expansion of the prediction error as a Taylor series, according to

$$\varepsilon(k, \boldsymbol{\theta}) \cong \varepsilon(k, \hat{\boldsymbol{\theta}}^{(i)}) + \left. \frac{\partial \varepsilon(k, \boldsymbol{\theta})}{\partial \boldsymbol{\theta}^T} \right|_{\boldsymbol{\theta}=\hat{\boldsymbol{\theta}}^{(i)}} (\boldsymbol{\theta} - \hat{\boldsymbol{\theta}}^{(i)}), \quad (2.45)$$

yields an approximated but always positive definite form of the Hessian matrix. Since the results related to this approximation are only valid in the vicinity of the current estimation $\hat{\boldsymbol{\theta}}^{(i)}$, Levenberg and Marquardt introduced an additional cost contribution to penalize large changes of $\hat{\boldsymbol{\theta}}$ within one iteration step, keeping

$$\left\| \hat{\boldsymbol{\theta}}^{(i+1)} - \hat{\boldsymbol{\theta}}^{(i)} \right\|_2 \quad (2.46)$$

small. Thus, the so defined cost function $J_N^{(i)}$ is given by

$$J_N^{(i)}(\boldsymbol{\theta}, Z^N) = \frac{1}{N} \sum_{k=1}^N \boldsymbol{\xi}(k, \boldsymbol{\theta}, \hat{\boldsymbol{\theta}}^{(i)})^T \mathbf{W} \boldsymbol{\xi}(k, \boldsymbol{\theta}, \hat{\boldsymbol{\theta}}^{(i)}) + \gamma^{(i)} \left[\boldsymbol{\theta} - \hat{\boldsymbol{\theta}}^{(i)} \right]^T \left[\boldsymbol{\theta} - \hat{\boldsymbol{\theta}}^{(i)} \right] \quad (2.47)$$

with the parameter γ to shape trade-off between prediction error minimization and changes of $\hat{\boldsymbol{\theta}}$. The mentioned term $\boldsymbol{\xi}(k, \boldsymbol{\theta}, \hat{\boldsymbol{\theta}}^{(i)})$ is defined as

$$\boldsymbol{\xi}(k, \boldsymbol{\theta}, \hat{\boldsymbol{\theta}}^{(i)}) = \varepsilon(k, \hat{\boldsymbol{\theta}}^{(i)}) - \boldsymbol{\Psi}(k, \hat{\boldsymbol{\theta}}^{(i)}) (\boldsymbol{\theta} - \hat{\boldsymbol{\theta}}^{(i)}), \quad (2.48)$$

where the local parameter sensitivity $\boldsymbol{\Psi}$ is given by

$$\boldsymbol{\Psi}(k, \hat{\boldsymbol{\theta}}^{(i)}) = \left. \frac{\partial \hat{\mathbf{y}}_{\text{id}}(k, \boldsymbol{\theta})}{\partial \boldsymbol{\theta}^T} \right|_{\boldsymbol{\theta}=\hat{\boldsymbol{\theta}}^{(i)}}. \quad (2.49)$$

Minimizing the cost function (Eq. 2.47) then yields the iterative Levenberg-Marquardt procedure. Since estimation-related descriptions should only serve a supplementary purpose within this work, Eq. (2.50) only depicts the optimization result schematically.

$$\frac{\partial J_N^{(i)}}{\partial \boldsymbol{\theta}} \stackrel{!}{=} \mathbf{0} \longrightarrow \hat{\boldsymbol{\theta}}^{(i+1)}(Z_N, \hat{\boldsymbol{\theta}}^{(i)}) \quad (2.50)$$

Table 2.2: Model parameters collected in θ . Numerical values are found by non-linear least squares method based on five training data sets.

variable	mean value	standard deviation	unit
k_{thd}	4.03	1.24	10^{-2} 1/g
$k_{R_{\text{thd}}}$	9.95	2.17	s Vol.-%/g
k_{L}	7.84	0.02	1
k_{rad}	2.30	0.01	$10^3 \text{ m}^2 \text{ K}$
k_{rec}	0.739	0.004	1
k_{sup}	1.33	0.01	10^3 W
$k_{Q,1}$	2.16	0.01	$\text{W (s/(g K))}^{k_{Q,2}}$
$k_{Q,2}$	0.928	0.002	1
m_{g}	311	2	kg
$m_{\text{w,he}}$	251	7	kg

Applying this search method to the non-linear furnace model and five training data sets indicates insufficient estimation of T_{O_2} . Subsequently, this parameter is excluded from the identification algorithm, whereby comprehensive estimations find

$$T_{\text{O}_2} = 16.7 \text{ min} \quad (2.51)$$

to provide suitable model performance. While table 2.2 comprises numerical values of the estimated parameters, Fig. 2.4a presents related simulation results compared with measurement values used for training. Validation is conducted by comparing simulation results with measurement data sets not used for identification, see Fig. 2.4b. Stated root mean squared error (RMSE) values provide a quantitative measure of model quality and emphasize promising overall performance.

Despite the additional state R_{thd} (Eq. 2.23) that allows consideration of experimentally captured all-pass behavior, the parameterized furnace model neglects this feature. However, closed-loop results presented later on exhibit no significant deficit related thereto. As it is furthermore implausible that a decrease in fuel mass flow causes a harsh oxygen decrease, the suspicion raises that these peaks are artifacts induced by inadequate access to manipulated variables within a short time span after a stepwise change in open-loop experiments. And since furnace accessibility has been enhanced between identification and closed-loop tests, insufficient mapping of this aspect can be ignored.

2.4.3 Applicability

The presented modeling approach comprises parameters related to physical quantities and therefore allows to capture various changes in furnace settings in an easy manner. While combustion of different fuels is usually associated with a new identification process, the introduced model can be adapted for this purpose by just changing the

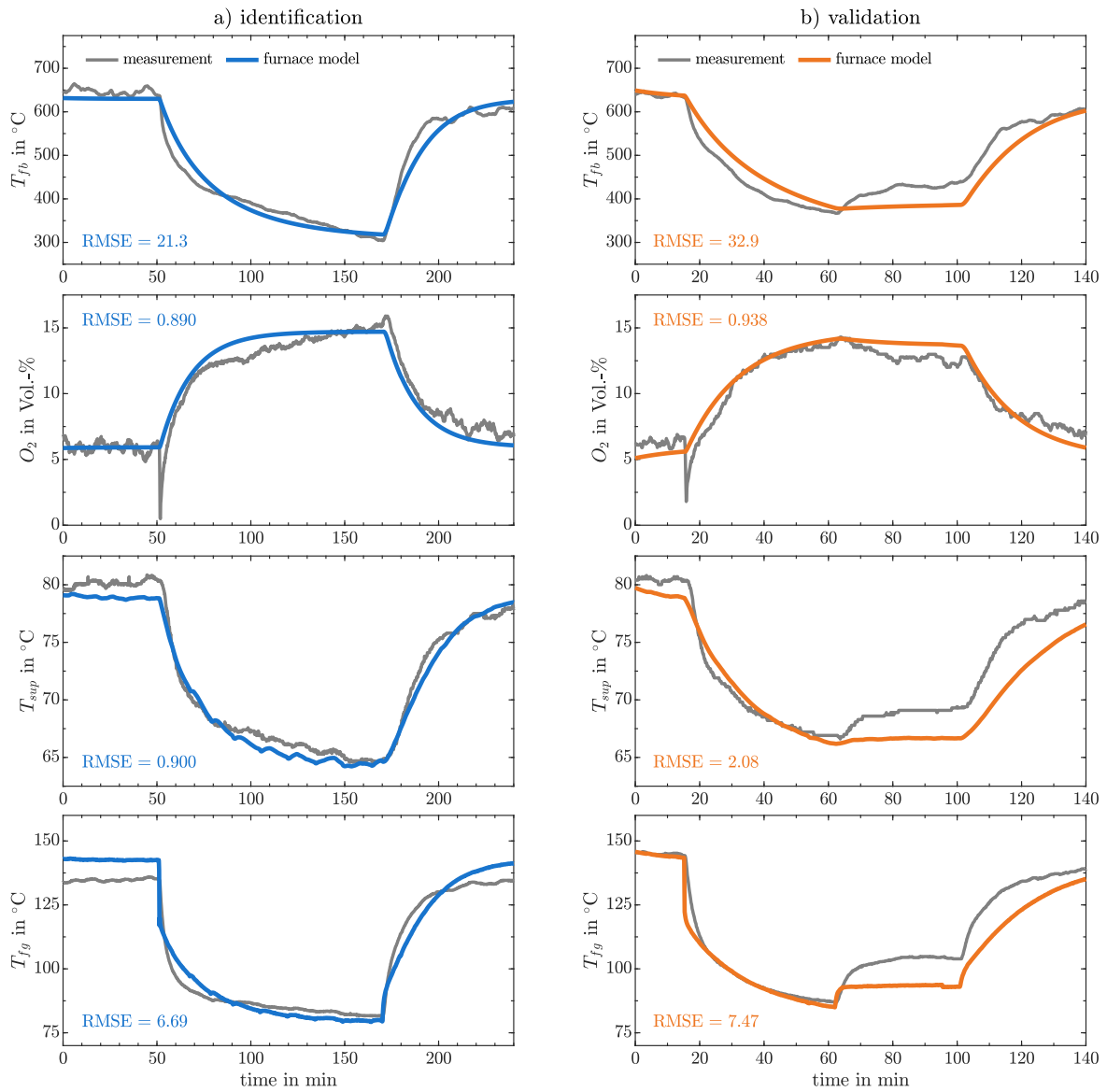


Figure 2.4: Simulation results of the non-linear furnace model compared to exemplary measurements used for (a) training and (b) validation. Root mean squared error (RMSE) serves as a model quality metric.

parameter vector φ (Eq. 2.35) appropriately. Section 4.2 outlines an experimental validation by utilizing wood chips with two different water contents instead of wooden pellets, which were already used for identification. Related fuel parameter vectors are given by Eqs. (2.52) and (2.53).

$$\varphi_{\text{chips-1}} = [35 \text{ wt.-%} \quad 0.3 \text{ wt.-%} \quad 19825 \text{ J/g}]^T \quad (2.52)$$

$$\varphi_{\text{chips-2}} = [20 \text{ wt.-%} \quad 0.3 \text{ wt.-%} \quad 19825 \text{ J/g}]^T \quad (2.53)$$

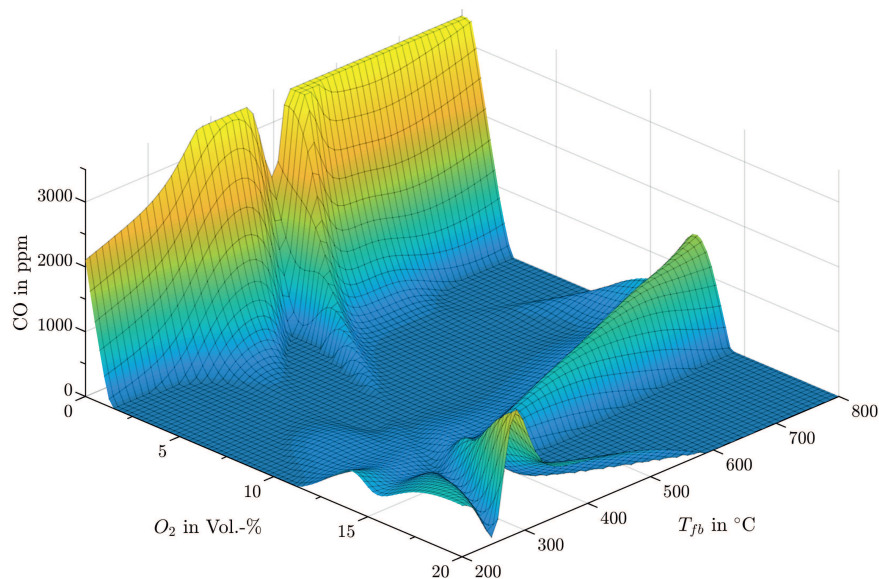


Figure 2.5: Graphical representation of the utilized CO model [15]. Sharp limit at 3500 ppm indicates sensor saturation.

2.5 Emission models

While the furnace model deals with O_2 , T_{fb} , and T_{sup} , emission formation is neglected but is at least equally important. Since CO is of vital importance to assess combustion efficiency (see section 2.1.2), an appropriate formation model would entail various application possibilities. Böhler et al. [15] found a static formation model to be suitable for the combustion of wooden pellets in the very same furnace investigated here. Fig. 2.5 depicts the relation, which relies on a neuronal network, between O_2 , T_{fb} , and CO. Besides for simulation purposes, this work takes advantage of this previous finding to determine emission-optimized reference values, see section 4.3.

Chapter 3

Controller design

The conceptual architecture used for controlling the investigated furnace is depicted in Fig. 3.1. Based on the furnace (section 2.4) covering the thermochemical conversion of biomass and necessary hardware elements, which translate electrical signals into mass flows, manufacturers often further enlarge furnace setups, aiming for simple handling of steady-state operation. Empirically evolved software supplements utilized for this purpose together with the basic hardware constitute the extended furnace (section 3.1). In order to maintain embedded empirical knowledge, any intended controller must cope with such an at least partly circumstantial environment. Hereinafter, this manufacturer-specific setup including a feedforward controller (section 3.1.2) and an input interface (section 3.1.1) is assumed to be given and immutable.

To control the plant in its extended modification not only an observer (section 3.2.2) but also an additional interface (reference interface - section 3.2.3) support the intended MPC (section 3.2.1). On the one hand these additional algorithms enable and on the other hand facilitate the overall control task, whereby grouping them together in a block (extended controller - section 3.2) is reasonable.

Following paragraphs provide an understanding of furnace-extending algorithms (section 3.1) followed by introducing the MPC in an appropriate formulation (section 3.2.1) and control-related supplements (sections 3.2.2 and 3.2.3).

3.1 Extended furnace

3.1.1 Input interface

The most common control strategy for small scale biomass furnaces is based on independently designed control loops using simple linear PI controllers [2]. To achieve sufficient control performance by applying such simple approach, decoupling of the process [29] and linear input-output behavior [30] are necessary prerequisites. Although satisfying both conditions simultaneously is hardly possible, the mainly static plant non-linearity enables a promising compromise. Its implementation together with the hardware components, which are used to supply the actual mass flows, constitutes the

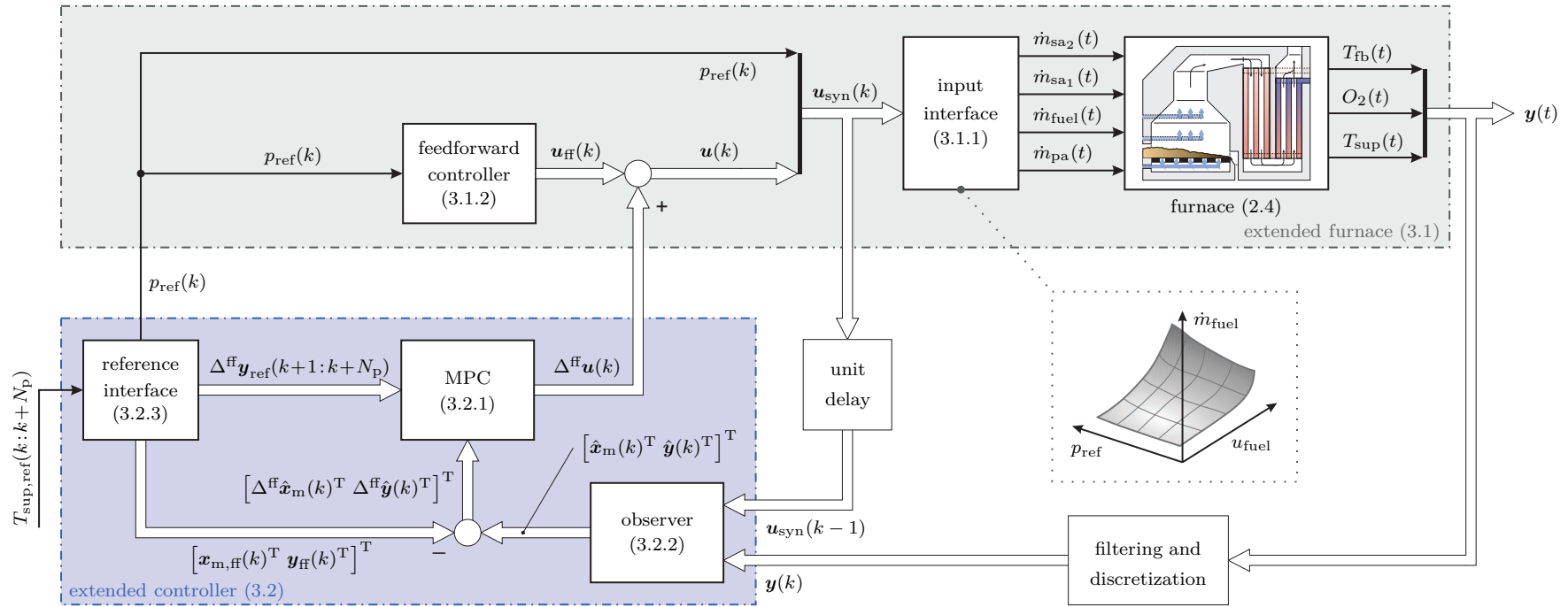


Figure 3.1: Conceptual architecture of the overall control structure. While presented furnace, its related input interface, and feedforward controller together constitute the extended furnace, the extended controller comprises an MPC, a state observer, and an interface calculating necessary reference values. Applied filtering and discretization transforms measured time-continuous output value $\mathbf{y}(t)$ into its time-discrete counterpart $\mathbf{y}(k)$. Numbers in brackets refer to sections describing the corresponding block.

input interface. A static but non-linear mapping according to

$$\mathbf{u}_{\text{syn}}(k) \mapsto [\dot{m}_{\text{sa}2}(t) \ \dot{m}_{\text{sa}1}(t) \ \dot{m}_{\text{fuel}}(t) \ \dot{m}_{\text{pa}}(t)]^T \quad (3.1)$$

between the newly defined synthetic input vector \mathbf{u}_{syn} and the actual mass flows serves as its mathematical description, also see the illustrative subfigure in Fig. 3.1 and section 3.1.2 including a simplified graphical representation (Fig. 3.3). For the sake of clarity, the current time $k T_s$ with T_s as the system sampling time is abbreviated by the actual time step k . The scalar synthetic input p_{ref} as part of

$$\mathbf{u}_{\text{syn}} = [p_{\text{ref}} \ \mathbf{u}^T]^T \quad (3.2)$$

represents the current heat demand on a percentage basis and influences the transformation in the input interface in such a non-linear way, that the process considering only the remaining synthetic input vector \mathbf{u} is decoupled and exhibits linear input-output behavior. As long as the actual heat output is close to the value according to the predefined input p_{ref} , these conditions are fulfilled in an appropriate but still approximate manner. Consequently, while $p_{\text{ref}}(k)$ is set only depending on the reference supply temperature $T_{\text{sup,ref}}(k)$, the controllable input vector diminishes and is defined as \mathbf{u} according to

$$\mathbf{u}^T = [u_{\text{fuel}} \ u_{\text{pa}} \ u_{\text{sa}}]. \quad (3.3)$$

For ease of readability, synthesized inputs, which basically lack of unambiguous physical interpretations, are labeled by indices referring to their main influence on the mass flows.

3.1.2 Feedforward controller

A feedforward controller only relying on the heat demand simultaneously combines simple operation with supplying an actual input vector \mathbf{u} enabling high combustion quality. However, this can only be guaranteed in case of a totally undisturbed furnace. Therefore, it is inevitable to adapt the input vector \mathbf{u}_{ff} , specified by feedforward control only, by a deviation $\Delta^{\text{ff}}\mathbf{u}$ based on feedback according to

$$\mathbf{u} = \mathbf{u}_{\text{ff}} + \Delta^{\text{ff}}\mathbf{u}. \quad (3.4)$$

While performing trajectory planning in dynamic feedforward control allows for designing the reference and disturbance behavior separately [31], here used static implementation

$$p_{\text{ref}}(k) \mapsto \mathbf{u}_{\text{ff}} = [u_{\text{fuel,ff}}(k) \ u_{\text{pa,ff}}(k) \ u_{\text{sa,ff}}(k)]^T, \quad (3.5)$$

graphically depicted in Fig. 3.2, shortens its versatility. Ignoring dynamic furnace behavior related thereto, obliges the feedback control to consider both, the reference and disturbance reaction in a deviation-related fashion. As the intended model predictive approach already includes the predictive property of trajectory planning inherently, a dynamic extension of the existing static feedforward controller would be redundant.

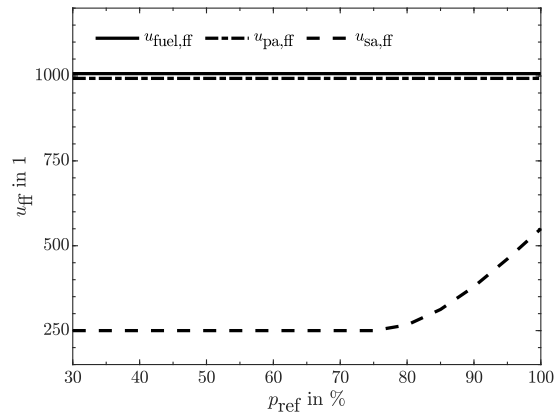


Figure 3.2: Static feedforward relationship (Eq. 3.5) between p_{ref} and items in \mathbf{u} .

Additionally, using Eq. (3.5) enables a simplified representation (Fig. 3.3) of relations comprised in the input interface - Eq. (3.1). For the sake of brevity, \dot{m}_{pa} and \dot{m}_{sa_1} are accumulated to one massflow \dot{m}_{psa} .

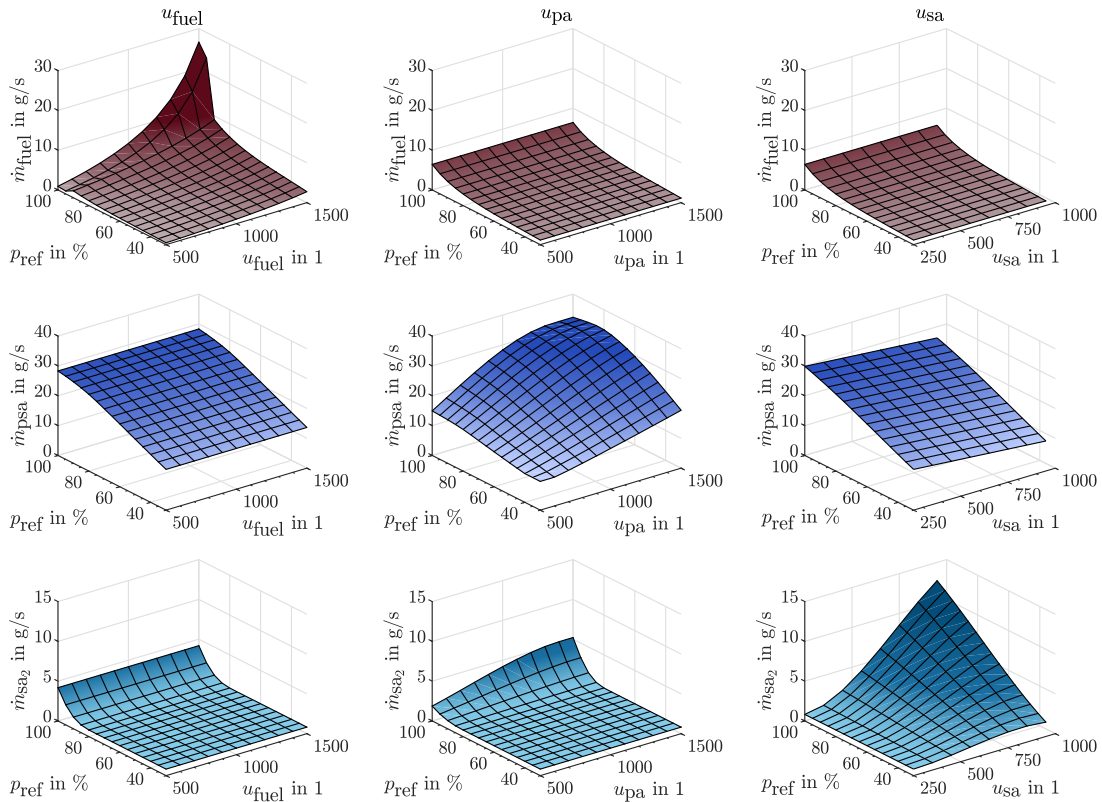


Figure 3.3: Relations within the input interface. While each column considers influence of p_{ref} and one item of $\mathbf{u} = [u_{fuel} \ u_{pa} \ u_{sa}]^T$, mass flows are organized line-by-line. Note that in each diagram the remaining values of \mathbf{u} are chosen according to Eq. (3.5), allowing depicted simplified representation.

3.2 Extended controller

3.2.1 MPC

Based on the state space representation of the augmented furnace (furnace and input interface) with the state vector $\mathbf{x}_m \in \mathbb{R}^{n_x}$, the output vector $\mathbf{y} \in \mathbb{R}^{n_y}$ according to Eq. (3.6), and the controllable input vector $\mathbf{u} \in \mathbb{R}^{n_u}$, Eq. (3.2), one linear MPC is established.

$$\begin{aligned}\mathbf{x}_m &= [m_b \ R_{\text{thd}} \ O_2 \ T_{\text{fb}} \ T_{\text{sup}}]^T \\ \mathbf{y} &= [T_{\text{fb}} \ O_2 \ T_{\text{sup}}]^T\end{aligned}\quad (3.6)$$

The deviation-related control setup gives rise to a demand for modifying the well known MPC formulation, see appendix A or [32], appropriately. Hereinafter, deviations from a chosen linearization point (subscript: L) are denoted by

$$\Delta^L(\star) = (\star) - (\star)_L, \quad (3.7)$$

where (\star) is a placeholder for the considered variable. Therefore, the discrete state space representation of the linearized model at time step k is given by

$$\begin{aligned}\Delta^L \mathbf{x}_m(k+1) &= \mathbf{A}_m \Delta^L \mathbf{x}_m(k) + \mathbf{B}_m \Delta^L \mathbf{u}(k) \\ \Delta^L \mathbf{y}(k) &= \mathbf{C}_m \Delta^L \mathbf{x}_m(k)\end{aligned}\quad (3.8)$$

with the system matrix $\mathbf{A}_m \in \mathbb{R}^{n_x \times n_x}$, the input matrix $\mathbf{B}_m \in \mathbb{R}^{n_x \times n_u}$, and the output matrix $\mathbf{C}_m \in \mathbb{R}^{n_y \times n_x}$. The wide range of steady-state operating points, which results from the whole operating range (30 to 100%) of the heat demand p_{ref} together with the feedforward controller, constitute all possible linearisation points. In order to compare different linear models regarding their ability to be controlled by a single linear algorithm, the ν -gap metric introduced by Vinnicombe [33] and applied by [14] for similar purposes offers an appropriate method (for more details about this procedure also see appendix C).

Therefore, Fig. 3.4 compares 20 linear models relying on different linearization points, which are unambiguously defined by their percentage heat demand $p_{\text{ref,L}}$ and chosen evenly distributed within the operating range. Gap metrics $\nu(\text{output}, \text{input})$ for all possible input-output combinations reveal that essentially p_{ref} -dependent relations incorporate restrictive non-linearities. But by neglecting p_{ref} as a controllable input, these models only differ slightly from each other in a ν -gap sense, underpinning above mentioned input-output linearization behavior of the input interface. Thus, the relation between \mathbf{u}_{fuel} and T_{fb} remains the critical one and is therefore used to find an appropriate linearization point by minimizing gap metric to all other linearized models within the operating range.

Thus, it can be concluded that one linear MPC is capable of controlling the furnace sufficiently. Furthermore, deviations from the finally chosen linearisation point are

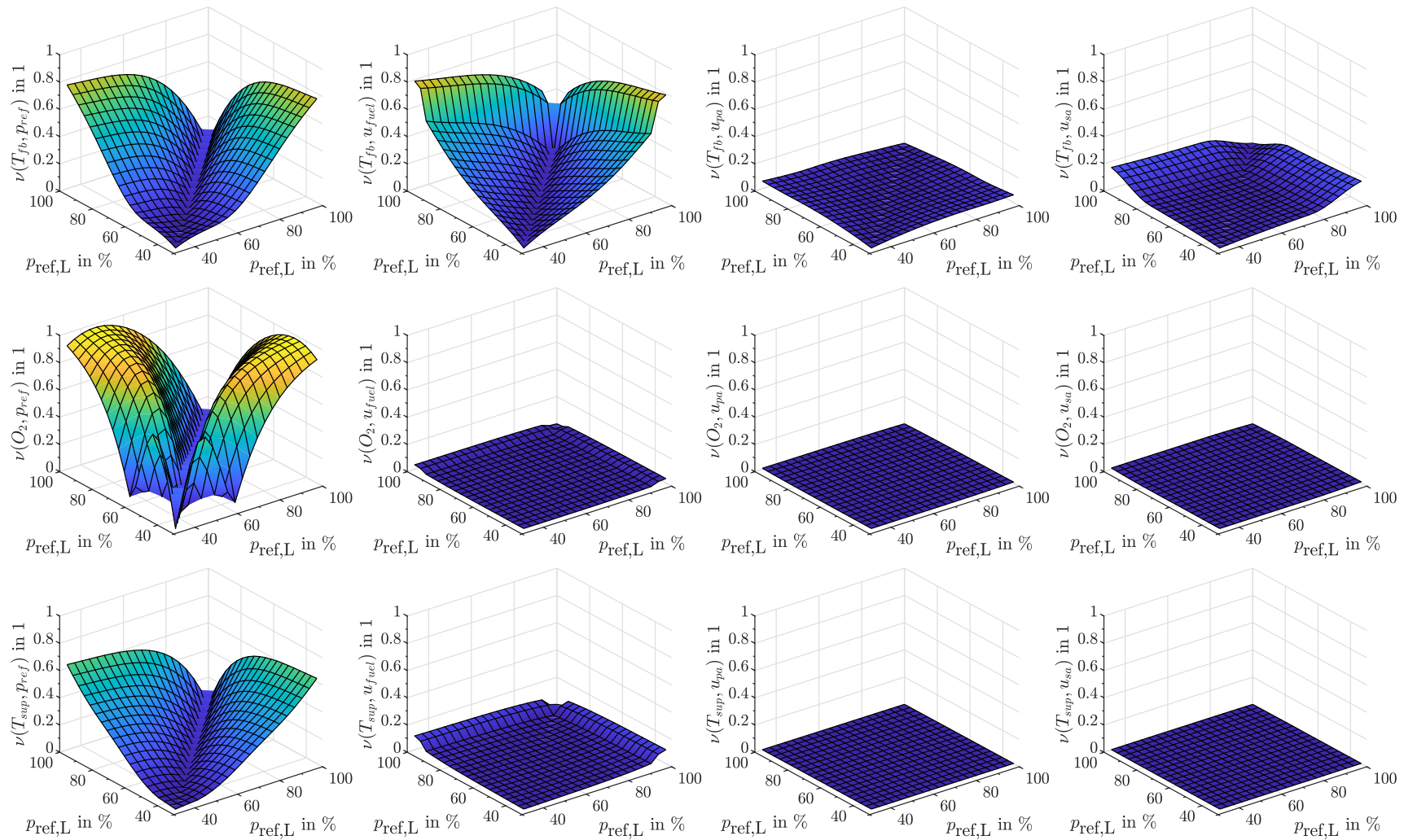


Figure 3.4: Gap metrics ν of all possible input-output combinations for 20 linear models of the furnace model enlarged by the input interface. While diagrams related to a certain item of the output vector \mathbf{y} are arranged line-by-line, each column represents influence of one specific item of the synthetic input vector \mathbf{u}_{syn} .

approximately equal to deviations from the steady-state operating point related to the actual feedforward control input \mathbf{u}_{ff} . Thus

$$\Delta^{\text{L}}(\star) \approx \Delta^{\text{ff}}(\star) = (\star) - (\star)_{\text{ff}} \quad (3.9)$$

with $\Delta^{\text{ff}}(\star)$ as the deviation from the feedforward-induced steady-state operating point $(\star)_{\text{ff}}$ holds for the whole operating range. Choosing the linearization point by minimizing the ν -gap value and using relation (3.9) yield the discrete state space representation shown in Eq. (3.10).

$$\begin{aligned} \Delta^{\text{ff}}\mathbf{x}_{\text{m}}(k+1) &= \mathbf{A}_{\text{m}} \Delta^{\text{ff}}\mathbf{x}_{\text{m}}(k) + \mathbf{B}_{\text{m}} \Delta^{\text{ff}}\mathbf{u}(k) \\ \Delta^{\text{ff}}\mathbf{y}(k) &= \mathbf{C}_{\text{m}} \Delta^{\text{ff}}\mathbf{x}_{\text{m}}(k) \end{aligned} \quad (3.10)$$

In order to eliminate steady-state offsets, the original plant model is augmented by adding n_{y} integrators. Applying the difference operation

$$\Delta(\star)(k+1) = \Delta^{\text{ff}}(\star)(k+1) - \Delta^{\text{ff}}(\star)(k) \quad (3.11)$$

the incremental formulation

$$\begin{aligned} \Delta\mathbf{x}_{\text{m}}(k+1) &= \mathbf{A}_{\text{m}} \Delta\mathbf{x}_{\text{m}}(k) + \mathbf{B}_{\text{m}} \Delta\mathbf{u}(k) \\ \Delta^{\text{ff}}\mathbf{y}(k+1) &= \Delta^{\text{ff}}\mathbf{y}(k) + \mathbf{C}_{\text{m}} \Delta\mathbf{x}_{\text{m}}(k+1) \end{aligned} \quad (3.12)$$

based on Eq. (3.10) is obtained. With the augmented state vector

$$\mathbf{x}(k) = \begin{bmatrix} \Delta\mathbf{x}_{\text{m}}(k) \\ \Delta^{\text{ff}}\mathbf{y}(k) \end{bmatrix}, \quad (3.13)$$

the state space representation of the augmented model is given by

$$\begin{aligned} \mathbf{x}(k+1) &= \mathbf{A}\mathbf{x}(k) + \mathbf{B}\Delta\mathbf{u}(k) \\ \Delta^{\text{ff}}\mathbf{y}(k) &= \mathbf{C}\mathbf{x}(k) \end{aligned} \quad (3.14)$$

with the matrices

$$\begin{aligned} \mathbf{A} &= \begin{bmatrix} \mathbf{A}_{\text{m}} & \mathbf{0}_{n_{\text{x}} \times n_{\text{y}}} \\ \mathbf{C}_{\text{m}}\mathbf{A}_{\text{m}} & \mathbf{I}_{n_{\text{y}}} \end{bmatrix}, \quad \mathbf{B} = \begin{bmatrix} \mathbf{B}_{\text{m}} \\ \mathbf{C}_{\text{m}}\mathbf{B}_{\text{m}} \end{bmatrix}, \\ \mathbf{C} &= \begin{bmatrix} \mathbf{0}_{n_{\text{y}} \times n_{\text{x}}} & \mathbf{I}_{n_{\text{y}}} \end{bmatrix}. \end{aligned} \quad (3.15)$$

Note that - providing a general statement by using a , b as substitutes - $\mathbf{0}_{a \times b}$ denotes a zero matrix of size $(a \times b)$ and \mathbf{I}_a denotes an identity matrix of size $(a \times a)$.

With N_{c} as the number of time steps within the control horizon and N_{p} the number of time steps within the prediction horizon, the vectors of stacked incremental inputs $\Delta\mathbf{U}$ and stacked predicted outputs \mathbf{Y} are defined by

$$\Delta\mathbf{U} = \left[\Delta\mathbf{u}(k)^{\text{T}} \quad \Delta\mathbf{u}(k+1)^{\text{T}} \quad \dots \quad \Delta\mathbf{u}(k+N_{\text{c}}-1)^{\text{T}} \right]^{\text{T}} \quad (3.16)$$

$$\mathbf{Y} = \left[\Delta^{\text{ff}}\mathbf{y}(k+1|k)^{\text{T}} \quad \Delta^{\text{ff}}\mathbf{y}(k+2|k)^{\text{T}} \quad \dots \quad \Delta^{\text{ff}}\mathbf{y}(k+N_{\text{p}}|k)^{\text{T}} \right]^{\text{T}}, \quad (3.17)$$

respectively. Thus, the prediction can be written compactly in the form of

$$\mathbf{Y} = \mathbf{F}\mathbf{x}(k) + \Phi \Delta \mathbf{U}, \quad (3.18)$$

where the matrices are given as

$$\mathbf{F} = \left[(\mathbf{CA}^1)^T \quad (\mathbf{CA}^2)^T \quad \dots \quad (\mathbf{CA}^{N_p})^T \right]^T \quad (3.19)$$

$$\Phi = \begin{bmatrix} \mathbf{CB} & \mathbf{0}_{n_y \times n_u} & \dots & \mathbf{0}_{n_y \times n_u} \\ \mathbf{CAB} & \mathbf{CB} & \dots & \mathbf{0}_{n_y \times n_u} \\ \mathbf{CA}^2 \mathbf{B} & \mathbf{CAB} & \dots & \mathbf{0}_{n_y \times n_u} \\ \vdots & & & \\ \mathbf{CA}^{N_p-1} \mathbf{B} & \mathbf{CA}^{N_p-2} \mathbf{B} & \dots & \mathbf{CA}^{N_p-N_c} \mathbf{B} \end{bmatrix} \quad (3.20)$$

With \mathbf{Y}_{ref} as the vector of stacked references within the prediction horizon according to

$$\mathbf{Y}_{\text{ref}} = \left[\Delta^{\text{ff}} \mathbf{y}_{\text{ref}}(k+1)^T \quad \Delta^{\text{ff}} \mathbf{y}_{\text{ref}}(k+2)^T \quad \dots \quad \Delta^{\text{ff}} \mathbf{y}_{\text{ref}}(k+N_p)^T \right]^T \quad (3.21)$$

the cost function J for optimization is determined by

$$J = \Delta \mathbf{U}^T \mathbf{R}_u \Delta \mathbf{U} + (\mathbf{Y}_{\text{ref}} - \mathbf{Y})^T \mathbf{Q}_y (\mathbf{Y}_{\text{ref}} - \mathbf{Y}) + J_{\text{sc}}, \quad (3.22)$$

where the term J_{sc} accounts for additional costs due to soft constraints and is yet to be defined. The weighting matrices \mathbf{R}_u , representing costs for increasing control inputs, and \mathbf{Q}_y , penalizing control errors, are structured as

$$\mathbf{R}_u = \text{diag}(\underbrace{[\mathbf{r}_u \quad \mathbf{r}_u \quad \dots \quad \mathbf{r}_u]}_{N_c \text{ times}}), \quad \mathbf{Q}_y = \text{diag}(\underbrace{[\mathbf{q}_y \quad \mathbf{q}_y \quad \dots \quad \mathbf{q}_y]}_{N_p \text{ times}}) \quad (3.23)$$

with

$$\mathbf{r}_u = \text{diag}([r_{\text{fuel}} \quad r_{\text{pa}} \quad r_{\text{sa}}]), \quad \mathbf{q}_y = \text{diag}([q_{T_{\text{fb}}} \quad q_{O_2} \quad q_{T_{\text{sup}}}], \quad (3.24)$$

comprising the scalar weighting factors for each in- and output, respectively. Minimizing the cost function (3.22) without considering any constraints yields the optimal control sequence $\Delta \mathbf{U}^*$ according to

$$\Delta \mathbf{U}^* = \left(\Phi^T \mathbf{Q}_y \Phi + \mathbf{R}_u \right)^{-1} \Phi^T \mathbf{Q}_y (\mathbf{Y}_{\text{ref}} - \mathbf{F}\mathbf{x}(k)). \quad (3.25)$$

However, various real plant conditions could require restrictions of the possible solution space. As system identification conducted to estimate model parameters mostly relies on data from furnace operation in the vicinity of steady-state operating points, a constraint on the amplitude of $\Delta^{\text{ff}} \mathbf{u}$ is reasonable. The limits

$$\Delta^{\text{ff}} \mathbf{u}_{\{\text{min}, \text{max}\}} = \begin{bmatrix} \Delta^{\text{ff}} u_{\text{fuel}, \{\text{min}, \text{max}\}} \\ \Delta^{\text{ff}} u_{\text{pa}, \{\text{min}, \text{max}\}} \\ \Delta^{\text{ff}} u_{\text{sa}, \{\text{min}, \text{max}\}} \end{bmatrix} \quad (3.26)$$

must be chosen with respect to the absolute limits of \mathbf{u} . Based on vector $\Delta^{\text{ff}}\mathbf{U}$, combining the deviation-related inputs within the control horizon, according to

$$\Delta^{\text{ff}}\mathbf{U} = \begin{bmatrix} \Delta^{\text{ff}}\mathbf{u}(k) \\ \Delta^{\text{ff}}\mathbf{u}(k+1) \\ \vdots \\ \Delta^{\text{ff}}\mathbf{u}(k+N_c-1) \end{bmatrix} = \mathbf{T}_{u,1} \Delta^{\text{ff}}\mathbf{u}(k-1) + \mathbf{T}_{u,2} \Delta\mathbf{U} \quad (3.27)$$

with the matrices

$$\mathbf{T}_{u,1} = \begin{bmatrix} \mathbf{I}_{n_u} \\ \mathbf{I}_{n_u} \\ \vdots \\ \mathbf{I}_{n_u} \end{bmatrix} \quad \mathbf{T}_{u,2} = \begin{bmatrix} \mathbf{I}_{n_u} & \mathbf{0}_{n_u \times n_u} & \cdots & \mathbf{0}_{n_u \times n_u} \\ \mathbf{I}_{n_u} & \mathbf{I}_{n_u} & \cdots & \mathbf{0}_{n_u \times n_u} \\ \vdots & \vdots & \ddots & \vdots \\ \mathbf{I}_{n_u} & \mathbf{I}_{n_u} & \cdots & \mathbf{I}_{n_u} \end{bmatrix}, \quad (3.28)$$

adduced hard input constraints are expressed as

$$\mathbf{T}_{u,1} \Delta^{\text{ff}}\mathbf{u}_{\min} \leq \Delta^{\text{ff}}\mathbf{U} \leq \mathbf{T}_{u,1} \Delta^{\text{ff}}\mathbf{u}_{\max}. \quad (3.29)$$

Because CO emissions strongly increase, if oxygen concentration falls below certain values (see Fig. 2.2 and [15]), a bottom limit is required. Compared with input-related constraints, hard limitations of output or state values could restrict feasibility of the optimization problem. The vector of predicted deviation-related oxygen concentrations \mathbf{Y}_{O_2} is obtained by applying a transformation matrix \mathbf{T}_{O_2} on the vector of stacked predicted outputs \mathbf{Y} according to

$$\mathbf{Y}_{O_2} = \begin{bmatrix} \Delta^{\text{ff}}O_2(k+1|k) \\ \Delta^{\text{ff}}O_2(k+2|k) \\ \vdots \\ \Delta^{\text{ff}}O_2(k+N_p|k) \end{bmatrix} = \underbrace{\text{diag}([0 \ 1 \ 0, \ 0 \ 1 \ 0, \ \dots])}_{\mathbf{T}_{O_2}} \mathbf{Y}. \quad (3.30)$$

In order to ensure feasibility a slack variable $s \in \mathbb{R}^{0+}$ is introduced to weaken the intended bottom limit, yielding condition

$$\mathbf{Y}_{O_2} \geq \mathbf{Y}_{O_2,\min} - s \mathbf{1}_{N_p \times 1} \quad (3.31)$$

with $\mathbf{Y}_{O_2,\min}$ as the vector of minimum permissible oxygen concentrations within the prediction horizon. Note that $\mathbf{1}_{N_p \times 1}$ denotes a vector of ones with dimension $(N_p \times 1)$. Fig. 3.5 presents two possible approaches to specify future limits. While option (a) represents a constant limit $\Delta^{\text{ff}}O_{2,\min}$ relative to the steady-state oxygen concentration $O_{2,\text{ff}}$, resulting from feedforward control only, option (b) implies a constant absolute bottom limit $O_{2,\min}$, whereas their mathematical implementations are given by Eqs. (3.32a, 3.32b), respectively.

$$\mathbf{Y}_{O_2,\min} = \begin{cases} \mathbf{1}_{N_p \times 1} \Delta^{\text{ff}}O_{2,\min} & \cdots \text{ (a)} \\ \mathbf{1}_{N_p \times 1} O_{2,\min} - \mathbf{O}_{2,\text{ff}}^{\text{pred}} & \cdots \text{ (b)} \end{cases} \quad (3.32)$$

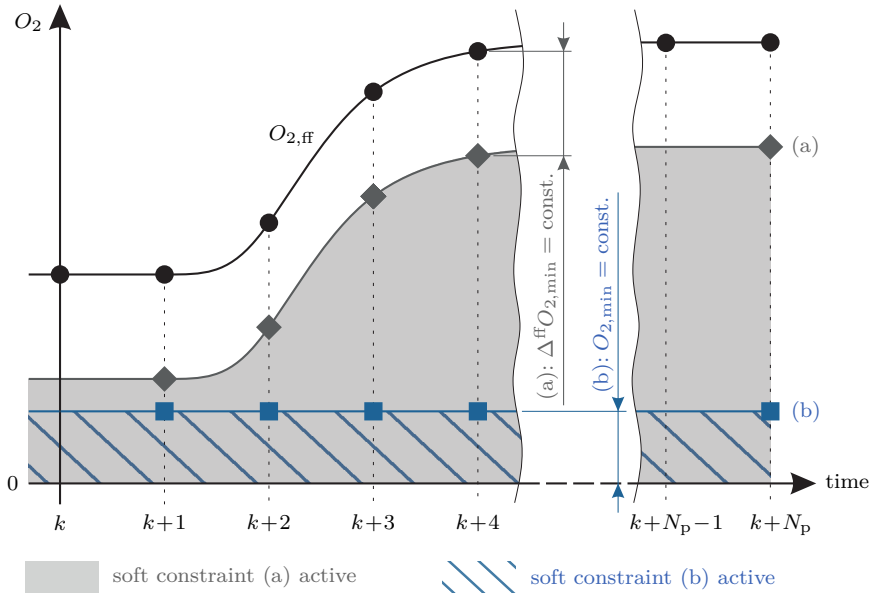


Figure 3.5: Constraint options acting on O_2 . While option (a) introduces a relative limit, option (b) restricts O_2 in an absolute fashion. Time-discrete values are connected smoothly to guide the eye.

Thereby, the vector $\mathbf{O}_{2,\text{ff}}^{\text{pred}}$ combines feedforward-induced steady-state oxygen concentrations $O_{2,\text{ff}}$ within the prediction horizon and is defined as

$$\mathbf{O}_{2,\text{ff}}^{\text{pred}} = [O_{2,\text{ff}}(k+1) \ O_{2,\text{ff}}(k+2) \ \dots \ O_{2,\text{ff}}(k+N_p)]^T. \quad (3.33)$$

Stated vector elements are obtained by using the reference interface, see section 3.2.3. Constraint option (a) represents a reasonable approach if feedforward control is designed to provide low-emission steady state operation. But as experimental results together with the CO model suggest much lower oxygen reference values than steady-state values obtained by feedforward control only, see section 4.3, absolute constraint option (b) becomes favorable.

Introducing additional costs J_{sc} according to

$$J_{sc} = c_1 s + c_2 s^2 \quad (3.34)$$

with $c_1, c_2 \in \mathbb{R}^{0+}$ allows influencing soft constraint's strength. Therefore, considering s as an additional decision variable and neglecting immutable terms in Eq. (3.22) yield the overall quadratic cost function

$$J = \begin{bmatrix} \Delta U \\ s \end{bmatrix}^T \mathbf{H} \begin{bmatrix} \Delta U \\ s \end{bmatrix} + \mathbf{f}^T \begin{bmatrix} \Delta U \\ s \end{bmatrix} \quad (3.35)$$

with the matrices

$$\mathbf{H} = \begin{bmatrix} \mathbf{R}_u + \Phi^T \mathbf{Q}_y \Phi & 0 \\ \mathbf{0}_{1 \times N_c n_u} & c_2 \end{bmatrix}, \quad (3.36)$$

$$\mathbf{f}^T = \left[-2(\mathbf{Y}_{\text{ref}} - \mathbf{F}\mathbf{x}(k)) \mathbf{Q}_y \Phi, \quad c_1 \right]. \quad (3.37)$$

Equation (3.35) subject to the constraints, rewritten as combined inequalities, expressed as

$$\begin{bmatrix} \mathbf{T}_{u,2} & \mathbf{0}_{N_c n_u \times 1} \\ -\mathbf{T}_{u,2} & \mathbf{0}_{N_c n_u \times 1} \\ -\mathbf{T}_{O_2} \Phi & -\mathbf{1}_{N_p \times 1} \\ \mathbf{0}_{1 \times N_c n_u} & -1 \end{bmatrix} \begin{bmatrix} \Delta \mathbf{U} \\ s \end{bmatrix} \leq \begin{bmatrix} \mathbf{T}_{u,1} (\Delta^{\text{ff}} \mathbf{u}_{\text{max}} - \Delta^{\text{ff}} \mathbf{u}(k-1)) \\ \mathbf{T}_{u,1} (-\Delta^{\text{ff}} \mathbf{u}_{\text{min}} + \Delta^{\text{ff}} \mathbf{u}(k-1)) \\ \mathbf{T}_{O_2} \mathbf{F}\mathbf{x}(k) - \mathbf{Y}_{O_2, \text{min}} \\ 0 \end{bmatrix} \quad (3.38)$$

constitutes the conclusive quadratic programming problem. By applying the receding horizon principle, deviation-related input vector $\Delta^{\text{ff}} \mathbf{u}$ at the actual time step k is set to

$$\begin{aligned} \Delta^{\text{ff}} \mathbf{u}(k) &= \Delta^{\text{ff}} \mathbf{u}(k-1) + \Delta \mathbf{u}(k) \\ &= \Delta^{\text{ff}} \mathbf{u}(k-1) + [\mathbf{I}_{n_u} \quad \mathbf{0}_{n_u \times n_u} \quad \dots \quad \mathbf{0}_{n_u \times n_u}] \Delta \mathbf{U}^* \end{aligned} \quad (3.39)$$

with $\Delta \mathbf{U}^*$ as the solution found by optimization.

3.2.2 Observer

Based on the furnace model including the input interface, an extended Kalman filter [34] is applied to estimate model states and therefore overcome lack of full state measurability. As the separation principle allows for independent controller and observer design, actual plant circumstances are considered to dictate appropriate covariance matrices of measurement and process noise.

Because the plant outputs correspond directly to model states, the observer provides on the one hand the estimated state vector $\hat{\mathbf{x}}_m(k)$ but on the other hand estimated plant outputs $\hat{\mathbf{y}}(k)$ as well. Since the Kalman filter accounts for corrupted signals, using estimated values and not raw measurement data as MPC inputs is favorable.

Appendix B supplies fundamentals of Kalman-filterung for the interested reader.

3.2.3 Reference interface

Furnace operators' main focus is obtaining a required supply temperature $T_{\text{sup,ref}}$ and heat demand P_{ref} related thereto, given as

$$P_{\text{ref}} = \dot{m}_w c_{p,w} (T_{\text{sup,ref}} - T_{\text{ret}}). \quad (3.40)$$

Because the supply temperature T_{sup} is directly measurable, it is chosen as the main reference and as in the given furnace setup an external control valve ensures a constant return temperature T_{ret} , the heat output is directly proportional to it anyway.

Besides controlling the heat output, it is equally important to provide high combustion quality accompanied by high efficiency and low emission formation. While legal constraints essentially restrict CO emissions [6, 7], their highly non-linear formation process complicates direct incorporation of CO as a control variable by using a simple

linear MPC. Nonetheless, a non-linear but static relation between CO, oxygen concentration O_2 , and freeboard temperature T_{fb} was found in a previous work [15] indicating that appropriately chosen reference values for O_2 and T_{fb} are sufficient to ensure low CO emissions. Furthermore, O_2 was found being the main influence on the formation process, which justifies common practice of realising emission control based on controlling O_2 only. Therefore, the reference interface as part of the extended controller must provide appropriate deviation-related reference vectors $\Delta^{\text{ff}}\mathbf{y}_{\text{ref}}$ according to

$$\Delta^{\text{ff}}\mathbf{y}_{\text{ref}} = \begin{bmatrix} \Delta^{\text{ff}}T_{\text{fb,ref}} \\ \Delta^{\text{ff}}O_{2,\text{ref}} \\ \Delta^{\text{ff}}T_{\text{sup,ref}} \end{bmatrix} = \mathbf{y}_{\text{ref}} - \mathbf{y}_{\text{ff}} \quad (3.41)$$

for every time step within the prediction horizon. Empiric or model based approaches yield the necessary relation, which is stored in tabular form and can be expressed as

$$T_{\text{sup,ref}}(k+1:k+N_p) \mapsto \mathbf{y}_{\text{ref}}(k+1:k+N_p) \quad (3.42)$$

using the notation

$$(\star)(a:a+b) = \begin{bmatrix} (\star)(a) \\ (\star)(a+1) \\ \dots \\ (\star)(a+b) \end{bmatrix} \quad (3.43)$$

with a , b as substitutes to provide a general statement. Section 4.3 offers detailed discussion on how to select references.

Because the control algorithm relies on a deviation-related formulation, absolute reference values, estimated state, and estimated output values must be related to corresponding steady-state values resulting from feedforward control only. For this purpose the reference interface incorporates feedforward-driven steady-state simulation results depending on the reference supply temperature. This can be expressed as

$$T_{\text{sup,ref}}(k) \mapsto \mathbf{x}_{\text{m,ff}}(k) \quad (3.44)$$

$$T_{\text{sup,ref}}(k:k+N_p) \mapsto \mathbf{y}_{\text{ff}}(k:k+N_p). \quad (3.45)$$

Using this data set enables calculation of all necessary deviations in every time step. Note that feedforward-induced steady-state oxygen concentrations, see Eq. (3.33), are inherently given as part of $\mathbf{y}_{\text{ff}}(k:k+N_p)$.

Additionally, the reference interface must provide p_{ref} , the actual heat demand on a percentage basis, according to

$$p_{\text{ref}}(k) = \frac{P_{\text{ref}}(k)}{P_{\text{nom}}} \quad (3.46)$$

as an input of the feedforward controller and input interface, where P_{nom} is the nominal furnace power.

Chapter 4

Results and discussion

In the following, results of the closed-loop introduced in section 3 are presented for combustion of different solid biofuels. While all used MPC configurations possess a prediction horizon with a length of $N_p = 180$ elements and a control horizon with a length of $N_c = 90$ elements, situation-specific demands dictate actual weighting matrices, which therefore may vary slightly from experiment to experiment. As providing a heat output, expressed as a required supply temperature T_{sup} , and enabling high combustion quality, related to a specific O_2 concentration, constitute the overarching objective, freeboard temperature T_{fb} must be considered more as a result of these demands rather than as an independent control variable. Therefore, its importance diminishes, which is represented by a negligibly small weighting. Unless otherwise stated, the weighting factors are set according to

$$\mathbf{r}_u = \text{diag}([r_{\text{fuel}} \ r_{\text{pa}} \ r_{\text{sa}}]) = \text{diag}([10 \ 2.5 \ 1]), \quad (4.1)$$

$$\mathbf{q}_y = \text{diag}([q_{T_{\text{fb}}} \ q_{O_2} \ q_{T_{\text{sup}}}] = \text{diag}([0.01 \ 0.75 \ 10]). \quad (4.2)$$

For all experiments the required supply temperature $T_{\text{sup,ref}}$ is chosen in a way to cover the whole power range that is accessible by the actual fuel. Further on, a constant system sampling time of $T_s = 10$ sec is used in each experiment, defining the prediction horizon to be of 30 min length.

4.1 Closed-loop results for wooden pellets

At first, without a deeper insight in emission formation it is reasonable to assume feedforward control to yield high steady-state combustion quality due to longstanding empirical improvements. Therefore, the initial approach relies on reference values \mathbf{y}_{ref} that are identical with output values \mathbf{y}_{ff} , which only result from feedforward control based on $T_{\text{sup,ref}}$ and correlated p_{ref} according to Eqs. (3.40) and (3.46). Related experimental output results for combustion of wooden pellets are depicted in the three upper diagrams of Fig. 4.1a.

Due to the purely static feedforward controller, harsh changes of p_{ref} directly cause rapid load changes on actuators. In order to prevent such excessive loads, the reference

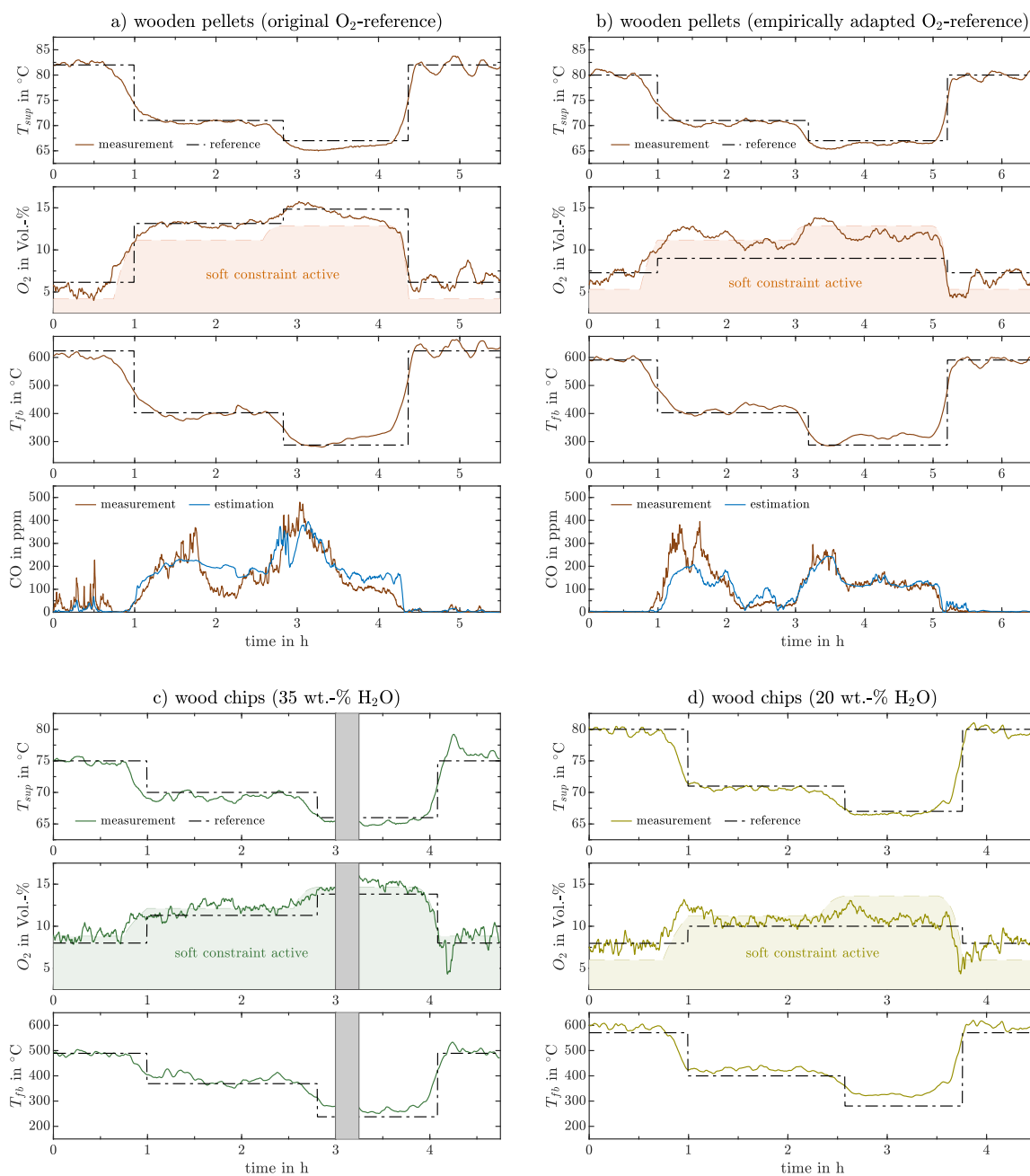


Figure 4.1: Experimental closed-loop output results obtained by utilizing introduced controller design for combustion of different solid biofuels. Output results as well as measured and estimated CO emissions for wooden pellets are conducted by applying (a) references according to $\Delta^{\text{ff}} \mathbf{y}_{\text{ref}} = \mathbf{0}$ and (b) an empirically adapted O_2 reference. Using wood chips with a water content of 35 wt.-% and 20 wt.-% yields results depicted in (c) and (d), respectively. Colored background highlights O_2 value ranges that cause additional costs due to violation of the implemented soft constraint. Grey areas in (c) indicate interruption due to automatic furnace cleaning.

interface incorporates a moving average filter with a window length of 90 time steps, corresponding to 15 min. Its purpose is to smooth changes of p_{ref} based on $T_{\text{sup,ref}}$ within the prediction horizon. Therefore, the applied relative oxygen constraint, according to Eqs. (3.31) and (3.32a) with $\Delta^{\text{ff}}O_{2,\text{min}} = 2 \text{ Vol.-%}$ and cost coefficients $c_1 = c_2 = 10$, possesses continuous changes starting 15 min before reference steps.

The results clearly indicate appropriate convergence towards reference values in steady state but also satisfying transition behavior, which is in agreement with simulation results shown in [14] for the very same furnace. Based on a comparison between the simulated closed-loop results using an MPC and the currently employed PI control strategy, which was additionally presented in [14], we can conclude that the implemented MPC offers significant improvements compared with classical control approaches. Among many other aspects, the penalizing effect of soft constraints contribute to this enhancement, whereas its influence is impressively illustrated in Fig. 4.1a as the oxygen concentration never falls significantly short of the applied limit.

Estimated CO emissions obtained according to section 2.5 exhibit good agreement with measured values, see bottom diagram of Fig. 4.1a. However, considerable amount of CO emissions, especially occurring in the lower power range, indicates chosen references to be inappropriate in terms of low emissions. Peaks in the first hour are associated with low oxygen concentrations, while increased CO emissions in the time span between 1 h and 4 h 15 min could result either from a low freeboard temperature T_{fb} or a high O_2 concentration. As increasing T_{fb} and keeping track of the given supply temperature reference $T_{\text{sup,ref}}$ are contradictory to each other, emission formation can only be influenced by adapting the remaining O_2 reference. In case of a constant fuel mass flow an increase in the O_2 concentration is related to increased air mass flows and therefore a shorter residence time in the chamber. This favors incomplete combustion, especially if a low freeboard temperature inhibits reaction time.

These observations suggest to increase the O_2 reference during high power periods and decrease it in lower power regions. Maintaining the same controller configuration but applying such an empirically adapted O_2 reference yield closed-loop results depicted in Fig. 4.1b. While experimental results confirm intended emission reduction, insufficient line-out of the O_2 concentration to the given set point stands out. Due to the unchanged soft limit implementation, still done in a simple relative fashion, actual references are partly situated within the constrained value range. Subsequently, minimizing control error would cause additional costs related to constraint violation, forcing optimization to find a compromise between these opposing cost contributions.

Therefore, the simple constraint implementation according to Eq. (3.32a) turns out to be obstructive for emission reduction, calling for an absolute bottom limit as introduced by Eq. (3.32b). Apart from that, CO minimization requires a methodical rather than the above-presented empirical approach to determine O_2 references. Based on both aspects, section 4.3 covers closed-loop simulations presenting a promising approach to achieve emission reduction.

4.2 Fuel flexibility

Although the investigated furnace is mainly designed for the combustion of wooden pellets, minor changes in furnace settings allow other solid biofuels to be utilized as well. Up to now, such a fuel switch includes adaption of actuator's working ranges followed by potentially protracted and therefore cost-intensive controller adjustments to account for differing fuel properties.

However, the presented analytic modeling approach (section 2.4) provides benefits, since model parameters related to the fuel and furnace settings can be adapted easily without a new parameter identification. Adapting the model parameters in the above stated sense for combustion of wooden pellets with a water content of 35 wt.-% and 20 wt.-% yields closed-loop output results displayed in Figs. 4.1c and 4.1d, respectively. Oxygen references, which are considered to be only of secondary importance in this paragraph (main focus lies on fuel flexibility), were chosen in an empirically based style similar to Fig. 4.1b.

All in all, results for combustion of wood chips with a water content of 35 wt.-% (Fig. 4.1c) show a satisfying control performance by utilizing introduced controller settings unaltered. Applying slight changes in weighting factors (Eqs. 4.1 and 4.2) according to

$$r_{pa} = 0.5, \quad q_{O_2} = 3 \quad (4.3)$$

yields results depicted in Fig. 4.1d. This adjustment was introduced to increase costs related to insufficient line-out behavior of oxygen relative to the contribution accounting for violating the soft constraint. This helps to overcome still inadequate relative constraint formulation. Nonetheless, further experiments using the initial weightings demonstrated comparable results (not shown in this work). Due to the overlapping O_2 constraint, the control error of oxygen would just increase slightly in the time span between 2 h 30 min and 3 h 45 min.

On the whole, one MPC configuration is capable of controlling combustion of different solid biofuels by just replacing model parameters appropriately, providing a fast and cost-effective approach for fuel switches. This novel application additionally confirms validity of the introduced model structure and emphasizes its versatile application possibilities.

4.3 Emission reduced control

While above considerations highlight the importance of an appropriately chosen O_2 reference in order to reduce CO emissions, lack of a systematic determination lets optimization remain empirically driven. But, besides applying the introduced CO model (section 2.5) for simulation purposes, its purely static relation between O_2 , T_{fb} , and CO offers a simple approach to find optimal references. Minimizing the CO emissions, based on this model, yields an emission-optimal O_2 reference for a given T_{fb} reference.

Using the CO model of the actual furnace under investigation a constant O_2 reference of 7 Vol.-% was found to fulfill this objective. The model additionally reveals that O_2 concentrations below 5 Vol.-% favor excessively high CO formation, providing the reasonable absolute bottom limit of $O_{2,\min} = 5$ Vol.-% as part of the soft constraint according to Eqs. (3.31) and (3.32b).

Based on these suggestions a closed-loop simulation was carried out, see Fig. 4.2, and compared to already depicted results obtained by applying an empirically adapted O_2 reference (Fig. 4.1b). To improve distinguishability, experimental and simulated O_2 results are shown separately in Figs. 4.2b and 4.2c. Results of T_{fb} are omitted, since they are only of secondary importance. Simulation utilizes an adapted MPC configuration according to

$$\mathbf{r}_u = \text{diag}([2.5 \ 2.5 \ 1]), \quad (4.4)$$

$$\mathbf{q}_y = \text{diag}([0.01 \ 20 \ 20]) \quad (4.5)$$

to stronger account for demonstrated importance of the O_2 concentration and to facilitate influence on the fuel mass flow, enhancing control performance. Furthermore, constraint's cost coefficients are now set to $c_1 = c_2 = 10^5$ to harden the introduced absolute bottom limit.

While shorter transition periods of T_{sup} for the first two reference steps confirm higher control performance, the third reference step, which is related to a change in heat demand from minimum to maximum, is marked by a higher rise time, see Fig. 4.2a. As the residual O_2 concentration immediately prior to the third reference step is intentionally lower in simulation than in experiment, the MPC inhibits harsh changes to keep track of the O_2 reference and to ensure the required minimum O_2 concentration. This intensified oxygen orientation provides intended emission reduction (Fig. 4.2d), whereas the higher peak at 5 h 10 min results from the static CO model, which is not able to handle highly dynamic transitions sufficiently. Experimental data support this statement since even lower oxygen concentrations being apparent during the last transition period cause by far lower CO emissions than simulated. Note that this argumentation is valid as the freeboard temperatures obtained by experiment and simulation are almost identical during the considered time span. Therefore, further research is needed to provide a comprehensive insight in emission formation dynamics. However, the chosen configuration setup provides an appealing compromise between emission peaks and control performance, suitable for most practical applications.

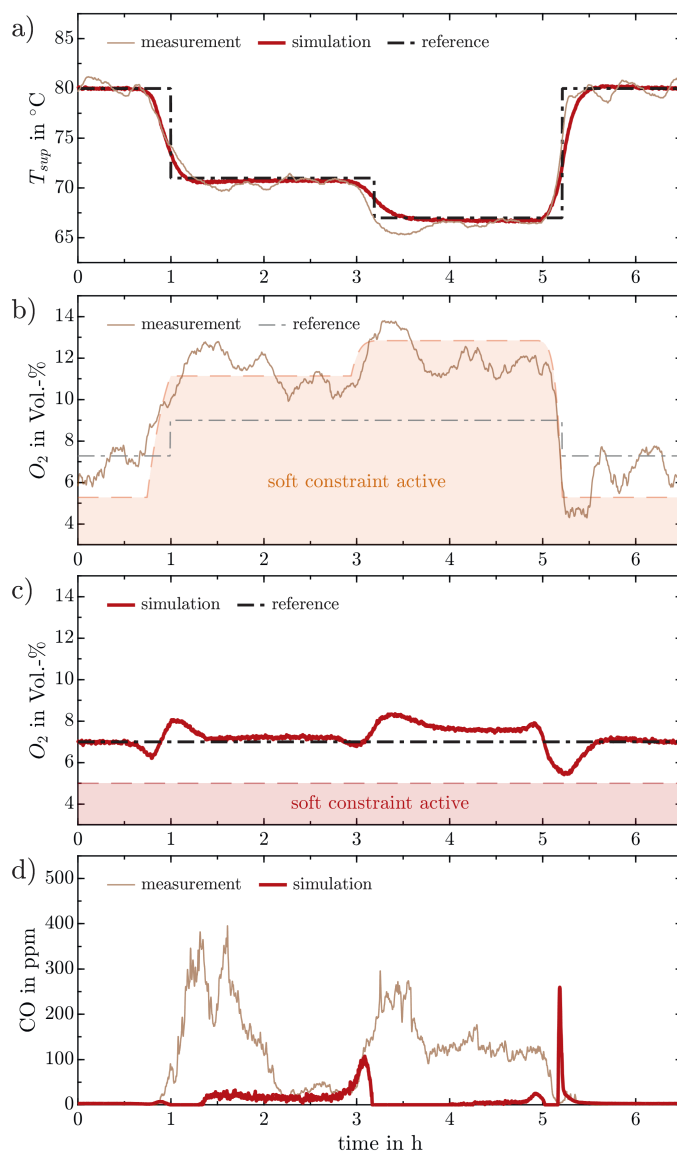


Figure 4.2: Experimental closed-loop results for combustion of wooden pellets and applying an empirically adapted O_2 reference (data already shown in Fig. 4.1b) are compared with simulation results obtained by adapting the O_2 reference in a model-based fashion, implementing an absolute O_2 soft constraint, and adjusting MPC's weighting matrices. Whilst experimental and simulation results for T_{sup} and CO are compared in (a) and (d), respectively, O_2 results are depicted separately in (b) and (c), for the sake of clarity.

Chapter 5

Conclusion

Within this work, a single linear MPC has been introduced to control a small-scale biomass furnace. Experimental closed-loop results confirm sufficient control performance within the whole power range, not only in steady-state operation but also in transient periods. Furthermore, combustion of different solid biofuels reveals that the implemented approach incorporates a pleasant method for fuel switches, done by a simple adaption of fuel-related model parameters. Additionally, the chosen controller setup preserves manufacturer's empirical knowledge, given in the form of software supplements, and keeps complexity and costs for implementation and maintenance at bay.

While direct controlling of CO must be relinquished due to its highly non-linear formation process, an adjusted version of a formation model from literature [15] pictures a promising way to determine O_2 references according to emission minimization. While simulation results clearly underpin the hypothesis of emission reduction related to an appropriate O_2 reference, experimental validation should be part of further research. Interestingly, this approach can be applied to any small biomass furnace without the need of additional sensors. This embodies a promising path to span the gap to large and cost-intensive furnaces, which may be already controlled by sophisticated strategies allowing to handle CO directly as a control variable. Besides its forward-looking nature, a model predictive algorithm also takes possible constraints into account. Experimental and especially simulated results indicate improved emission behavior by implementing a bottom limit for the O_2 concentration with respect to its contribution to the CO formation process.

While defining the output constraints in a soft sense guarantees feasibility, designing the cost function in a quadratic manner allows fast solvers to be used. Therefore, low-cost standard hardware is sufficient to conduct all necessary computations in every time step.

As the introduced controller is based on one of the simplest model predictive formulations, it is on the one hand easy to implement and to maintain, but offers on the other hand a variety of additional features compared to the widely used PID control schemes. In combination with a model of the CO formation process it provides a setup that is able to meet high efficiency as well as emission-related requirements. Therefore,

this work should act as a guideline describing how to take a first but necessary step away from classical methods to fulfill upcoming and even more restrictive limitations in the future.

To ease migration, the feedforward controller and the input interface, which were solely designed by the manufacturer, were consciously included into the overall concept on a one-to-one basis. Nonetheless, a more open access to the actual furnace hardware without any obstacles, concerning empirically developed add-ons, would be preferable in order to unfold MPC's full potential.

Besides this aspect, further research on the static CO model is worthy of consideration to possibly provide improved O_2 references. Despite its good accordance with experimental results for combustion of wooden pellets, similar models for other fuels are hardly discussed in literature. Since they would enable to successfully apply the introduced strategy for emission reduction more generally, their development is highly promising. Additionally, formation models for other emissions could be designed and included to find appropriate references for the O_2 concentration. Another way to incorporate such emissions is to include appropriate additional terms in the cost function.

Further cost contributions could not only consider emission aspects but also include the demand for high efficiency in an explicit fashion. In the future, additional constraints or cost contributions could be used to migrate safety-relevant entities into the MPC formulation, which would reduce the complexity of the overall control scheme.

Employing estimation algorithms to account for varying fuel properties or water contents, similar to those presented in [9, 35], could be another step towards increased performance. Estimation results could be either included as a disturbance variable or used to update the furnace model on a regular basis.

Up to now, the supply temperature reference was assumed to be given precisely. Especially, if a furnace is used to heat just a few or even a single facility, predicting the heat demand for the next 30 min is challenging. Therefore, intensive research on how to provide appropriate predictions is of vital importance to exploit predictive controller's full potential.

Appendix A

Fundamentals of discrete-time linear MPC

Model predictive control schemes gained increased interest in recent years. Linear discrete-time formulations combine moderate implementation effort with comprehensive additional features not provided by classical control approaches. The following remarks are based on literature [32,36] and serve as a compendium of how to implement a simple linear model predictive controller (MPC). After discussing the basic formulation with and without constraints, this chapter closes with a short recap of stability issues.

A.1 Basic concept of model predictive control

While many different model predictive control schemes exist, the basic concept always remains unaltered. Based on a process model and actual measurements, future control inputs \mathbf{u} are calculated by optimizing an appropriately chosen cost function. Figure A.1 depicts this situation for a single-input-single-output system at the actual time step k . The main objective is to determine future inputs, which can be varied within the control horizon comprising N_c time steps, in such a way to attain the best possible control performance within the prediction horizon consisting of N_p time steps.

Since the process model is utilized to predict plant outputs \mathbf{y} , modeling and parameter identification are of considerable importance. Besides deviations from reference values \mathbf{y}_{ref} , also restrictions of inputs, output constraints and so on can be included into the optimization problem, which increases applicability of such advanced control strategies even further.

Hereinafter, a linear discrete-time model predictive formulation based on state space representation of the process model is discussed in detail. Other model predictive approaches are comprehensively discussed in [32].

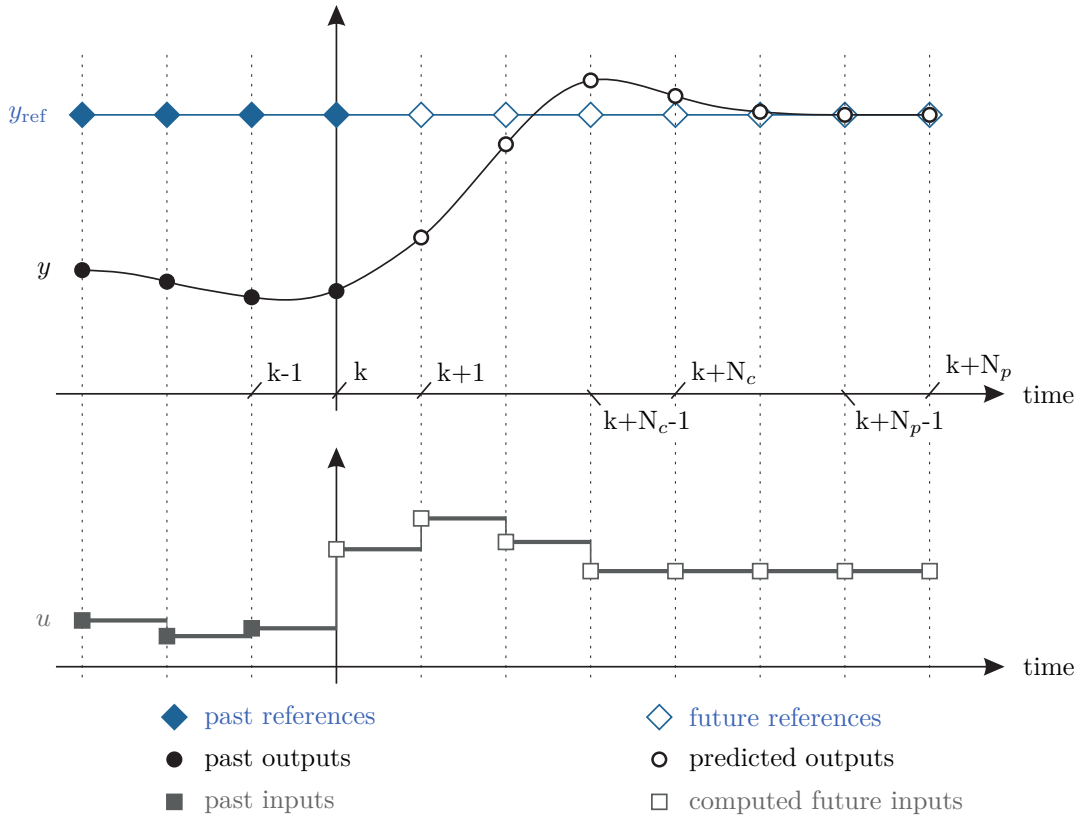


Figure A.1: Illustrative representation of a model predictive control procedure at the actual time step k . Without loss of generality, a single-input-single-output system is considered.

A.2 Linear discrete-time formulation

Suppose a linear discrete state space model of the considered plant to be given at time step k by

$$\begin{aligned}\tilde{\mathbf{x}}_m(k+1) &= \mathbf{A}_m \tilde{\mathbf{x}}_m(k) + \mathbf{B}_m \tilde{\mathbf{u}}(k) + \mathbf{E}_m \tilde{\mathbf{z}}(k) \\ \tilde{\mathbf{y}}(k) &= \mathbf{C}_m \tilde{\mathbf{x}}_m(k)\end{aligned}\tag{A.1}$$

with the state vector $\tilde{\mathbf{x}}_m \in \mathbb{R}^{n_x}$, the controllable input vector $\tilde{\mathbf{u}} \in \mathbb{R}^{n_u}$, the disturbance vector $\tilde{\mathbf{z}} \in \mathbb{R}^{n_z}$, the output vector $\tilde{\mathbf{y}} \in \mathbb{R}^{n_y}$, the system matrix $\mathbf{A}_m \in \mathbb{R}^{n_x \times n_x}$, the input matrix $\mathbf{B}_m \in \mathbb{R}^{n_x \times n_u}$, the disturbance matrix $\mathbf{E}_m \in \mathbb{R}^{n_x \times n_z}$, and the output matrix $\mathbf{C}_m \in \mathbb{R}^{n_y \times n_x}$. Since the algorithm being presented within this chapter relies on actual measurements, actual inputs and disturbances are assumed to not directly influence the outputs. To provide a general approach, which is also applicable for models gained by linearization of a non-linear description, deviations from a chosen steady-state operating point are declared by

$$(\tilde{\star}) = (\star) - (\star)_{\text{op}},\tag{A.2}$$

where (\star) is a placeholder for the considered variable.

To eliminate steady-state offsets, the plant model is augmented by adding n_y integrators. Applying the difference operation

$$\Delta(\star)(k+1) = (\tilde{\star})(k+1) - (\tilde{\star})(k) \quad (\text{A.3})$$

on Eq. (A.1) yields the incremental formulation as follows:

$$\begin{aligned} \Delta \mathbf{x}_m(k+1) &= \mathbf{A}_m \Delta \mathbf{x}_m(k) + \mathbf{B}_m \Delta \mathbf{u}(k) + \mathbf{E}_m \Delta \mathbf{z}(k) \\ \tilde{\mathbf{y}}(k+1) &= \tilde{\mathbf{y}}(k) + \mathbf{C}_m \Delta \mathbf{x}_m(k+1). \end{aligned} \quad (\text{A.4})$$

By introducing the augmented state vector \mathbf{x} according to

$$\mathbf{x}(k) = \begin{bmatrix} \Delta \mathbf{x}_m(k) \\ \tilde{\mathbf{y}}(k) \end{bmatrix}, \quad (\text{A.5})$$

the state space representation of the augmented model is given by

$$\begin{aligned} \mathbf{x}(k+1) &= \mathbf{A}\mathbf{x}(k) + \mathbf{B}\Delta \mathbf{u}(k) + \mathbf{E}\Delta \mathbf{z}(k) \\ \tilde{\mathbf{y}}(k) &= \mathbf{C}\mathbf{x}(k) \end{aligned} \quad (\text{A.6})$$

with the matrices

$$\mathbf{A} = \begin{bmatrix} \mathbf{A}_m & \mathbf{0}_{n_x \times n_y} \\ \mathbf{C}_m \mathbf{A}_m & \mathbf{I}_{n_y} \end{bmatrix}, \quad \mathbf{B} = \begin{bmatrix} \mathbf{B}_m \\ \mathbf{C}_m \mathbf{B}_m \end{bmatrix}, \quad \mathbf{E} = \begin{bmatrix} \mathbf{E}_m \\ \mathbf{C}_m \mathbf{E}_m \end{bmatrix}, \quad \mathbf{C} = \begin{bmatrix} \mathbf{0}_{n_y \times n_x} & \mathbf{I}_{n_y} \end{bmatrix}.$$

Note that - providing a general statement by using a, b as substitutes - $\mathbf{0}_{a \times b}$ denotes a zero matrix of size $(a \times b)$ and \mathbf{I}_a denotes an identity matrix of size $(a \times a)$. To provide a concise description, vector \mathbf{Y} aggregates predicted outputs within the prediction horizon as follows:

$$\mathbf{Y} = \left[\tilde{\mathbf{y}}(k+1|k)^T \quad \tilde{\mathbf{y}}(k+2|k)^T \quad \dots \quad \tilde{\mathbf{y}}(k+N_p|k)^T \right]^T. \quad (\text{A.7})$$

Thus, the prediction can be written compactly as

$$\mathbf{Y} = \mathbf{F}\mathbf{x}(k) + \Phi_u \Delta \mathbf{U} + \Phi_z \Delta \mathbf{Z}, \quad (\text{A.8})$$

where $\Delta \mathbf{U}$ denotes the vector of stacked incremental inputs and $\Delta \mathbf{Z}$ the vector of stacked incremental disturbances. Definitions of vectors and matrices being present in Eq. (A.8) are given below.

$$\Delta \mathbf{U} = \left[\Delta \mathbf{u}(k)^T \quad \Delta \mathbf{u}(k+1)^T \quad \dots \quad \Delta \mathbf{u}(k+N_c-1)^T \right]^T \quad (\text{A.9})$$

$$\Delta \mathbf{Z} = \left[\Delta \mathbf{z}(k)^T \quad \Delta \mathbf{z}(k+1)^T \quad \dots \quad \Delta \mathbf{z}(k+N_c-1)^T \right]^T \quad (\text{A.10})$$

$$\mathbf{F} = \left[(\mathbf{C}\mathbf{A}^1)^T \quad (\mathbf{C}\mathbf{A}^2)^T \quad \dots \quad (\mathbf{C}\mathbf{A}^{N_p})^T \right]^T \quad (\text{A.11})$$

$$\Phi_{\mathbf{u}} = \begin{bmatrix} \mathbf{CB} & \mathbf{0}_{n_y \times n_u} & \dots & \mathbf{0}_{n_y \times n_u} \\ \mathbf{CAB} & \mathbf{CB} & \dots & \mathbf{0}_{n_y \times n_u} \\ \mathbf{CA^2B} & \mathbf{CAB} & \dots & \mathbf{0}_{n_y \times n_u} \\ \vdots & & & \\ \mathbf{CA}^{N_p-1}\mathbf{B} & \mathbf{CA}^{N_p-2}\mathbf{B} & \dots & \mathbf{CA}^{N_p-N_c}\mathbf{B} \end{bmatrix} \quad (\text{A.12})$$

$$\Phi_{\mathbf{z}} = \begin{bmatrix} \mathbf{CE} & \mathbf{0}_{n_y \times n_z} & \dots & \mathbf{0}_{n_y \times n_z} \\ \mathbf{CAE} & \mathbf{CE} & \dots & \mathbf{0}_{n_y \times n_z} \\ \mathbf{CA^2E} & \mathbf{CAE} & \dots & \mathbf{0}_{n_y \times n_z} \\ \vdots & & & \\ \mathbf{CA}^{N_p-1}\mathbf{E} & \mathbf{CA}^{N_p-2}\mathbf{E} & \dots & \mathbf{CA}^{N_p-N_c}\mathbf{E} \end{bmatrix} \quad (\text{A.13})$$

Based upon that, a reasonable and still simple cost function J for optimization may be formulated according to

$$J = \Delta \mathbf{U}^T \mathbf{R}_{\mathbf{u}} \Delta \mathbf{U} + (\mathbf{Y}_{\text{ref}} - \mathbf{Y})^T \mathbf{Q}_{\mathbf{y}} (\mathbf{Y}_{\text{ref}} - \mathbf{Y}) + J_{\text{sc}}. \quad (\text{A.14})$$

While the first term penalizes harsh changes of the controllable input, the second term accounts for deviations of the predicted outputs \mathbf{Y} from a given reference \mathbf{Y}_{ref} , which is defined as

$$\mathbf{Y}_{\text{ref}} = [\tilde{\mathbf{y}}_{\text{ref}}(k+1)^T \tilde{\mathbf{y}}_{\text{ref}}(k+2)^T \dots \tilde{\mathbf{y}}_{\text{ref}}(k+N_p)^T]^T. \quad (\text{A.15})$$

Furthermore, the cost contribution J_{sc} accounts for potential soft constraints, see section A.3.3. The weighting matrices $\mathbf{R}_{\mathbf{u}}$, representing costs for increasing control inputs, and $\mathbf{Q}_{\mathbf{y}}$, penalizing control errors, are structured as

$$\mathbf{R}_{\mathbf{u}} = \text{diag}(\underbrace{[\mathbf{r}_{\mathbf{u}} \ \mathbf{r}_{\mathbf{u}} \ \dots \ \mathbf{r}_{\mathbf{u}}]}_{N_c \text{ times}}), \quad \mathbf{Q}_{\mathbf{y}} = \text{diag}(\underbrace{[\mathbf{q}_{\mathbf{y}} \ \mathbf{q}_{\mathbf{y}} \ \dots \ \mathbf{q}_{\mathbf{y}}]}_{N_p \text{ times}}), \quad (\text{A.16})$$

where

$$\mathbf{r}_{\mathbf{u}} = \text{diag}([r_1 \ r_2 \ \dots \ r_{n_u}]), \quad \mathbf{q}_{\mathbf{y}} = \text{diag}([q_1 \ q_2 \ \dots \ q_{n_y}]) \quad (\text{A.17})$$

comprise the scalar weighting factors for each input and output, respectively. Minimizing the cost function (Eq. A.14) without considering any constraints (and therefore also $J_{\text{sc}} = 0$) yields the optimal control sequence $\Delta \mathbf{U}^*$ according to

$$\Delta \mathbf{U}^* = \left(\Phi_{\mathbf{u}}^T \mathbf{Q}_{\mathbf{y}} \Phi_{\mathbf{u}} + \mathbf{R}_{\mathbf{u}} \right)^{-1} \Phi_{\mathbf{u}}^T \mathbf{Q}_{\mathbf{y}} (\mathbf{Y}_{\text{ref}} - \mathbf{F}\mathbf{x}(k) - \Phi_{\mathbf{z}} \Delta \mathbf{Z}). \quad (\text{A.18})$$

Note that the presented formulation enables to account for disturbances influencing plant behavior. Since most practical applications lack of appropriate knowledge concerning acting disturbances, $\Delta \mathbf{Z} = \mathbf{0}$ holds in such cases.

A.3 Consideration of constraints

A major benefit of model predictive control schemes is the ability to explicitly account for present limitations for the controllable inputs as well as output and state values. Thereby, the overall optimization problem incorporates these restrictions by narrowing the solution space according to appropriate inequality constraints. Besides the formulation of two different types of input constraints (sections A.3.1 and A.3.2), output constraints and the related soft implementation (section A.3.3) are discussed in the following. Section A.3.4 then summarizes the conclusive optimization problem including presented limitations.

A.3.1 Rate constraints on input

Some applications rise the need to restrict the rate of change of the controllable inputs by introducing lower and upper limits defined by

$$\Delta \mathbf{u}_{\{\min, \max\}} = \begin{bmatrix} \Delta u_{1, \{\min, \max\}} \\ \Delta u_{2, \{\min, \max\}} \\ \vdots \\ \Delta u_{n_u, \{\min, \max\}} \end{bmatrix}. \quad (\text{A.19})$$

As these constraints should apply for the whole control horizon, the decisive condition is given as

$$\Delta \mathbf{U}_{\min} \leq \Delta \mathbf{U} \leq \Delta \mathbf{U}_{\max} \quad (\text{A.20})$$

with limitations according to

$$\Delta \mathbf{U}_{\{\min, \max\}} = \underbrace{\begin{bmatrix} \mathbf{I}_{n_u} \\ \mathbf{I}_{n_u} \\ \vdots \\ \mathbf{I}_{n_u} \end{bmatrix}}_{\mathbf{T}_{u,1}} \Delta \mathbf{u}_{\{\min, \max\}}. \quad (\text{A.21})$$

To provide a formulation that is consistent with the optimization problem, Eq. (A.20) is rewritten in terms of the decision variable $\Delta \mathbf{U}$ as follows:

$$\begin{bmatrix} -\mathbf{I}_{N_c n_u} \\ \mathbf{I}_{N_c n_u} \end{bmatrix} \Delta \mathbf{U} \leq \begin{bmatrix} -\mathbf{T}_{u,1} \Delta \mathbf{u}_{\min} \\ \mathbf{T}_{u,1} \Delta \mathbf{u}_{\max} \end{bmatrix}. \quad (\text{A.22})$$

A.3.2 Amplitude constraints on input

Since the most common type of restrictions acts on the amplitude of the controllable inputs, this section is of considerable importance for almost every design procedure. As the actual algorithm requires thresholds to be set relative to the operating point

chosen for modeling (see Eq. A.1), the implemented limits $\tilde{\mathbf{u}}_{\{\min, \max\}}$ (Eq. A.23) must be determined with respect to the absolute limit values of \mathbf{u} .

$$\tilde{\mathbf{u}}_{\{\min, \max\}} = \begin{bmatrix} \tilde{u}_{1, \{\min, \max\}} \\ \tilde{u}_{2, \{\min, \max\}} \\ \vdots \\ \tilde{u}_{n_u, \{\min, \max\}} \end{bmatrix} \quad (\text{A.23})$$

Based on the vector of stacked incremental inputs $\Delta\mathbf{U}$, the vector of stacked inputs $\tilde{\mathbf{U}}$ within the control horizon is calculated by

$$\tilde{\mathbf{U}} = \begin{bmatrix} \tilde{\mathbf{u}}(k) \\ \tilde{\mathbf{u}}(k+1) \\ \vdots \\ \tilde{\mathbf{u}}(k+N_c-1) \end{bmatrix} = \mathbf{T}_{u,1} \tilde{\mathbf{u}}(k-1) + \mathbf{T}_{u,2} \Delta\mathbf{U}, \quad (\text{A.24})$$

where $\tilde{\mathbf{u}}(k-1)$ is the value of the controllable input at the previous time step and matrix $\mathbf{T}_{u,2}$ is defined as follows:

$$\mathbf{T}_{u,2} = \begin{bmatrix} \mathbf{I}_{n_u} & \mathbf{0}_{n_u \times n_u} & \cdots & \mathbf{0}_{n_u \times n_u} \\ \mathbf{I}_{n_u} & \mathbf{I}_{n_u} & \cdots & \mathbf{0}_{n_u \times n_u} \\ \vdots & & & \\ \mathbf{I}_{n_u} & \mathbf{I}_{n_u} & \cdots & \mathbf{I}_{n_u} \end{bmatrix}. \quad (\text{A.25})$$

With the permissible range according to

$$\mathbf{T}_{u,1} \tilde{\mathbf{u}}_{\min} \leq \tilde{\mathbf{U}} \leq \mathbf{T}_{u,1} \tilde{\mathbf{u}}_{\max}, \quad (\text{A.26})$$

the compact constraint formulation of absolute limits on the input values follows to

$$\begin{bmatrix} -\mathbf{T}_{u,2} \\ \mathbf{T}_{u,2} \end{bmatrix} \Delta\mathbf{U} \leq \begin{bmatrix} -\mathbf{T}_{u,1} [\tilde{\mathbf{u}}_{\min} - \tilde{\mathbf{u}}(k-1)] \\ \mathbf{T}_{u,1} [\tilde{\mathbf{u}}_{\max} - \tilde{\mathbf{u}}(k-1)] \end{bmatrix}. \quad (\text{A.27})$$

A.3.3 Output constraints

Besides input constraints, defining limits for output or state values might be interesting as well. This could render additional control loops unnecessary and therefore reduce overall complexity. However, output constraints similar to above discussed input constraints could result in an infeasible optimization problem. To overcome this lack, threshold values $\tilde{\mathbf{y}}_{\{\min, \max\}}$, according to

$$\tilde{\mathbf{y}}_{\{\min, \max\}} = \begin{bmatrix} \tilde{y}_{1, \{\min, \max\}} \\ \tilde{y}_{2, \{\min, \max\}} \\ \vdots \\ \tilde{y}_{n_y, \{\min, \max\}} \end{bmatrix}, \quad (\text{A.28})$$

will no longer be considered as hard but rather soft limits. To be more precise, the permissible range is now defined as

$$\mathbf{T}_y \tilde{\mathbf{y}}_{\min} - \mathbf{T}_y \mathbf{s} \leq \mathbf{Y} \leq \mathbf{T}_y \tilde{\mathbf{y}}_{\max} + \mathbf{T}_y \mathbf{s} \quad (\text{A.29})$$

with the matrix \mathbf{T}_y given by

$$\mathbf{T}_y = \begin{bmatrix} \mathbf{I}_{n_y} \\ \mathbf{I}_{n_y} \\ \vdots \\ \mathbf{I}_{n_y} \end{bmatrix} \quad (\text{A.30})$$

and $\mathbf{s} > \mathbf{0}$ as the so-called vector of slack variables, which is defined as

$$\mathbf{s} = \begin{bmatrix} s_1 & s_2 & \dots & s_{n_y} \end{bmatrix}^T. \quad (\text{A.31})$$

These slack variables allow the lower and upper limits to be shifted, and determination of their actual values has thereby to be integrated into the optimization problem. By introducing additional costs J_{sc} of the form

$$J_{sc} = \mathbf{C}_1 \mathbf{s} + \mathbf{s}^T \mathbf{C}_q \mathbf{s}, \quad (\text{A.32})$$

the strength of the implemented limits can be adapted by appropriately selected weighting factors $w \in \mathbb{R}^{0+}$ comprised in matrices \mathbf{C}_1 and \mathbf{C}_q according to

$$\mathbf{C}_1 = \begin{bmatrix} w_{1,1} & w_{1,2} & \dots & w_{1,n_y} \end{bmatrix}, \quad (\text{A.33})$$

$$\mathbf{C}_q = \text{diag} \begin{bmatrix} w_{q,1} & w_{q,2} & \dots & w_{q,n_y} \end{bmatrix}, \quad (\text{A.34})$$

respectively. Note that the presented cost contribution J_{sc} (Eq. A.32) stems from the demand to maintain the quadratic form already applied in Eq. (A.14). While another cost function might fulfill the actual control demand more appropriately, a more complex solver would be needed. Since this usually comes along with increased computation time, such an adaption should be justified by simulation or experiment. Finally, the output constraints can be rewritten as

$$\begin{bmatrix} -\Phi_u & -\mathbf{T}_y \\ \Phi_u & -\mathbf{T}_y \\ \mathbf{0}_{n_y \times N_p n_u} & -\mathbf{I}_{n_y} \end{bmatrix} \begin{bmatrix} \Delta U \\ \mathbf{s} \end{bmatrix} \leq \begin{bmatrix} -\mathbf{T}_y \tilde{\mathbf{y}}_{\min} + \mathbf{F} \mathbf{x}(k) + \Phi_z \Delta \mathbf{Z} \\ \mathbf{T}_y \tilde{\mathbf{y}}_{\max} - \mathbf{F} \mathbf{x}(k) - \Phi_z \Delta \mathbf{Z} \\ \mathbf{0}_{n_y \times 1} \end{bmatrix}. \quad (\text{A.35})$$

A.3.4 Conclusive optimization problem

Considering \mathbf{s} as an additional decision variable and neglecting immutable terms in Eq. (A.14) yield the overall quadratic cost function J in case of active soft constraints as

$$J = \begin{bmatrix} \Delta U \\ \mathbf{s} \end{bmatrix}^T \mathbf{H} \begin{bmatrix} \Delta U \\ \mathbf{s} \end{bmatrix} + \mathbf{f}^T \begin{bmatrix} \Delta U \\ \mathbf{s} \end{bmatrix} \quad (\text{A.36})$$

with the matrices

$$\mathbf{H} = \begin{bmatrix} \mathbf{R}_u + \Phi_u^T \mathbf{Q}_y \Phi_u & \mathbf{0}_{N_c n_u \times n_y} \\ \mathbf{0}_{n_y \times N_c n_u} & \mathbf{C}_q \end{bmatrix}, \quad (\text{A.37})$$

$$\mathbf{f}^T = \begin{bmatrix} -2(\mathbf{Y}_{\text{ref}} - \mathbf{F}\mathbf{x}(k) - \Phi_z \Delta \mathbf{Z}) \mathbf{Q}_y \Phi_u, & \mathbf{C}_1 \end{bmatrix}. \quad (\text{A.38})$$

Equation (A.36) obeys the above introduced constraints, which are rewritten as combined inequalities and jointly expressed as

$$\begin{bmatrix} -\mathbf{I}_{N_c n_u} & \mathbf{0}_{N_c n_u \times n_y} \\ \mathbf{I}_{N_c n_u} & \mathbf{0}_{N_c n_u \times n_y} \\ -\mathbf{T}_{u,2} & \mathbf{0}_{N_c n_u \times n_y} \\ \mathbf{T}_{u,2} & \mathbf{0}_{N_c n_u \times n_y} \\ -\Phi_u & -\mathbf{T}_y \\ \Phi_u & -\mathbf{T}_y \\ \mathbf{0}_{n_y \times N_c n_u} & -\mathbf{I}_{n_y} \end{bmatrix} \begin{bmatrix} \Delta \mathbf{U} \\ \mathbf{s} \end{bmatrix} \leq \begin{bmatrix} -\mathbf{T}_{u,1} \Delta \mathbf{u}_{\min} \\ \mathbf{T}_{u,1} \Delta \mathbf{u}_{\max} \\ -\mathbf{T}_{u,1} [\tilde{\mathbf{u}}_{\min} - \tilde{\mathbf{u}}(k-1)] \\ \mathbf{T}_{u,1} [\tilde{\mathbf{u}}_{\max} - \tilde{\mathbf{u}}(k-1)] \\ -\mathbf{T}_y \tilde{\mathbf{y}}_{\min} + \mathbf{F}\mathbf{x}(k) + \Phi_z \Delta \mathbf{Z} \\ \mathbf{T}_y \tilde{\mathbf{y}}_{\max} - \mathbf{F}\mathbf{x}(k) - \Phi_z \Delta \mathbf{Z} \\ \mathbf{0}_{n_y \times 1} \end{bmatrix}. \quad (\text{A.39})$$

Therefore, the conclusive quadratic programming problem consists of Eqs. (A.36) and (A.39).

A.4 Receding horizon principle

Optimization yields $\Delta \mathbf{U}^*$ as the solution given by Eq. (A.18) or found by solving the quadratic programming problem considering inequality constraints. By applying the receding horizon principle, the controllable input vector $\tilde{\mathbf{u}}$ at the actual time step k is calculated by

$$\begin{aligned} \tilde{\mathbf{u}}(k) &= \tilde{\mathbf{u}}(k-1) + \Delta \mathbf{u}(k) \\ &= \tilde{\mathbf{u}}(k-1) + [\mathbf{I}_{n_u} \quad \mathbf{0}_{n_u \times n_u} \quad \dots \quad \mathbf{0}_{n_u \times n_u}] \Delta \mathbf{U}^*. \end{aligned} \quad (\text{A.40})$$

A.5 Stability

Stability is a major concern in all control applications and so it is for model predictive schemes as well. In the following, three different approaches being able to guarantee stability of a discrete-time MPC with constraints are discussed briefly. While Fig. A.2 depicts these methods schematically, the interested reader is referred to a comprehensive review published in [37] or to a more illustrative recap presented in [36].

Hereinafter, it is assumed that the plant model perfectly fits reality and no disturbances occur ($\tilde{\mathbf{z}} = \mathbf{0}$). Furthermore, an equilibrium point characterized by $\tilde{\mathbf{x}} = 0$ and $\tilde{\mathbf{u}} = 0$ should exist and has to be stabilized.

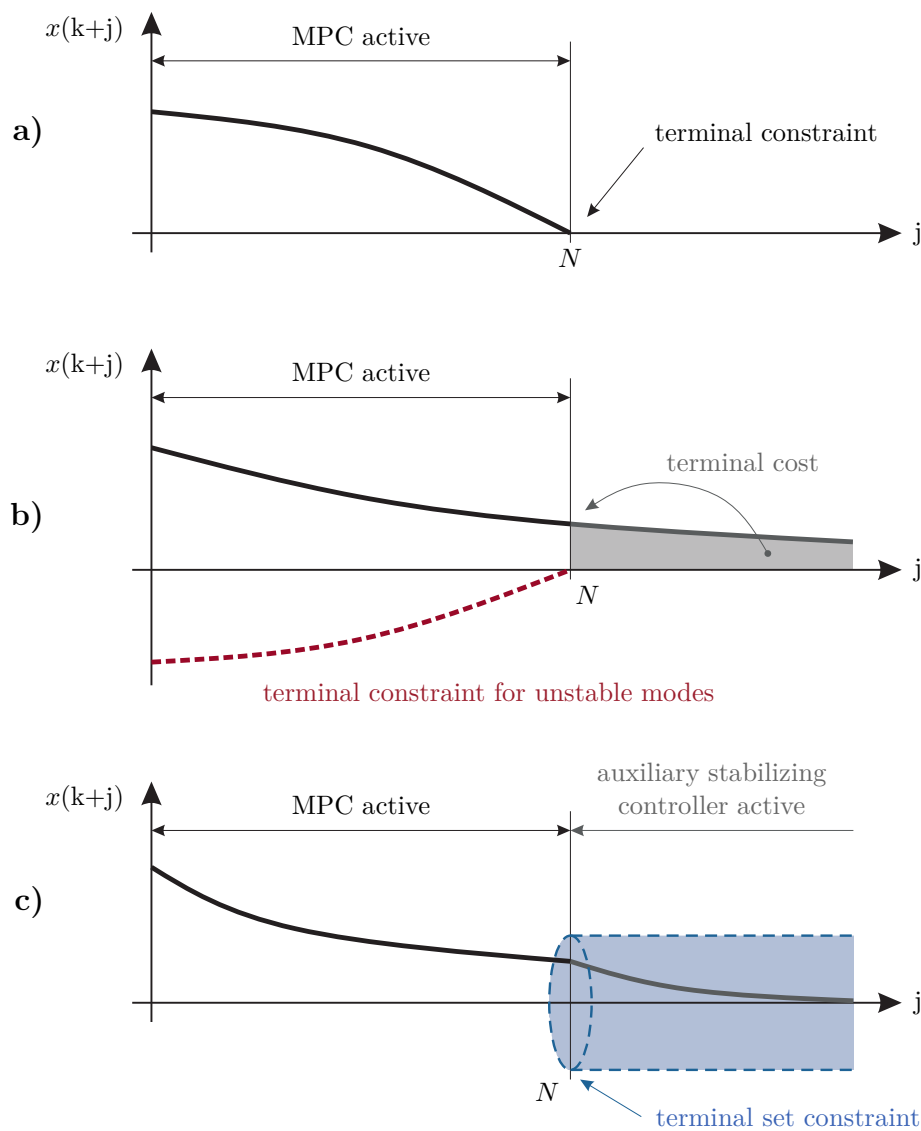


Figure A.2: Schematic representation of different approaches to guarantee MPC closed-loop stability: (a) terminal equality constraints, (b) terminal costs (and terminal equality constraints for unstable modes), (c) terminal set constraints. Illustration adapted from [36].

A.5.1 Terminal equality constraints

Among all presented approaches, introducing terminal equality constraints is the simplest one. The initial optimization problem is thereby extended by the additional equality constraint

$$\tilde{\mathbf{x}}(k+N_p|k) = \mathbf{0} \quad (\text{A.41})$$

effective at the end of the prediction horizon, see Fig. A.2a. If the overall optimization problem is feasible and provides a global minimum in each time step, closed loop stability is guaranteed. The proof related thereto can be simply shown by utilizing an

appropriate Lyapunov function [36]. However, restriction (A.41) might entail infeasibility damping applicability of this simple approach.

A.5.2 Terminal costs

Infinite-horizon optimal control problems yield closed-loop stability if the considered plant is detectable and can be stabilized in the given configuration. The very same basic idea is now applied to guarantee stability in case of a model predictive control algorithm, which results in a cost function $J_{tc,s}$ based on an infinite horizon and given by

$$J_{tc,s}(k) = \sum_{i=1}^{\infty} \left\{ \tilde{\mathbf{y}}(k+i|k)^T \mathbf{q}_y \tilde{\mathbf{y}}(k+i|k) + \Delta \tilde{\mathbf{u}}(k+i-1)^T \mathbf{r}_u \Delta \tilde{\mathbf{u}}(k+i-1) \right\}. \quad (\text{A.42})$$

Since changes of the control action can only take place within the control horizon, $\Delta \tilde{\mathbf{u}}(k+i-1) = \mathbf{0}$ holds for $i > N_c$. Thus, the cost function can be rewritten as

$$J_{tc,s}(k) = \sum_{i=1}^{N_c} \left\{ \tilde{\mathbf{y}}(k+i|k)^T \mathbf{q}_y \tilde{\mathbf{y}}(k+i|k) + \Delta \tilde{\mathbf{u}}(k+i-1)^T \mathbf{r}_u \Delta \tilde{\mathbf{u}}(k+i-1) \right\} + \dots \quad (\text{A.43})$$

$$\tilde{\mathbf{x}}(k+N_c|k)^T \mathbf{Q} \tilde{\mathbf{x}}(k+N_c|k)$$

with \mathbf{Q} as a solution of the discrete Lyapunov equation given by

$$\mathbf{A}_m^T \mathbf{Q} \mathbf{A}_m = \mathbf{Q} - \mathbf{C}_m^T \mathbf{q}_y \mathbf{C}_m. \quad (\text{A.44})$$

Therefore, the last term of Eq. (A.43) represents an additional cost contribution penalizing states at the end of the control horizon, see Fig. A.2b. If \mathbf{A}_m only exhibits eigenvalues inside the unit circle, which is valid for asymptotically stable plants, Eq. (A.44) provides a unique positive definite solution \mathbf{Q} . As $\tilde{\mathbf{x}}(k+N_c|k)^T \mathbf{Q} \tilde{\mathbf{x}}(k+N_c|k)$ is thereby a Lyapunov function, stability in the sense of Lyapunov is guaranteed. It can be shown, that under the assumption of $\mathbf{R} \succ 0$, $\mathbf{Q} \succ 0$ and present full state observability, the relation

$$J_{tc,s}(k+1) = J_{tc,s}(k) - \underbrace{\tilde{\mathbf{y}}(k+1|k)^T \mathbf{q}_y \tilde{\mathbf{y}}(k+1|k)}_{\geq 0} - \underbrace{\Delta \tilde{\mathbf{u}}(k)^T \mathbf{r}_u \Delta \tilde{\mathbf{u}}(k)}_{\geq 0} \leq J_{tc,s}(k) \quad (\text{A.45})$$

implies that $\|\tilde{\mathbf{x}}\|_2$ decreases over time. Consequently, there is no need to include terminal costs if a stable plant is considered.

In case of unstable modes, they have to be separated by an eigenvalue/eigenvector decomposition as follows

$$\mathbf{A}_m \mathbf{S} = \mathbf{S} \mathbf{\Lambda} \quad (\text{A.46})$$

with \mathbf{S} as the matrix of eigenvectors arranged column-by-column and $\mathbf{\Lambda}$ as a diagonal matrix filled with the related eigenvalues. Based on the actual eigenvalue, \mathbf{S} can be split into unstable modes \mathbf{S}_u and stable modes \mathbf{S}_s according to

$$\mathbf{S} = \begin{bmatrix} \mathbf{S}_u & \mathbf{S}_s \end{bmatrix}. \quad (\text{A.47})$$

The unstable modes can be observed by the modal coordinates ξ_u given as

$$\xi_u(k) = C_u \tilde{x}(k) \quad (\text{A.48})$$

with matrix C_u found by

$$C_u \begin{bmatrix} S_u & S_s \end{bmatrix} = \begin{bmatrix} I & 0 \end{bmatrix}. \quad (\text{A.49})$$

To guarantee stability, modal coordinates ξ_u are forced to zero at the end of the control horizon, see Fig. A.2b. Thus, the terminal equality constraint related thereto is given by

$$\xi_u(k+N_c) = F_u \tilde{x}(k) + \Phi_{u,u} \Delta U \stackrel{!}{=} 0, \quad (\text{A.50})$$

with the matrices

$$F_u = C_u A_m^{N_c}, \quad \Phi_{u,u} = \begin{bmatrix} C_u A_m^{N_c-1} B & C_u A_m^{N_c-2} B & \dots & C_u B \end{bmatrix}. \quad (\text{A.51})$$

Although the last part of this approach is similar to the terminal equality constraints presented in section A.5.1, this overall concept softens conditions to guarantee stability since stable motions are not forced to vanish at the end of the control horizon any more.

A.5.3 Terminal set constraints

Since both methods mentioned above utilize some kind of terminal equality constraint, feasibility is not guaranteed. The following approach generalizes the underlying problem by assuming an auxiliary stabilizing controller to be active after the MPC horizon ends. Therefore, the cost function can be written more generally as follows

$$J_{\text{tsc}}(k) = \sum_{i=1}^{N_c} \underbrace{l(\tilde{x}(k+i), \tilde{u}(k+i-1))}_{\text{stage costs}} + \underbrace{V_f(\tilde{x}(k+N_c))}_{\text{terminal costs}}, \quad (\text{A.52})$$

where the terminal costs relate to the stabilizing control algorithm. To guarantee stability, this fictitious controller must not run into constraints. For this purpose, one has to determine a region - the so-called terminal set - \mathbb{X}_f in which the MPC has to drive the system at the end of the horizon, see Fig. A.2c. If the states $\tilde{x}(k+N_c)$ are located within this region, the auxiliary controller is thereafter able to stabilize the system for all time without violating constraints. With \mathbb{X} and \mathbb{U} as the permissible ranges for the state and input vector, respectively, the constraints for the overall optimization problem can be written as

$$\tilde{x}(k+i) \in \mathbb{X} \subset \mathbb{R}^{n_x} \quad \forall i = 0, 1, \dots \quad (\text{A.53})$$

$$\tilde{u}(k+i) \in \mathbb{U} \subset \mathbb{R}^{n_u} \quad \forall i = 0, 1, \dots \quad (\text{A.54})$$

$$\tilde{x}(k+N_c) \in \mathbb{X}_f \subseteq \mathbb{X}. \quad (\text{A.55})$$

For a comprehensive review of how to determine such a terminal set, see [37].

Appendix B

Fundamentals of Kalman-filtering

State estimation is of particular interest in many technical fields and evolved drastically since 1960, when Rudolph E. Kalman published his famous article [38]. Based on least squares estimation, introduced by Carl F. Gauss in 1809 [39], Kalman established an estimation algorithm by minimizing error variance. Not only its simple discrete-time implementation but also the fact that this approach provides the optimal (linear) filter for most applications stands out. Because of its paramount importance, only the discrete-time formulation is discussed in detail in this chapter. Out of numerous literature sources referring to this topic, the following remarks are mainly based on [40, 41].

B.1 Process description

Assume a discrete state space model of the investigated plant to be given by

$$\mathbf{x}(k) = \mathbf{A}_d \mathbf{x}(k-1) + \mathbf{B}_d \mathbf{u}(k-1) + \mathbf{G}_d \mathbf{w}(k-1) \quad (\text{B.1})$$

$$\mathbf{y}(k) = \mathbf{C}_d \mathbf{x}(k) + \mathbf{D}_d \mathbf{u}(k) + \mathbf{v}(k), \quad (\text{B.2})$$

with the state vector \mathbf{x} comprising n_x states, the output vector \mathbf{y} consisting of n_y measurable quantities, the input vector \mathbf{u} with n_u elements, the vector of process noise \mathbf{w} of size n_w , the vector of measurement noise \mathbf{v} with n_y items, the system matrix \mathbf{A}_d , the input matrix \mathbf{B}_d , the input matrix for process noise \mathbf{G}_d , the output matrix \mathbf{C}_d , and the direct input-output matrix \mathbf{D}_d . Please note that matrices are of appropriate size according to vector sizes mentioned above.

While the measurement noise \mathbf{v} represents actually occurring fluctuations of the measured values, process noise \mathbf{w} is an abstract entity accounting for model uncertainties. A model that perfectly matches the real plant would be sufficiently described without additional process noise. Furthermore, there would be no need to estimate but rather to just predict model states by using the perfect model. But since no model is able to exhaustively fit reality, process noise is vital to consider limited confidence in the chosen model. It is assumed that the noise processes are white, Gaussian dis-

tributed, zero-mean and have known covariance matrices - see mathematical formulation as follows.

$$\mathbf{w}(k) \sim \mathcal{N}(\mathbf{0}, \mathbf{Q}(k)) \quad (\text{B.3})$$

$$\mathbf{Q}(k) = \text{diag} [Q_1(k) \dots Q_{n_x}(k)] \quad (\text{B.4})$$

$$\mathbf{v}(k) \sim \mathcal{N}(\mathbf{0}, \mathbf{R}(k)) \quad (\text{B.5})$$

$$\mathbf{R}(k) = \text{diag} [R_1(k) \dots R_{n_y}(k)] \quad (\text{B.6})$$

Furthermore, no correlation between the noise processes should exist, whereby

$$\text{Cov} [\mathbf{v}(k), \mathbf{w}(k)] = \mathbf{0} \quad (\text{B.7})$$

holds. As \mathbf{w} has to be mean-free, any disturbances with a non-zero mean must be included in the input vector \mathbf{u} (if known) or have to be incorporated in the state vector \mathbf{x} as an additional unknown quantity.

While Eqs. (B.8-B.10) reveal that including \mathbf{G}_d in Eq. (B.1) in an explicit manner is not necessary, it is helpful for understanding stability issues (see section B.5). Furthermore, the extended Kalman filter makes use of this formulation, even for the measurement noise \mathbf{v} (section B.6).

$$\text{E} [\mathbf{G}_d \mathbf{w}(k-1)] = \mathbf{0} \quad (\text{B.8})$$

$$\text{Var} [\mathbf{G}_d \mathbf{w}(k-1)] = \mathbf{G}_d \mathbf{Q}(k-1) \mathbf{G}_d^T \quad (\text{B.9})$$

$$\mathbf{G}_d \mathbf{w}(k-1) \sim \mathcal{N}(\mathbf{0}, \mathbf{G}_d \mathbf{Q}(k-1) \mathbf{G}_d^T) \quad (\text{B.10})$$

B.2 Filter formulation

Based on the model (Eqs. B.1 and B.2), a first step towards an appropriate state estimation provides prediction of model states $\hat{\mathbf{x}}_{\text{pred}}$ and outputs $\hat{\mathbf{y}}_{\text{pred}}$ for the actual time step k as follows

$$\hat{\mathbf{x}}_{\text{pred}}(k) = \mathbf{A}_d \hat{\mathbf{x}}_{\text{corr}}(k-1) + \mathbf{B}_d \mathbf{u}(k-1) \quad (\text{B.11})$$

$$\hat{\mathbf{y}}_{\text{pred}}(k) = \mathbf{C}_d \hat{\mathbf{x}}_{\text{pred}}(k) + \mathbf{D}_d \mathbf{u}(k). \quad (\text{B.12})$$

Suppose that the corrected state estimate $\hat{\mathbf{x}}_{\text{corr}}(k-1)$ is already known from a previous calculation step. To improve estimation results, deviations $\Delta \mathbf{y}$ between the measured values \mathbf{y} and the predicted values $\hat{\mathbf{y}}_{\text{pred}}$, according to

$$\Delta \mathbf{y}(k) = \mathbf{y}(k) - \hat{\mathbf{y}}_{\text{pred}}(k), \quad (\text{B.13})$$

should be taken into account. Therefore, the predicted states $\hat{\mathbf{x}}_{\text{pred}}$ are adapted in the form of

$$\hat{\mathbf{x}}_{\text{corr}}(k) = \hat{\mathbf{x}}_{\text{pred}}(k) + \mathbf{K}(k) \Delta \mathbf{y}(k), \quad (\text{B.14})$$

where $\hat{\mathbf{x}}_{\text{corr}}(k)$ is the corrected state estimate at the actual time step and $\mathbf{K}(k)$ is a time-variant gain matrix yet to be defined. Figure B.1 represents these relations graphically.

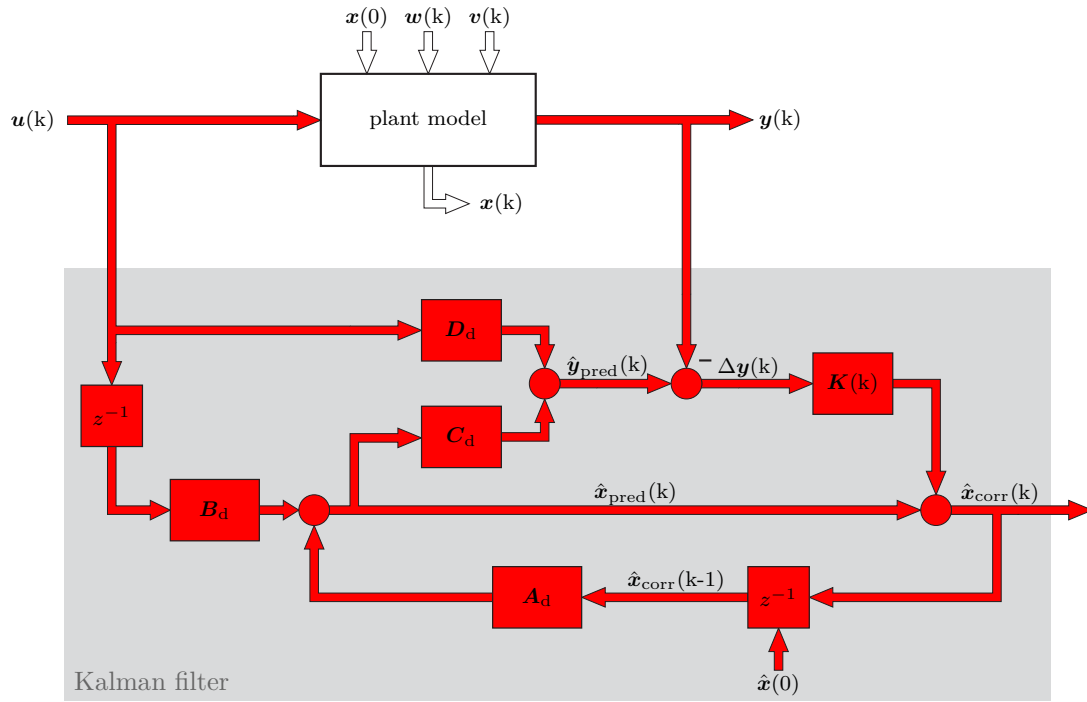


Figure B.1: Conceptual architecture of the discrete-time Kalman filter estimating states at the actual time step k .

B.3 Derivation

Although the filter formulation is now given, the question remains how to appropriately choose $\mathbf{K}(k)$ or rather which cost function has to be minimized in order to obtain an optimal estimate. For this purpose, the estimation error of prediction $\hat{\mathbf{e}}_{\text{pred}}$ and correction $\hat{\mathbf{e}}_{\text{corr}}$ are examined in detail. Coming from the following definitions

$$\hat{\mathbf{e}}_{\text{pred}}(k) := \mathbf{x}(k) - \hat{\mathbf{x}}_{\text{pred}}(k) \quad (\text{B.15})$$

$$\hat{\mathbf{e}}_{\text{corr}}(k) := \mathbf{x}(k) - \hat{\mathbf{x}}_{\text{corr}}(k) \quad (\text{B.16})$$

and using model and filter relations, the estimation errors can be written as stated by Eqs. (B.17) and (B.18), respectively.

$$\begin{aligned} \hat{\mathbf{e}}_{\text{pred}}(k) &= \mathbf{A}_d \mathbf{x}(k-1) + \mathbf{B}_d \mathbf{u}(k-1) + \mathbf{G}_d \mathbf{w}(k-1) - \mathbf{A}_d \hat{\mathbf{x}}_{\text{corr}}(k-1) - \mathbf{B}_d \mathbf{u}(k-1) \\ &= \mathbf{A}_d [\mathbf{x}(k-1) - \hat{\mathbf{x}}_{\text{corr}}(k-1)] + \mathbf{G}_d \mathbf{w}(k-1) \\ &= \mathbf{A}_d \hat{\mathbf{e}}_{\text{corr}}(k-1) + \mathbf{G}_d \mathbf{w}(k-1) \end{aligned} \quad (\text{B.17})$$

$$\begin{aligned} \hat{\mathbf{e}}_{\text{corr}}(k) &= \mathbf{x}(k) - \hat{\mathbf{x}}_{\text{pred}}(k) - \mathbf{K}(k) [\mathbf{y}(k) - \hat{\mathbf{y}}_{\text{pred}}(k)] \\ &= \mathbf{x}(k) - \hat{\mathbf{x}}_{\text{pred}}(k) - \mathbf{K}(k) [\mathbf{C}_d \mathbf{x}(k) + \mathbf{D}_d \mathbf{u}(k) + \mathbf{v}(k) - \mathbf{C}_d \hat{\mathbf{x}}_{\text{pred}}(k) - \mathbf{D}_d \mathbf{u}(k)] \\ &= [\mathbf{I} - \mathbf{K}(k) \mathbf{C}_d] [\mathbf{x}(k) - \hat{\mathbf{x}}_{\text{pred}}(k)] - \mathbf{K}(k) \mathbf{v}(k) \\ &= [\mathbf{I} - \mathbf{K}(k) \mathbf{C}_d] \hat{\mathbf{e}}_{\text{pred}}(k) - \mathbf{K}(k) \mathbf{v}(k) \end{aligned} \quad (\text{B.18})$$

By substituting $\hat{\boldsymbol{\epsilon}}_{\text{pred}}$ in Eq. (B.18), the estimation error of prediction can be calculated recursively as follows.

$$\hat{\boldsymbol{\epsilon}}_{\text{corr}}(\mathbf{k}) = [\mathbf{I} - \mathbf{K}(\mathbf{k}) \mathbf{C}_d] \mathbf{A}_d \hat{\boldsymbol{\epsilon}}_{\text{corr}}(\mathbf{k}-1) + [\mathbf{I} - \mathbf{K}(\mathbf{k}) \mathbf{C}_d] \mathbf{G}_d \mathbf{w}(\mathbf{k}-1) - \mathbf{K}(\mathbf{k}) \mathbf{v}(\mathbf{k}) \quad (\text{B.19})$$

Since the expected values of \mathbf{w} and \mathbf{v} are both zero, the dynamic of the expected estimation error is completely determined by the homogeneous part (Eq. B.20) only.

$$\mathbb{E}[\hat{\boldsymbol{\epsilon}}_{\text{corr}}(\mathbf{k})] = [\mathbf{I} - \mathbf{K}(\mathbf{k}) \mathbf{C}_d] \mathbf{A}_d \mathbb{E}[\hat{\boldsymbol{\epsilon}}_{\text{corr}}(\mathbf{k}-1)] \quad (\text{B.20})$$

Therefore, two conditions could guarantee an (asymptotically) unbiased estimation. If the initial estimate $\hat{\mathbf{x}}(0)$ is identical to the true initial state vector $\mathbf{x}(0)$, expected estimation error will be zero for all time. While this condition is never met in any practical application, an asymptotically stable error dynamic ensures asymptotically unbiased estimation anyway. Section B.5 presents a prerequisite that is necessary to guarantee this behavior in case of a time-variant matrix $\mathbf{K}(\mathbf{k})$ chosen according to Kalman's algorithm. For now, assume this condition to be met.

Since the estimator is thus already unbiased due to its architecture, Kalman suggested to further increase performance by minimizing error variances, resulting in the cost function $J(\mathbf{k})$ according to

$$J(\mathbf{k}) = \mathbb{E}[(x_1 - \hat{x}_1)^2] + \dots + \mathbb{E}[(x_{n_x} - \hat{x}_{n_x})^2] = \text{Tr}[\hat{\mathbf{P}}_{\text{corr}}(\mathbf{k})] \quad (\text{B.21})$$

with x_1, \dots, x_{n_x} as the elements of $\mathbf{x}(\mathbf{k})$ and $\hat{\mathbf{P}}_{\text{corr}}$ as the covariance matrix of the estimation error related to correction. Based on Eq. (B.18), $\hat{\mathbf{P}}_{\text{corr}}$ is calculated by

$$\begin{aligned} \hat{\mathbf{P}}_{\text{corr}}(\mathbf{k}) &= \text{Cov}[\hat{\boldsymbol{\epsilon}}_{\text{corr}}(\mathbf{k}), \hat{\boldsymbol{\epsilon}}_{\text{corr}}(\mathbf{k})] = \text{Var}[\hat{\boldsymbol{\epsilon}}_{\text{corr}}(\mathbf{k})] \\ &= \text{Var}[(\mathbf{I} - \mathbf{K}(\mathbf{k}) \mathbf{C}_d) \hat{\boldsymbol{\epsilon}}_{\text{pred}}(\mathbf{k}) - \mathbf{K}(\mathbf{k}) \mathbf{v}(\mathbf{k})] \\ &= \text{Var}[(\mathbf{I} - \mathbf{K}(\mathbf{k}) \mathbf{C}_d) \hat{\boldsymbol{\epsilon}}_{\text{pred}}(\mathbf{k})] + \text{Var}[-\mathbf{K}(\mathbf{k}) \mathbf{v}(\mathbf{k})] + \dots \\ &\quad \underbrace{2 \text{Cov}[(\mathbf{I} - \mathbf{K}(\mathbf{k}) \mathbf{C}_d) \hat{\boldsymbol{\epsilon}}_{\text{pred}}(\mathbf{k}), -\mathbf{K}(\mathbf{k}) \mathbf{v}(\mathbf{k})]}_{=0 \text{ (non-causal dependency)}} \\ &= (\mathbf{I} - \mathbf{K}(\mathbf{k}) \mathbf{C}_d) \text{Var}[\hat{\boldsymbol{\epsilon}}_{\text{pred}}(\mathbf{k})] (\mathbf{I} - \mathbf{K}(\mathbf{k}) \mathbf{C}_d)^T + \mathbf{K}(\mathbf{k}) \text{Var}[\mathbf{v}(\mathbf{k})] \mathbf{K}(\mathbf{k})^T \\ &= (\mathbf{I} - \mathbf{K}(\mathbf{k}) \mathbf{C}_d) \hat{\mathbf{P}}_{\text{pred}}(\mathbf{k}) (\mathbf{I} - \mathbf{K}(\mathbf{k}) \mathbf{C}_d)^T + \mathbf{K}(\mathbf{k}) \mathbf{R}(\mathbf{k}) \mathbf{K}(\mathbf{k})^T \quad (\text{B.22}) \end{aligned}$$

with the covariance matrix $\hat{\mathbf{P}}_{\text{pred}}$ of the estimation error related to prediction given by

$$\begin{aligned} \hat{\mathbf{P}}_{\text{pred}}(\mathbf{k}) &= \text{Cov}[\hat{\boldsymbol{\epsilon}}_{\text{pred}}(\mathbf{k}), \hat{\boldsymbol{\epsilon}}_{\text{pred}}(\mathbf{k})] = \text{Var}[\hat{\boldsymbol{\epsilon}}_{\text{pred}}(\mathbf{k})] \\ &= \text{Var}[\mathbf{A}_d \hat{\boldsymbol{\epsilon}}_{\text{corr}}(\mathbf{k}-1) + \mathbf{G}_d \mathbf{w}(\mathbf{k}-1)] \\ &= \text{Var}[\mathbf{A}_d \hat{\boldsymbol{\epsilon}}_{\text{corr}}(\mathbf{k}-1)] + \text{Var}[\mathbf{G}_d \mathbf{w}(\mathbf{k}-1)] + \underbrace{2 \text{Cov}[\mathbf{A}_d \hat{\boldsymbol{\epsilon}}_{\text{corr}}(\mathbf{k}-1), \mathbf{G}_d \mathbf{w}(\mathbf{k}-1)]}_{=0 \text{ (non-causal dependency)}} \\ &= \mathbf{A}_d \text{Var}[\hat{\boldsymbol{\epsilon}}_{\text{corr}}(\mathbf{k}-1)] \mathbf{A}_d^T + \mathbf{G}_d \text{Var}[\mathbf{w}(\mathbf{k}-1)] \mathbf{G}_d^T \\ &= \mathbf{A}_d \hat{\mathbf{P}}_{\text{corr}}(\mathbf{k}-1) \mathbf{A}_d^T + \mathbf{G}_d \mathbf{Q}(\mathbf{k}-1) \mathbf{G}_d^T. \quad (\text{B.23}) \end{aligned}$$

Therefore, the still undetermined matrix $\mathbf{K}(k)$ is used to minimize the cost function (Eq. B.21), which yields

$$\frac{\partial \text{Tr} [\hat{\mathbf{P}}_{\text{corr}}(k)]}{\partial \mathbf{K}(k)} \stackrel{!}{=} \mathbf{0} \rightarrow \mathbf{K}(k) = \hat{\mathbf{P}}_{\text{pred}}(k) \mathbf{C}_d^T [\mathbf{C}_d \hat{\mathbf{P}}_{\text{pred}}(k) \mathbf{C}_d^T + \mathbf{R}(k)]^{-1}. \quad (\text{B.24})$$

Since $\mathbf{R}(k)$ and $\hat{\mathbf{P}}_{\text{corr}}(0)$ are chosen as positive definite matrices, $\hat{\mathbf{P}}_{\text{pred}}$ is also positive definite for all time. Thus, the second partial derivative

$$\frac{\partial^2 \text{Tr} [\hat{\mathbf{P}}_{\text{corr}}(k)]}{\partial^2 \mathbf{K}(k)} = 2 [\mathbf{C}_d \hat{\mathbf{P}}_{\text{pred}}(k) \mathbf{C}_d^T + \mathbf{R}(k)]^T \quad (\text{B.25})$$

is positive definite as well. Therefore, the so defined Kalman gain \mathbf{K} is always accompanied by a minimum of the cost function. Using relation (B.24) simplifies the calculation of $\hat{\mathbf{P}}_{\text{corr}}$, Eq. (B.26).

$$\hat{\mathbf{P}}_{\text{corr}}(k) = [\mathbf{I} - \mathbf{K}(k) \mathbf{C}_d] \hat{\mathbf{P}}_{\text{pred}}(k). \quad (\text{B.26})$$

B.4 One-step Kalman filter equations

For ease of legibility, recursive filter equations for a single calculation step are summarized in the boxes given below.

prediction

$$\hat{\mathbf{x}}_{\text{pred}}(k) = \mathbf{A}_d \hat{\mathbf{x}}_{\text{corr}}(k-1) + \mathbf{B}_d \mathbf{u}(k-1) \quad (\text{B.27})$$

$$\hat{\mathbf{y}}_{\text{pred}}(k) = \mathbf{C}_d \hat{\mathbf{x}}_{\text{pred}}(k) + \mathbf{D}_d \mathbf{u}(k) \quad (\text{B.28})$$

$$\hat{\mathbf{P}}_{\text{pred}}(k) = \mathbf{A}_d \hat{\mathbf{P}}_{\text{corr}}(k-1) \mathbf{A}_d^T + \mathbf{G}_d \mathbf{Q}(k-1) \mathbf{G}_d^T \quad (\text{B.29})$$

correction

$$\mathbf{K}(k) = \hat{\mathbf{P}}_{\text{pred}}(k) \mathbf{C}_d^T [\mathbf{C}_d \hat{\mathbf{P}}_{\text{pred}}(k) \mathbf{C}_d^T + \mathbf{R}(k)]^{-1} \quad (\text{B.30})$$

$$\Delta \mathbf{y}(k) = \mathbf{y}(k) - \hat{\mathbf{y}}_{\text{pred}}(k) \quad (\text{B.31})$$

$$\hat{\mathbf{x}}_{\text{corr}}(k) = \hat{\mathbf{x}}_{\text{pred}}(k) + \mathbf{K}(k) \Delta \mathbf{y}(k) \quad (\text{B.32})$$

$$\hat{\mathbf{P}}_{\text{corr}}(k) = [\mathbf{I} - \mathbf{K}(k) \mathbf{C}_d] \hat{\mathbf{P}}_{\text{pred}}(k) \quad (\text{B.33})$$

Figure B.2 illustrates the estimation procedure to gain a state estimate at time step k . While the graphical representation covers a model with only one state, presented relations are still valid in a more general case with numerous states. Starting with the corrected state estimate $\hat{\mathbf{x}}_{\text{corr}}$ at the previous time step $k-1$, Eqs. (B.27) and (B.28)

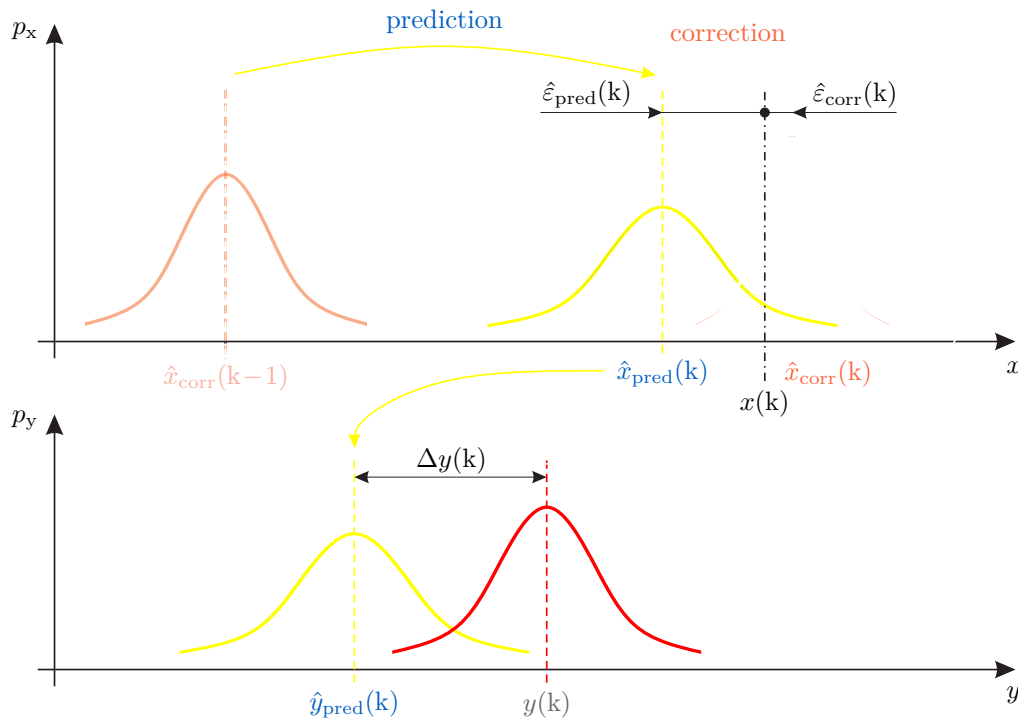


Figure B.2: Simplified graphical representation, adapted from [42], of the Kalman filter algorithm to estimate the state vector at time step k .

provide the predicted state estimate $\hat{\mathbf{x}}_{\text{pred}}$ and output estimate $\hat{\mathbf{y}}_{\text{pred}}$ at the actual time step k , respectively. Incorporating measured output values $\mathbf{y}(k)$ by Eq. (B.29) and calculating Kalman gain using Eqs. (B.29) and (B.30) yield the corrected state estimate $\hat{\mathbf{x}}_{\text{corr}}$ at the actual time step. As a basis for the next iteration, the covariance matrix of the estimation error related to correction is calculated by Eq. (B.33).

B.5 Existence and stability

Full state observability of the pair $(\mathbf{A}_d, \mathbf{C}_d)$ is sufficient for the existence of a Kalman filter [43–45], since otherwise not all states uniquely affect measured values \mathbf{y} .

However, it is more challenging to prove asymptotic stability of the Kalman filter (see Eq. B.20). It was shown that full state controllability of the pair $(\mathbf{A}_d, \mathbf{G}_d)$ and \mathbf{Q} being positive definite ensure asymptotic stability [43–45]. If the noise process is written compactly according to Eq. (B.10), one can simplify this condition: the covariance matrix $\tilde{\mathbf{Q}}$ of the compactly written process noise has to be positive definite. This is valid if process noises acting on different states are independent of each other and exhibit non-zero variances. While the latter interpretation seems reasonable from a practical point of view, a more formal approach is to look into the following formulation of the covariance matrix of the estimation error related to prediction

$$\hat{\mathbf{P}}_{\text{pred}}(k) = \mathbf{A}_d \hat{\mathbf{P}}_{\text{pred}}(k-1) \mathbf{A}_d^T + \mathbf{A}_d \mathbf{K}(k-1) \mathbf{C}_d \hat{\mathbf{P}}_{\text{pred}}(k-1) \mathbf{A}_d^T + \tilde{\mathbf{Q}}(k-1). \quad (\text{B.34})$$

This so-called discrete Riccati equation exhibits a steady solution of $\mathbf{0}$ for $\hat{\mathbf{P}}_{\text{pred}}$ in case the last term diminishes. Since each scalar process noise with zero variance in the compactly written form is related to a zero value in the diagonal of $\tilde{\mathbf{Q}}$, affected elements of $\hat{\mathbf{P}}_{\text{pred}}$ will eventually approach 0. Subsequently, associated elements of \mathbf{K} will vanish as well. Therefore, corresponding corrected state estimates will remain unaffected, independent of how large occurring deviations $\Delta\mathbf{y}$ will become. To sum up, too small variances of process noise come along with biased estimation results, while too large values result in a non-optimal estimation algorithm. As long as the chosen values cover real circumstances perfectly, the Kalman filter provides satisfying estimates. But since almost every implementation hypothesizes constant noise covariances, sudden disturbances, which can be interpreted as sharp changes in the noise variance, lack of appropriate consideration. To overcome this issue, process noise variances can be chosen higher than expected during normal operation. Although, the filter is thus not optimal anymore, increased robustness justifies this approach by far.

Lastly, it is worth mentioning that the Kalman filter is the optimal filter for a linear system with Gaussian distributed noises and in spite of many publications it is still the optimal *linear* filter even if noise processes are not Gaussian distributed.

B.6 Extended Kalman filter

Based on the classic approach, the Kalman filter algorithm can be simply extended to serve the need for state estimation of non-linear systems. Using the discrete-time model, given by

$$\mathbf{x}(k) = \mathbf{f}(\mathbf{x}(k-1), \mathbf{u}(k-1), \mathbf{w}(k-1)) \quad (\text{B.35})$$

$$\mathbf{y}(k) = \mathbf{g}(\mathbf{x}(k), \mathbf{u}(k), \mathbf{v}(k)), \quad (\text{B.36})$$

local linearization of the state and output equation provides the following matrices:

$$\begin{aligned} \mathbf{A}_d(k-1) &= \left. \frac{\partial \mathbf{f}}{\partial \mathbf{x}} \right|_{\hat{\mathbf{x}}_{\text{corr}}(k-1)} & \mathbf{C}_d(k) &= \left. \frac{\partial \mathbf{g}}{\partial \mathbf{x}} \right|_{\hat{\mathbf{x}}_{\text{pred}}(k)} \\ \mathbf{G}_d(k-1) &= \left. \frac{\partial \mathbf{f}}{\partial \mathbf{w}} \right|_{\hat{\mathbf{x}}_{\text{corr}}(k-1)} & \mathbf{F}_d(k) &= \left. \frac{\partial \mathbf{g}}{\partial \mathbf{v}} \right|_{\hat{\mathbf{x}}_{\text{pred}}(k)} \end{aligned}$$

Adapting the filter equations depicted in section B.4 by utilizing these linearizations yield the equations of the extended Kalman filter algorithm - see boxes below.

prediction

$$\hat{\mathbf{x}}_{\text{pred}}(k) = \mathbf{f}(\hat{\mathbf{x}}_{\text{corr}}(k-1), \mathbf{u}(k-1), \mathbf{0})$$

$$\hat{\mathbf{y}}_{\text{pred}}(k) = \mathbf{g}(\hat{\mathbf{x}}_{\text{pred}}(k), \mathbf{u}(k), \mathbf{0})$$

$$\hat{\mathbf{P}}_{\text{pred}}(k) = \mathbf{A}_d(k-1) \hat{\mathbf{P}}_{\text{corr}}(k-1) \mathbf{A}_d(k-1)^T + \mathbf{G}_d(k-1) \mathbf{Q}(k-1) \mathbf{G}_d(k-1)^T$$

correction

$$\mathbf{K}(k) = \hat{\mathbf{P}}_{\text{pred}}(k) \mathbf{C}_d(k)^T \left[\mathbf{C}_d(k) \hat{\mathbf{P}}_{\text{pred}}(k) \mathbf{C}_d(k)^T + \mathbf{F}_d(k) \mathbf{R}(k) \mathbf{F}_d(k)^T \right]^{-1}$$

$$\Delta \mathbf{y}(k) = \mathbf{y}(k) - \hat{\mathbf{y}}_{\text{pred}}(k)$$

$$\hat{\mathbf{x}}_{\text{corr}}(k) = \hat{\mathbf{x}}_{\text{pred}}(k) + \mathbf{K}(k) \Delta \mathbf{y}(k)$$

$$\hat{\mathbf{P}}_{\text{corr}}(k) = [\mathbf{I} - \mathbf{K}(k) \mathbf{C}_d(k)] \hat{\mathbf{P}}_{\text{pred}}(k)$$

Appendix C

Fundamentals of gap metric

Gap metrics were originally introduced by Zames and El-Sakkary [46] to study uncertainty in feedback systems. Since then, gap metrics have been extensively applied in the broad field of robust control. In this diploma thesis, the ν -gap metric, introduced by Vinnicombe [33], was utilized to find an appropriate linearization point of a non-linear plant model. Its supplementary role within this work justifies to neglect mentioning comprehensive and complex fundamentals of robust control. While the following remarks only relate to practical application, mathematical aspects are excessively presented and discussed in [33, 46, 47].

The ν -gap metric provides a value $\delta_\nu(P_1, P_2)$ with $0 \leq \delta_\nu \leq 1$ to assess the gap between two linear transfer functions P_1 and P_2 in a closed-loop sense. Values close to 0 indicate that one controller is likely to sufficiently control both plants (P_1 and P_2), while values close to 1 illustrate substantial differences in the closed-loop behaviors by using one and the same controller.

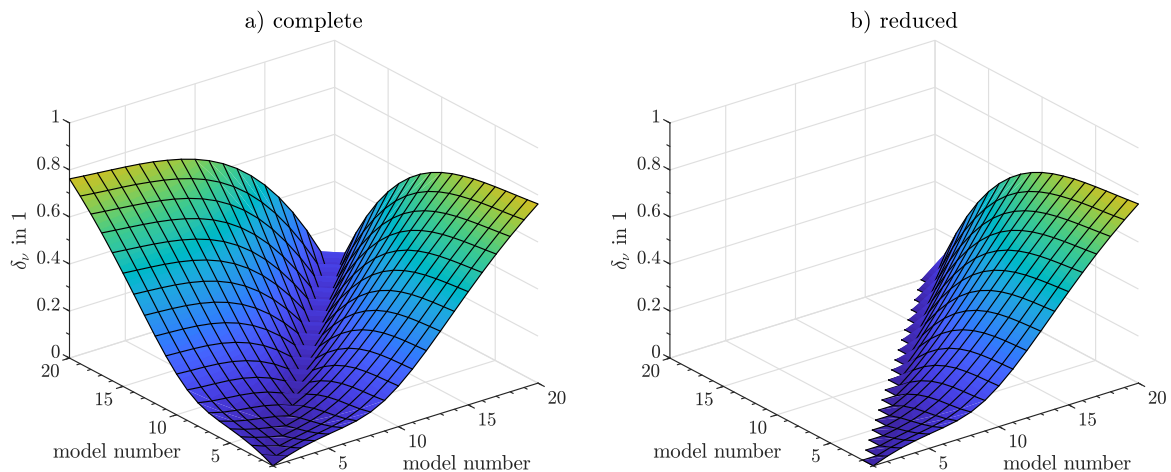


Figure C.1: Exemplary gap map covering pairwise comparisons of 20 linear models, depicted (a) completely and (b) reduced to the essential. Single results are connected smoothly to guide the eye.

This scheme can be utilized to compare linear transfer functions resulting from the approximation of a non-linear model in the vicinity of different linearization points. Pairwise comparisons of many different linear models, which are characterized by linearization points distributed within the whole operating range, are usually depicted graphically, see an exemplary gap map in Fig. C.1a. Since $\delta_\nu(P_1, P_2) = \delta_\nu(P_2, P_1)$ holds by definition of a metric, only half of the diagram covers the whole information (Fig. C.1b). Clearly, gap values of models compared with themselves vanish.

Graphically presented results are subsequently used to find a model that exhibits the least maximum gap value to all other linear models. As a sufficiently small gap thereby ensures satisfying control performance in the whole operating range by a single linear controller, controller design itself has to consider only the so found linear model. Besides determination of linearization points, this procedure is also helpful for defining appropriate submodels in multilinear model approaches [48].

Bibliography

- [1] J.A.J. Gowlett and R.W. Wrangham. Earliest fire in africa: towards the convergence of archaeological evidence and the cooking hypothesis. *Azania: Archaeological Research in Africa*, 48:5–30, 2013.
- [2] M. Kaltschmitt, H. Hartmann, and H. Hofbauer. *Energie aus Biomasse: Grundlagen, Techniken und Verfahren*. Springer-Verlag, 2009.
- [3] B. Nagel, H. Dellweg, and L.M. Gierasch. Glossary for chemists of terms used in biotechnology (IUPAC Recommendations 1992). *Pure and Applied Chemistry*, 64:143–168, 1992.
- [4] European Commission - Eurostat. Share of energy from renewable sources for heating and cooling. [https://ec.europa.eu/eurostat/statistics-explained/index.php?title=File:Share_of_energy_from_renewable_sources_for_heating_and_cooling,_2004-2018_\(%25\).png](https://ec.europa.eu/eurostat/statistics-explained/index.php?title=File:Share_of_energy_from_renewable_sources_for_heating_and_cooling,_2004-2018_(%25).png), accessed online, 29.4.2020.
- [5] Umweltbundesamt Deutschland. Erneuerbare Energien in Zahlen. <https://www.umweltbundesamt.de/themen/klima-energie/erneuerbare-energien/erneuerbare-energien-in-zahlen?sprungmarke=waerme#uberblick>, accessed online, 29.4.2020.
- [6] Landesrecht Wien. Art. 15a B-VG über das Inverkehrbringen von Kleinf Feuerungen und die Überprüfung von Feuerungsanlagen und Blockheizkraftwerken in der geltenden Fassung vom 25. April 2020.
- [7] Bundesamt für Justiz Deutschland. Verordnung über kleine und mittlere Feuerungsanlagen vom 26. Januar 2010 (BGBl. I S. 38).
- [8] J. Kortela and S.L. Jämsä-Jounela. Modeling and model predictive control of the BioPower combined heat and power (CHP) plant. *International Journal of Electrical Power & Energy Systems*, 65:453–462, 2015.
- [9] J. Kortela and S.L. Jämsä-Jounela. Model predictive control utilizing fuel and moisture soft-sensors for the Biopower 5 combined heat and power (CHP) plant. *Applied energy*, 131:189–200, 2014.

- [10] N. Paces, A. Voigt, S. Jakubek, A. Schirrer, and M. Kozek. Combined control of combustion load and combustion position in a moving grate biomass furnace. In *19th Mediterranean Conference on Control & Automation (MED)*, pages 1447–1452. IEEE, 2011.
- [11] M. Leskens, L.B.M. van Kessel, and O.H. Bosgra. Model predictive control as a tool for improving the process operation of MSW combustion plants. *Waste Management*, 25(8):788–798, 2005.
- [12] M. Gölles, R. Bauer, T. Brunner, N. Dourdoumas, and I. Obernberger. Model based control of a biomass grate furnace. In *European Conference on Industrial Furnaces and Boilers*, volume 9, pages 1–10, 2011.
- [13] C. Schörghuber, M. Gölles, N. Dourdoumas, and I. Obernberger. Modellbasierte Regelung des Sekundärluftmassenstromes bei Biomasse-Feuerungsanlagen. *at-Automatisierungstechnik*, 62(7):487–499, 2014.
- [14] L. Böhler, J. Krail, G. Görtler, and M. Kozek. Fuzzy model predictive control for small-scale biomass combustion furnaces. *Applied Energy*, submitted, 2020.
- [15] L. Böhler, G. Görtler, J. Krail, and M. Kozek. Carbon monoxide emission models for small-scale biomass combustion of wooden pellets. *Applied Energy*, 254:113668, 2019.
- [16] DIN EN ISO 18125:2017-08: Solid biofuels - Determination of calorific value.
- [17] V. Placek and B. Sulc. Support of biomass boiler control design by modeling. In *Proceedings of the 2015 16th International Carpathian Control Conference (ICCC)*, pages 393–398. IEEE, 2015.
- [18] R. Bauer, M. Gölles, T. Brunner, N. Dourdoumas, and I. Obernberger. Modelling of grate combustion in a medium scale biomass furnace for control purposes. *Biomass and Bioenergy*, 34(4):417–427, 2010.
- [19] R. Seeber, M. Gölles, N. Dourdoumas, and M. Horn. Reference shaping for model-based control of biomass grate boilers. *Control engineering practice*, 82:173–184, 2019.
- [20] R. Seeber, M. Goelles, T. Brunner, N. Dourdoumas, and I. Obernberger. Improvement of a model based control strategy for biomass furnaces. *at-Automatisierungstechnik*, 62(12):891–902, 2014.
- [21] R.P. Van Der Lans, L.T. Pedersen, A. Jensen, P. Glarborg, and K. Dam-Johansen. Modelling and experiments of straw combustion in a grate furnace. *Biomass and Bioenergy*, 19(3):199–208, 2000.

- [22] A. Boriouchkine and S.L. Jämsä-Jounela. Simplification of a mechanistic model of biomass combustion for on-line computations. *Energies*, 9:735, 2016.
- [23] R. Strzalka, T.G. Erhart, and U. Eicker. Analysis and optimization of a co-generation system based on biomass combustion. *Applied Thermal Engineering*, 50(2):1418–1426, 2013.
- [24] R. Bauer, M. Goelles, T. Brunner, N. Dourdoumas, and I. Obernberger. Dynamic modelling of the heat transfer in a gas tube heat exchanger. *at-Automatisierungstechnik*, 56(10):513–520, 2008.
- [25] DIN EN ISO 18134-2:2017-05: Solid biofuels - Determination of moisture content - Oven dry method - Part 2: Total moisture - Simplified method.
- [26] DIN EN ISO 18122:2016-03: Solid biofuels - Determination of ash content.
- [27] L. Ljung. *System Identification: Theory for the User*. Prentice Hall information and system sciences series. Prentice Hall PTR, 1999.
- [28] M. Kozek and S. Jakubek. Identifikation und Experimentelle Modellbildung. *lecture notes*, Technische Universität Wien, 2018.
- [29] Q.G. Wang. *Decoupling control*, volume 285. Springer Science & Business Media, 2002.
- [30] B. Charlet, J. Lévine, and R. Marino. On dynamic feedback linearization. *Systems & Control Letters*, 13(2):143–151, 1989.
- [31] J. Deutscher. *Zustandsregelung verteilt-parametrischer Systeme*. Springer-Verlag, 2012.
- [32] L. Wang. *Model predictive control system design and implementation using MATLAB®*. Springer Science & Business Media, 2009.
- [33] G. Vinnicombe. *Uncertainty and Feedback: H_∞ Loop-shaping and the ν -gap Metric*. World Scientific, 2001.
- [34] S. Haykin. *Kalman filtering and neural networks*, volume 47. John Wiley & Sons, 2004.
- [35] J. Kortela and S.L. Jämsä-Jounela. Fuel moisture soft-sensor and its validation for the industrial BioPower 5 CHP plant. *Applied energy*, 105:66–74, 2013.
- [36] S. Jakubek and A. Schirrer. Adaptive and Predictive Control. *lecture notes*, Technische Universität Wien, 2019.
- [37] J.B. Rawlings and D.Q. Mayne. *Model predictive control: Theory and design*. Nob Hill Pub., 2009.

- [38] R. E. Kalman. A new approach to linear filtering and prediction problems. 1960.
- [39] C.F. Gauss. *Theoria motus corporum coelestium in sectionibus conicis solem ambientium*, volume 7. Perthes et Besser, 1809.
- [40] D. Simon. *Optimal state estimation: Kalman, H infinity, and nonlinear approaches*. John Wiley & Sons, 2006.
- [41] R. Marchthaler and S. Dingler. *Kalman-Filter*. Springer, 2017.
- [42] MathWorks®. Understanding Kalman Filters. <https://www.mathworks.com/videos/series/understanding-kalman-filters.html>, accessed online, 15.5.2020.
- [43] J. Deyst and C. Price. Conditions for asymptotic stability of the discrete minimum-variance linear estimator. *IEEE Transactions on Automatic Control*, 13(6):702–705, 1968.
- [44] B.D.O. Anderson and J.B. Moore. Detectability and stabilizability of time-varying discrete-time linear systems. *SIAM Journal on Control and Optimization*, 19(1):20–32, 1981.
- [45] B. Southall, B.F. Buxton, and J.A. Marchant. Controllability and Observability: Tools for Kalman Filter Design. In *BMVC*, pages 1–10, 1998.
- [46] G. Zames and A.K. El-sakkary. Unstable systems and feedback: The gap metric. 1980.
- [47] Z. Kemin and J.C. Doyle. *Essential of Robust Control*. Prentice Hall Inc, New Jersey, 1995.
- [48] J. Du, C. Song, and P. Li. Application of gap metric to model bank determination in multilinear model approach. *Journal of Process Control*, 19(2):231–240, 2009.